Microstructural Development and the Evolution of Defects in Constrained and Sinter-Forged Ceramics

Dustin Michael Frame

A dissertation submitted in partial fulfillment of the requirements for the degree of

Doctor of Philosophy

University of Washington

2006

Program Authorized to Offer Degree: Materials Science and Engineering

INFORMATION TO USERS

The quality of this reproduction is dependent upon the quality of the copy submitted. Broken or indistinct print, colored or poor quality illustrations and photographs, print bleed-through, substandard margins, and improper alignment can adversely affect reproduction.

In the unlikely event that the author did not send a complete manuscript and there are missing pages, these will be noted. Also, if unauthorized copyright material had to be removed, a note will indicate the deletion.

ProQuest Information and Learning Company
300 North Zeeb Road
P.O. Box 1346
Ann Arbor, MI 48106-1346

University of Washington
Graduate School

This is to certify that I have examined this copy of a doctoral dissertation by

Dustin Michael Frame

and have found that it is complete and satisfactory in all respects,
and that any and all revisions required by the final
examining committee have been made.

Chair of the Supervisory Committee:

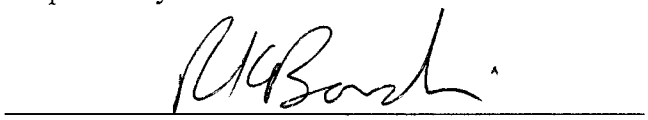

Rajendra K. Bordia

Reading Committee:

Rajendra K. Bordia

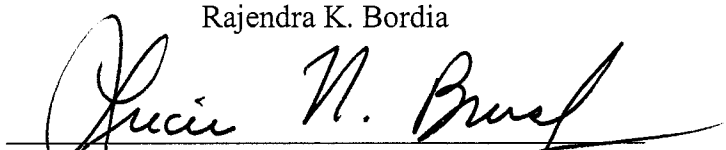

Lucien N. Brush

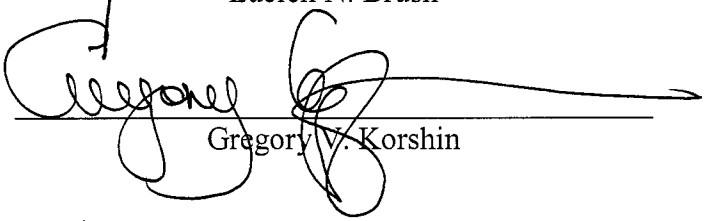

Gregory V. Korshin

Date: 8/14/06

In presenting this dissertation in partial fulfillment of the requirements for the doctoral degree at the University of Washington, I agree that the Library shall make its copies freely available for inspection. I further agree that extensive copying of the dissertation is allowable only for scholarly purposes, consistent with "fair use" as prescribed in the U.S. Copyright Law. Requests for copying or reproduction of this dissertation may be referred to Proquest Information and Learning, 300 North Zeeb Road, Ann Arbor, MI 48106-1346, 1-800-521-0600, to whom the author has granted "the right to reproduce and sell (a) copies of the manuscript in microform and/or (b) printed copies of the manuscript made from microform."

Signature Dustin Frane

Date 8/14/06

University of Washington

Abstract

Microstructural Development and the Evolution of Defects in Constrained and Sinter-Forged Ceramics

Dustin Michael Frame

Chair of the Supervisory Committee:
Professor Rajendra K. Bordia
Department of Materials Science and Engineering

In this study, the microstructural evolution of uniaxial loaded, or constrained sintered YSZ compacts and the growth of cracks and defects in constrained ceramic films is reported. It is shown that a uniaxial load applied to a YSZ compact will lead to a modified densification. In addition to a modified densification, the pore structure is shown to exhibit an anisotropic modification from the applied load, the magnitude of anisotropy increasing with load, temperature, and localized density. Further investigation of this anisotropic micro-pore behavior with artificial controlled sized pores shows that there is a critical pore size at which the behavior changes from that of nano-pores to that of micro-pores.

The growth of cracks and holes in constrained YSZ films is investigated by introducing artificial defects with a Focused Ion Beam into green centrifuge-cast YSZ films. This technique for studying defect growth allows micron scale defects to be introduced into a fragile green film for sintering studies. Stress concentrations near defects will lead to increased damage and crack growth in the films. Channel cracks are observed in the films with introduced defects, and are absent in films without defects. Sintering cracks are observed in some samples with high interfacial friction and large thickness. From analyzing the percent of each crack growth, small crack to large crack behavior transition point is observed.

Currently, most densification models assume isotropic sintering behavior. It is shown in this study that assumption is inaccurate. This research has increased the knowledge base of anisotropic microstructure evolution, an area that is currently not very well understood but applicable to many important systems.

TABLE OF CONTENTS

LIST OF FIGURES

LIST OF TABLES

ACKNOWLEDGEMENTS

The author wishes to express sincere appreciation to the students, faculty and staff of the Department of Materials Science & Engineering for their help and support which made this experience so valuable. The author would also like to give a special thanks to Professor Raj Bordia for his guidance and support.

DEDICATION

To my family

CHAPTER I

INTRODUCTION

I.1 GENERAL REMARKS

In processing ceramic compacts it is sometimes necessary to apply an external stress during sintering to aid densification, or to sinter a ceramic film constrained by a rigid substrate. The constraint from the rigid substrate generates internal stresses in the sintering film. During the sintering of a ceramic compact under an external, internal, single or multi-axis stress, a modified densification can result. This stress-driven modified densification can lead to warping, cracking, anisotropic microstructural development, or the growth of other instabilities. These effects are important in several significant application areas including Solid Oxide Fuel Cells (SOFCs), electronic packaging and environmental protective coatings. There has been significant research on this important topic; however, two issues have not received much attention. They are the evolution of anisotropic microstructures and the growth of cracks and other flaws.

The research in this dissertation is focused on understanding the microstructural evolution of uniaxial loaded, or constrained sintered YSZ compacts and the growth of cracks and defects in constrained ceramic films. In the uniaxial loaded samples the pore structure will be studied to understand the behavior of the anisotropy that develops with respect to processing parameters. In the constrained sintered samples, the effect that the in-plane biaxial stress has on the development of defects in the film will be studied.

Increasing the understanding of the development of anisotropic microstructures is important in order to aid the development of anisotropic sintering models. Currently, most densification models assume isotropic sintering behavior. This dissertation will

increase the knowledge base of anisotropic microstructure evolution, and aid in the development of anisotropic densification models.

The development of defects in a constrained film is not very well understood, but applicable to many important systems. A goal of this dissertation is to increase the fundamental understanding of how these defects develop in a constrained film at the submicron level and aid the understanding of how the internal sintering stresses drive their development. Technologically, this understanding will help in developing robust and reliable processing strategies for multilayer devices like SOFCs.

CHAPTER II

LITERATURE REVIEW

II.1 SOLID OXIDE FUEL CELLS

In 1897 Nernst filed a patent for an electric lamp that utilized an ionically conductive solid electrolyte that would glow when a voltage was applied across it [1]. In this Nernst glower, the second-class conductor would only start to conduct (and glow) when it was heated above a certain point upon which conduction would be significant. This lamp was intended to compete with the carbon filament electric lamp successfully invented by Thomas Edison only 17 years earlier. Although the Nernst lamp was not successful in competing with other electric lamp technologies, a significant step towards the development of Solid Oxide Fuel Cells (SOFCs) had begun.

The first Solid Oxide Fuel Cell was developed by Haber who filed a patent in 1905 [2]. As shown in Figure 2.1, Haber placed glass tubes (g) through an air tight heated chamber, which was being filled with generator gas. Air would pass through the glass tubes, which were coated on both sides with platinum. Subsequently, a potential would be measurable across the glass tube.

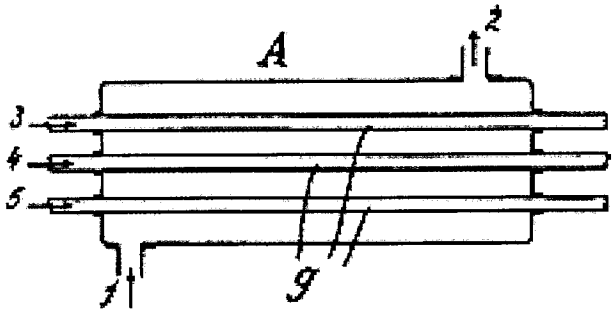

Figure 2.1 Haber's Solid Electrolyte Fuel Cell 1905 [2]

SOFCs would continue to use platinum as the electrodes until Baur further developed the SOFC by creating solid metal oxide electrodes [3]. The first time Yttria Stabilized Zirconia was used in a solid oxide fuel cell was in 1937 by Baur and Preis [4]. Their SOFC used a coke anode and iron oxide as the cathode. Much more work would be done to further characterize the mechanisms of SOFCs, but the foundation was set for the SOFC field we see today.

II.1.1 Components of a SOFC

As shown in Figure 2.2, the three main parts of a Solid Oxide Fuel Cell are the anode, cathode, and the electrolyte. The anode and cathode are both porous electrodes. They are required to be both electrically and ionically conductive. The electrolyte is an electric insulator, but an ionic conductor. The electrolyte serves to separate the two reactions electrically, but allow the chemical potential to drive the ions across the electrolyte and force the electrons to pass around the electrolyte to the other side.

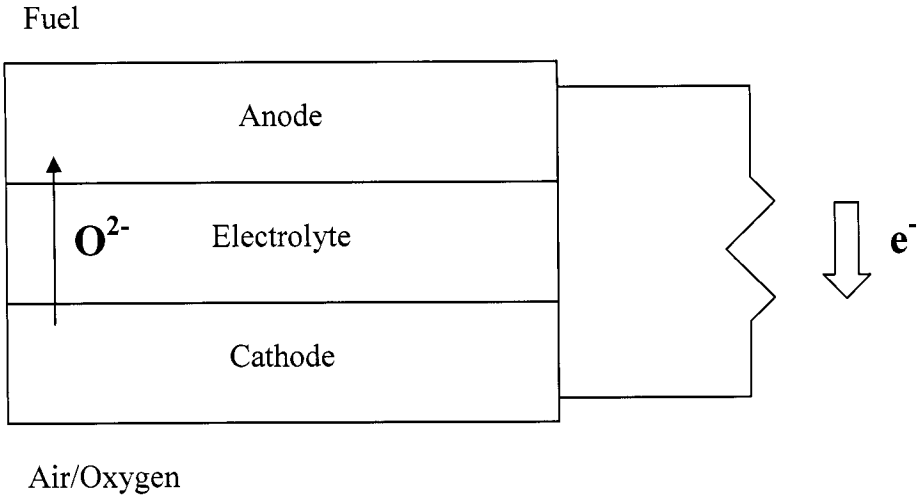

Figure 2.2 Components of a Solid Oxide Fuel Cell

Currently the most common cathode material is Strontium doped Lanthanum Manganite or LSM. LSM is stable in an oxidizing environment, has a good electrical conductivity, and exhibits good activity for oxygen reduction under the operating conditions. The most commonly used Anode material is a Nickel-Zirconia cermet. Ni/YSZ is electrically conductive, stable in a reducing environment, and the YSZ provides the ionic conduction [5].

II.1.2 Operation of a SOFC

In a Solid Oxide Fuel Cell, the fuel can be hydrogen (H_2), carbon monoxide (CO), carbon (C), or a hydrocarbon chain that can be reformed in the cell to create one or more of these. Many hydrocarbons can be used and internally reformed because of the high operating temperature, removing the need for expensive external fuel reformers. The oxidizer needs to be either air, which is 20% oxygen, or pure oxygen. The reaction at the cathode side is:

$$O_2 + 4e^- \rightarrow 2O^{2-} \quad (2.1)$$

The possible reactions for the anode side are:

$$CO + O^{2-} \rightarrow CO_2 + 2e^- \quad (2.2)$$

$$H_2 + O^{2-} \rightarrow H_2O + 2e^- \quad (2.3)$$

$$C + 2O^{2-} \rightarrow CO_2 + 4e^- \quad (2.4)$$

The overall possible reactions for the cell are:

$$H_2 + \tfrac{1}{2} O_2 \rightarrow H_2O \quad (2.5)$$

$$CO + \tfrac{1}{2} O_2 \rightarrow CO_2 \quad (2.6)$$

$$C + O_2 \rightarrow CO_2 \quad (2.7)$$

Besides water and CO_2, SOFCs create high quality waste heat as a by-product. This waste heat can be used for cogeneration, heating buildings, or other heating purposes. Through cogeneration or other uses of waste heat, the overall efficiency of a SOFC system can be greatly increased.

II.2 YTTRIA STABILIZED ZIRCONIA

In Nernts's efforts to find the best material for his new lamp, he experimented with many materials to find which one had the best ionic conductivity (the mechanism of which would be described in 1943 by Wagner [6]). In 1899 the best material that he came up with was 85% Zirconia and 15% Yttria [7]. The first time this material was used in a fuel cell was by Baur in 1937 [4].

A hundred years after Nernst used 85% Zirconia and 15% Yttria, Yttria Stabilized Zirconia (at about the same % of Yttria) is the most commonly used SOFC electrolyte for it's high conductivity, low cost, good strength, and high chemical stability.

II.2.1 Yttria Stabilized Zirconia Structure

The crystal structure of Zirconia is a Cubic Fluorite, shown in Figure 2.3. Zirconium atoms have a 4+ charge, and Yttrium has a 3+ charge. These charges imply that when oxidized, Yttrium will require less oxygen to satisfy the charge requirements. So when Yttria is doped into Zirconia in the Cubic Fluorite lattice, less oxygen is needed. The reduction in the number of oxygen atoms, while maintaining the cubic fluorite structure, creates oxygen site vacancies. Hund first discovered this phenomenon of ion vacancies in 1951 [8]. The availability of many oxygen ion vacancies, in addition to the structure of the fluorite lattice, leads to high oxygen ion conductivity in this material.

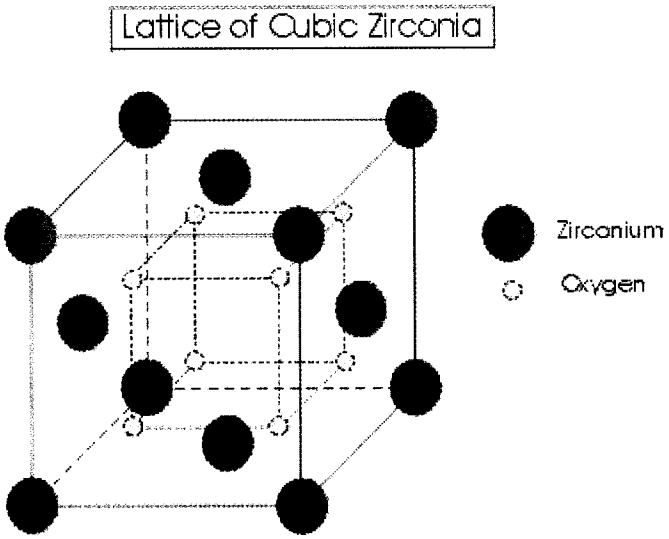

Figure 2.3 Cubic Fluorite Crystal structure of Cubic Zirconia [9]

In Figure 2.4 a ZrO_2 – Y_2O_3 phase diagram is shown. With the doping of Yttrium into the Zirconia, the high temperature cubic and tetragonal phases are stabilized, allowing them to exist at room temperature as metastable phases. This leads to a high ionic conductivity at a range of temperatures [10]. In pure ZrO_2, these phases are stable at relatively high temperatures (approximately 1000°C for the tetragonal and 2400°C for the cubic phase).

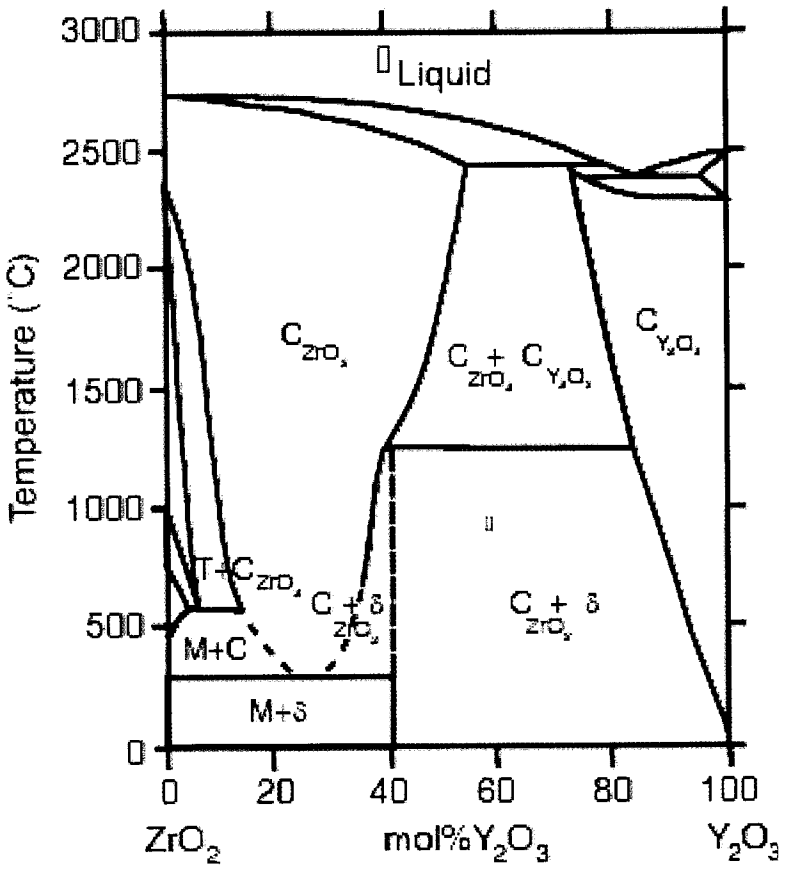

Figure 2.4 Zirconia – Yttria phase diagram [11]

II.3 SINTERING

Sintering is the process of forming a coherent object from smaller pieces by heating to a high temperature below the melting temperature. In polycrystalline materials, there are two main types of sintering, liquid phase sintering and solid state sintering. Liquid phase sintering is when a small-percentage of a second material exists as a glass at the sintering temperature of the main constituent. The presence of the glass aids the sintering of the main constituent. This dissertation deals solely with solid state sintering of polycrystalline materials. Solid state sintering is where all constituents are solid during the sintering step, and densification occurs by solid state diffusion.

II.3.1 Sintering Driving Force

The driving force for sintering is the reduction in surface energy. The free energy associated with solid-vapor interfaces is larger than that of the solid-solid interfaces. In solid state sintering, the higher energy solid-vapor interfaces are replaced by the lower energy solid-solid interfaces. This results in an overall reduction in the total free energy.

When two particles come in contact (whether they are single crystal, amorphous, or polycrystalline), there is an interfacial energy acting over this curved surface (or neck). The sintering stress (Σ) associated with this interfacial energy is correlated to the interparticle neck. The sintering stress given by Equation (2.8) is used as the basis for geometric sintering models [12]. G is the grain size, r is the radius of curvature of the pore, γ is the surface energy, and γ_b is the grain boundary energy.

$$\sigma = \frac{2\gamma_b}{G} + \frac{2\gamma}{r} \tag{2.8}$$

Since a ceramic compact made of fine particles has a large solid-vapor interfacial area relative to its mass there is a large driving force for sintering. In order to accomplish sintering of the compact (in non-geological time frames) the sample must be heated to an elevated temperature in order to increase the mobility of atoms in the material. The higher the surface area to mass ratio is in a compact, the lower the temperature the compact needs to be taken to in order to exhibit the same sintering rate. The higher the temperature the faster the sintering rate.

II.3.2 Stages of Sintering

Sintering involves significant geometric changes, and in order to facilitate the understanding of the changes, it has been conceptually divided into three stages. Many authors have provided described of these stages. One example is by Coble [13, 14]. The evaluation of the microstructure is schematically illustrated in Figure 2.5.

In the initial stage of sintering, the main evolution is neck growth between individual particles. The neck is the point of contact between two particles. This stage involves little to no grain growth and there is little densification of the compact in this stage. The intermediate stage of densification involves the largest amount of densification. Grain growth begins in this stage but is limited. Pores become well defined during this stage and are interconnected. The final stage of sintering involves some densification, but the grain growth is the main microstructural change in this stage. The interconnected pores that developed during the intermediate stage are now isolated, and are present at the grain junctions or within the grains.

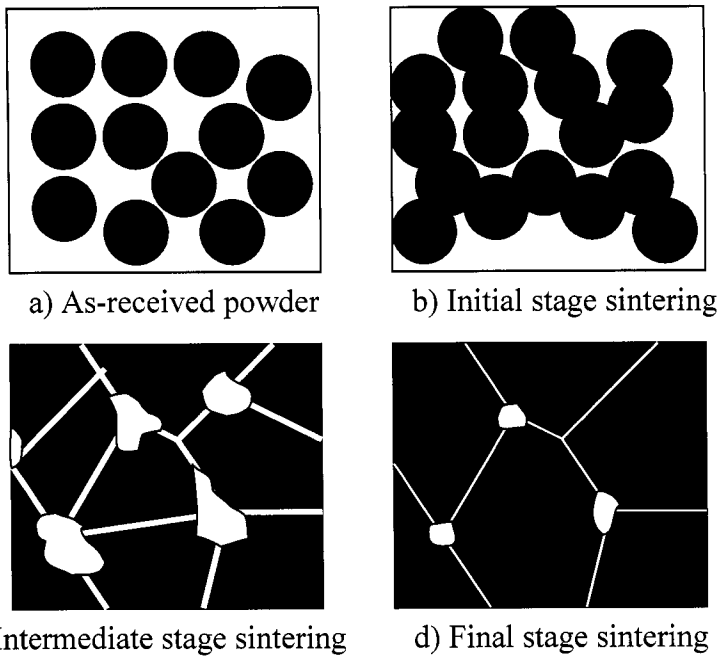

Figure 2.5 Microstructural evolution during the three stages of sintering a) As-received b) Initial stage neck growth c) Intermediate stage d) Final stage

II.3.3 Sintering Mechanisms

In order for the reduction of interfaces, there must be transport of the atoms in the compact. Ashby described six distinguishable mechanisms that contribute to the sintering of a particle aggregate in solid state sintering [15]. The six mechanisms are illustrated in Figure 2.6 and described in Table 2.1.

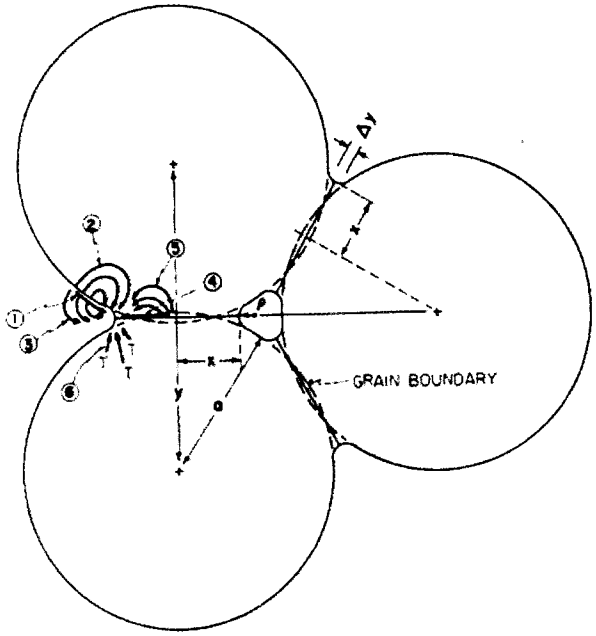

Figure 2.6 Six paths in diffusion controlled sintering [15]

Table 2.1 Six mechanisms that are possible in diffusion controlled sintering.

Mechanism No.	Transport path	Source of matter	Sink of matter
1	Surface diffusion	Surface	Neck
2	Lattice diffusion	Surface	Neck
3	Vapor Transport	Surface	Neck
4	Boundary diffusion	Grain boundary	Neck
5	Lattice diffusion	Grain boundary	Neck
6	Lattice diffusion	Dislocations	Neck

The first three mechanisms move atoms from the surface to the growing neck. These mechanisms do not contribute to densification (reduction in volume of the compact). These mechanisms are called coarsening mechanisms. The last three mechanisms move atoms from the interior of the particles to the neck, which results in reduction of the compact volume. These are called densifying mechanisms.

II.4 SINTERING OF CONSTRAINED FILMS

In the sintering of films on a rigid substrate there are two scenarios: fully constrained by a dense rigid substrate (where there is no shrinkage in the plane), and partially constrained by a densifying second layer. Figure 2.7 schematically illustrates the differences between "constrained" sintering and "co-fired" sintering.

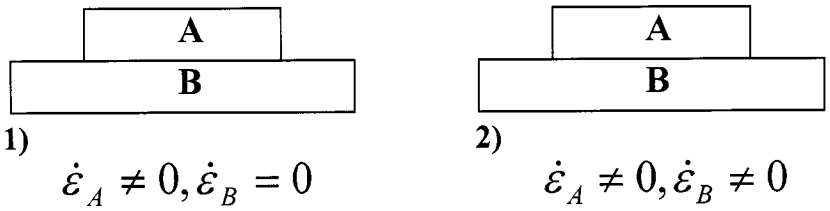

Figure 2.7 1) A constrained system where the substrate is a dense rigid body; 2) A co-fired system where the substrate is a densifying porous body.

II.4.1 Models of Sintering of Constrained Films

Scherer and Garino [16] analyzed the sintering of a porous glass film on a rigid substrate using a continuum mechanics model. By using constitutive equations for a porous viscous body and the difference in free strain rate between the film and the substrate, they modeled the constrained densification for the film. The relationship between constrained and free densification that Scherer and Garino developed is shown in Equation (2.9). K_p and G_p are the bulk and shear viscosities. Analysis for an isotropic sintering layer and an anisotropic sintering layer was shown. Their analysis predicted that there is little difference in the densification rate between isotropic and anisotropic films.

$$\left[\frac{\dot{\bar{p}}}{\bar{p}}\right]_{cons} = \frac{3K_p}{3(3K_p + 4G_p)}\left[\frac{\dot{\bar{p}}}{\bar{p}}\right]_{free} \tag{2.9}$$

Bordia and Raj [17] developed a model for the sintering behavior of a film constrained by a rigid substrate. They showed in their model that the generation of processing defects, and the rate of densification rate are related to a material property β. β is the ratio of the shear rate to the densification rate. They showed that the magnitude of the incompatibility stress depends on β and if the stresses are large enough they can lead to film failure. Their analysis showed that a higher value of β leads to stress relaxation by shear flow and results in lower stress, and reduced effect of the constraint. They used a viscoelastic model for the sintering film.

Hsueh [18] proposes a simplified solution to the constrained film on a rigid substrate problem. His model also used a viscoelastic formulation. The time independent elastic stresses are first assessed and then transformed into the time dependent viscoelastic solutions. Hsueh finds that the hydrostatic tension in the film is limited by the sintering stress, because sintering stops when the hydrostatic tension approaches the sintering

stress. Further, his calculations show that films with lower viscosities relax stresses faster and sinter at higher rates than films with high viscosities. This analysis applies to stresses far away from free ends.

Bordia and Scherer [19] compared the different models used in the analysis of constrained sintering and showed that the elastic effects are not significant. With this simplification, the predictions of the different models are similar for realistic values of the constitutive parameters.

Jagota and Hui [20, 21] examined the mechanics of sintering thin films. They analyzed the films as a compressible viscous fluid with a sliding interface between the film and substrate. By using a two dimensional analysis of the governing equations, they were able to analyze the effect that friction parameters had on the sintering film, including film velocity and radial stress. Further analysis allowed them to predict crack growth in a constrained film based on the friction parameter from their model.

Zhao and Dharani [22] developed a viscoelastic finite element model to simulate the constrained sintering of a ceramic film under constant heating rates. The sintering model is supposed to be applicable to any sintering film and film geometry. Using their model they calculated the thermal residual stresses present in the film. It was shown that cooling rates induce large normal tensile stresses in the film. It was also shown that the film does not densify uniformly, but rather the film near an edge or corner does not densify well and experiences large tensile stresses.

Carroll and Rahaman [23] developed a model to study initial stage sintering of constrained polycrystalline films. The model assumes uniform cubic packing of spherical particles. Analysis using their model showed that the densification rate of constrained thin films is highly dependant on the dihedral angle of the material and on

the grain growth. Grain growth was shown to reduce the sintering pressure. Significant grain growth can effectively stop film densification.

Bordia et al. [24] developed a general transversely isotropic viscous formulation for sintering bodies that takes into account anisotropic sintering behavior. Isotropic constitutive laws are not able to predict the sintering behavior of a constrained film, or sinter forged compact, that develops an anisotropic microstructure. The following describes the isotropic and anisotropic formulation of the constrained film models.

The isotropic constitutive behavior of the sintering viscous body is given by [25]:

$$\dot{\varepsilon}_i = \dot{\varepsilon}_i^{free} + \left(\frac{1}{E^p}\right)\left[\sigma_i - \nu^p\left(\sigma_j + \sigma_k\right)\right] \tag{2.10}$$

Where $\dot{\varepsilon}_i$ is the strain rate in the i direction, $\dot{\varepsilon}_i^{free}$ is the free sintering strain rate, E^p and ν_p are the uniaxial viscosity and the viscous Poisson's ratio, and σ_i, σ_j, and σ_k are the three principal stresses. Furthermore, assuming zero in-plane strain rate due to the constraint ($\dot{\varepsilon}_1 = \dot{\varepsilon}_2 = 0$), the in-plane stress and volumetric densification rate of the constrained film are given by Equations (2.11) and (2.12).

$$\sigma^{\infty} = -\frac{E^p \dot{\varepsilon}^{free}}{1-\nu^p} \tag{2.11}$$

$$\dot{\varepsilon}_3^{constr.} = \dot{\varepsilon}^{free}\left(\frac{1+\nu^p}{1-\nu^p}\right) \tag{2.12}$$

Equation (2.12) is for the volumetric densification of a constrained film (since there is no strain in the plane). The densification of a free film is three times the free

densification rate. Thus, Equation (2.13) shows the relationship between the densification rate of a free and constrained film.

$$\left(\frac{\dot{\rho}}{\rho}\right)^{constr.} = \frac{1+\nu^p}{(1-\nu^p)}\frac{1}{3}\left(\frac{\dot{\rho}}{\rho}\right)^{free} \tag{2.13}$$

Zero-radial strain rate sinter-forging experiments have shown that the microstructure of this analogous system becomes anisotropic [26]. From this analogous system, it is assumed that a constrained film will also develop an anisotropic microstructure. For this system a new general transversely isotropic viscous formulation for constrained sintering bodies that takes into account anisotropic sintering behavior has been developed by Bordia et al. [24]. For a transversely isotropic body, Equations (2.14) and (2.15) describe the strain rate of the body in the normal direction and the 1-2 plane which is the isotropic plane.

$$\dot{\varepsilon}_3 = \dot{\varepsilon}_3^{free} + \left(\frac{1}{E_3^p}\right)\left[\sigma_3 - \nu_{13}^p \frac{E_3^p}{E_1^p}(\sigma_1+\sigma_2)\right] \tag{2.14}$$

$$\dot{\varepsilon}_1 = \dot{\varepsilon}_2 = \dot{\varepsilon}_1^{free} + \left(\frac{1}{E_1^p}\right)\left[\sigma_1 - \nu_{12}^p\sigma_2 - \frac{E_1^p}{E_3^p}\nu_{31}^p\sigma_3\right] \tag{2.15}$$

Where $\dot{\varepsilon}_i^{free}$ is the free strain rate in the i direction, E_i^p is the uniaxial viscosity in the i direction, ν_{ij}^p is the appropriate viscous Poisson's ratio, σ_i is the stress and $\dot{\varepsilon}_i$ is the strain rate in the i direction. In a fully constrained film Equations 2.14 and 2.15 can be used to obtain the in-plane stress and volumetric densification.

$$\sigma^{\infty} = -\frac{E_1^p \dot{\varepsilon}_1^{free}}{1-\nu_{12}^p} \tag{2.16}$$

$$\dot{\varepsilon}_3^{constr.} = \dot{\varepsilon}_3^{free} + \frac{2\nu_{13}^p}{1-\nu_{12}^p}\dot{\varepsilon}_1^{free} \tag{2.17}$$

The constrained densification is no longer directly proportional to the free densification rate, since the in plane and axial components have been separated for the anisotropic analysis. Equation (2.18) relates the free densification rate to the constrained densification rate.

$$\left(\frac{\dot{\rho}}{\rho}\right)^{constr.} = \frac{\nu_{13}^p}{\left(1-\nu_{12}^p\right)}\left[\left(\frac{\dot{\rho}}{\rho}\right)^{free} + \dot{\varepsilon}_3^{free}\right] - \dot{\varepsilon}_3^{free} \tag{2.18}$$

II.4.2 Experimental Studies on the Sintering of Films Constrained by a Substrate

In a paper written by Garino and Bowen [27], that was intended to show experimentally their film preparation techniques and to compare their films sintering behavior with published models, showed an astute observation that clearly shows the effect of constraint on the densification of a film. They prepared a 30μm alumina film on a rigid dense substrate. After heating the film to 1000°C for one hour, they broke the sample in half, and then sintered to 1450°C for 1hr. The breaking step delaminated some of the film near the edge from the substrate, but the film remained intact. As can be seen in Figure 2.8 the portion of the film not adhered (or constrained) to the substrate is near full density, whereas the portion of the film constrained by the substrate is quite porous.

Figure 2.8 Visual proof of the effect of constraint on the densification of a film. The smooth portion of the film is not attached to the substrate. The porous portion is still adhered to the substrate. The film is intact [27].

Garino and Bowen [28] studied the densification of constrained and unconstrained glass and polycrystalline films and compared their results to the predictions from the Scherer and Garino model [16]. They sintered glass powder, alumina and zinc oxide powders in free and constrained geometries. The glass films will undergo viscous sintering, while the polycrystalline films will undergo solid-state sintering. Constrained film shrinkage was measured in-situ using laser reflectance, while the unconstrained densification was analyzed with SEM. They found that the model predicted the constrained film densification of the glass powder very well, with the anisotropic model matching a little better. Anisotropy was not found in the microstructure however. The polycrystalline

powders did not match the models well. They concluded that the model does not apply for polycrystalline films.

Choe et al. [29] studied the constrained sintering of a gold circuit paste on a substrate. They used an optical technique capable of measuring thickness during sintering of a constrained film, and a setup to measure the in-plane stresses generated in constrained-sintering films. They found that the level of stress in the constrained film was not large enough to explain the observed tenfold rate retardation in the film. Further, the densification rate retardation cannot be attributed to grain growth kinetics. They concluded that the reduction in sintering rate was due to reduction in stress as a driving force due to the constraint of grains to the substrate, as well as the change in dominant diffusion from grain-boundary to lattice diffusion.

Bang and Lu [30] measured the in-plane stresses that developed in a constrained borosilicate glass film during sintering. The 0.6mm thick films were constrained by a dense silicon substrate. A very thin substrate was used in order to measure the substrate curvatures. The curvature of the substrate was measured in order to calculate the in-plane sintering stress. The maximum measured tensile stresses were around 20 kPa for the initial stage of sintering which corresponds well with the Bordia and Jagota model [31]. Using the in-plane stress, the calculated hydrostatic stress came out to 13 kPa, which correlates well with hydrostatic stress calculated from Scherer and Garino's analysis [16]. It was also shown that the stress had no effect of the densification up to 90% density. However, the stress did have measurable effect on the final stage sintering.

Busso et al. [32] experimentally measured the average grain size and relative density development of a screen-printed LSM film onto a rigid dense YSZ substrate. Calculations were made to model the behavior of the system they were testing experimentally. They found that their data reached good agreement with the Du [33, 34]

and Besson [35] models. One thing they did notice from the models is that a significant amount of densification and grain growth occurs during heat up before isothermal, as well as during cooldown after isothermal for the high temperature isothermal samples. The radius of curvature measured after their experiment was 1000 times larger than predicted. They found that most of the stress in the film was relieved by micro-cracks.

Stech et al. [36] characterized sintered nanocrystalline TiO_2 films of thickness 140 or 65nm. The TiO_2 films were sintered on muscovite at 600° and 900°C from 10min to 25h. They found that the grain growth stopped at a similar size to that of the thickness of the film. The film thickness actually limited grain growth in all of their experiments. As density increased grain size was shown to increase. Pore size was shown to plateau at about 75% density, but grain growth continued. This suggests that the inter-pore distance was growing.

Lin and Jean [37] studied the densification behavior of silver circuit paste under constrained sintering on a rigid silicon substrate. The stress data collected was compared to the calculated stress from the viscous analogy for the constitutive equations of a porous sintering material of Bordia and Scherer [19, 25, 38]. They first noticed that the stress in the film rose sharply during the initial stage of sintering, then leveled out and was sustained for the remainder of the sintering. The stress was also shown to increase as a function of sintering temperature, a sign of increased densification rate. The densification mechanism was shown to change from grain-boundary diffusion in free films to lattice diffusion in constrained films. This change in densification mechanism and the increased film tensile stress both contributed to the decrease in constrained film densification rate.

II.5 CO-FIRED FILMS: EXPERIMENTAL RESULTS & MODELLING

In co-fired ceramic systems, such as a planar co-fired SOFC system or a Low Temperature Co-fired Ceramic system (LTCC), the greatest threats to producing flat defect free samples is: the difference in densification rates of the materials, and the difference in the coefficient of thermal expansion. Most of the stress analysis, modeling, and constrained sintering rate prediction of the previous section are all applicable to co-fired systems. In this section an overview of the literature on the processing of co-fired systems is provided.

Majumdar et al. [39] analyzed the stress and fracture of a three layer co-fired system due to mismatch of thermal expansion coefficients. The system that they studied was the SOFC three layer system of NiO/YSZ, YSZ, and LSM. The three layers were tape cast and pressed together, and then sintered. Using different thicknesses for the different layers, varying the NiO content of the anode, and by varying the porosity of the anode they were able to develop a fracture model of the three-layer SOFC tape system. Their model matched well with their experimental data. There were failures of the films during cool down due to mismatch in coefficients of thermal expansion. They found that a small difference in the CTE can lead to very high stresses in the tri-layer. By increasing the porosity of the anode, and tailoring the distribution of NiO, the fracture probability can be greatly reduced.

Cheng and Raj [40] also studied theoretically and experimentally a three layer co-fired system. Their system was that of two ceramic films sandwiching a metal film. The ceramic was either Titania or glass powder and the metal was palladium. They found that the layer that is stressed in tension in the early stages of sintering is most likely to fracture during sintering. Their theoretical prediction that glass/metal/glass films would not develop defects because of a high value of shear relaxation in glass was confirmed

by their experiments. Their model shows that the likelihood of developing a tensile stress in the multilayer only depends on the geometry, green density, and the ratio of intrinsic sintering pressures. Available models were adequate in predicting stresses in the films.

Lu et al. [41] studied the sintering kinetics of a multi-layer co-fired system consisting of metal/ceramic/glass, and its effect on the camber of the system. The linear shrinkage of the system was studied using non-contact optical scanning equipment that would measure the width of the sample many times during sintering. Their initial experimental results showed that the sintering rate of the free and co-fired thick gold films was very different. They noticed that the gold film in the co-fired system would not even start to densify before the free sintered gold film had already reached full density. The stresses that developed from a mismatch in the sintering rate of the materials led the materials to constrain the others during sintering. This constraint developed stresses, which in turn was responsible for camber development.

Jean and Chang [42-44] analyzed a Silver electrode co-fired with Barium Titanate dielectric processed via tape-casting, screen-printing, and laminating. In a subsequent paper they also evaluated a Ni-based ceramic-filled glass packaging system using the same method [45]. For the Nickel system they evaluated the samples they processed, and compared their experimental observations with their analysis of camber developing during sintering. Camber development during sintering for this system was very interesting. As the sample heated up it would develop positive camber, then would return to level, than at elevated temperature it would develop negative camber. These camber developments, and the stresses involved, are attributed to the densification mismatches in the system. Mathematical analysis of the system based on a viscous model showed significant agreement with the experimental data. In the Ag system they found that there was grain-boundary diffusion as well as viscous flow of glass, but their experimental data still matched well with the viscous model.

Cai et al. [46] investigated hybrid ceramic laminates of Magnesium oxide doped Alumina and Ceria doped Zirconia of different thickness. The tapes cast layers were stacked together in symmetric and asymmetric sequences and sintered. Channel cracks, debonding cracks, and edge cracks were observed in the symmetric laminates. Debonding cracks and interlayer cracks were observed in the asymmetrical laminates. Most of the damage was observed in the Zirconia based layer. The Zirconia layer would densify at a lower temperature so it would be under a tensile stress from the alumina layer that had not yet sintered. This tensile stress, and the lower strength of the Zirconia layer led to many of the cracks. This mismatch led to curling of the bi-layer systems. The asymmetrical layers, where one layer is thicker than the other, were less prone to curling. Another test was done where there were many films of alternating composition sintered in a laminate. The Zirconia layer was varied from sample to sample with different amounts of the alumina powder. The presence of just 10% of alumina powder greatly reduced the stress, and in turn defects in the system. This result showed that the CTE mismatch played a major role in controlling the tendency to form defects. The extent of the cracking in both systems could be reduced or eliminated through stress relaxation, or better matching of the sintering rates and thermal expansions of the constituents.

II.6 CRACKS AND DAMAGE IN CONSTRAINED AND CO-FIRED FILMS

A very important possible effect of the stresses generated due to incompatible densification rates is the generation and growth of processing defects. In this section, the available literature relevant to this affect is reviewed.

II.6.1 Modeling of Cracks and Damage in Constrained and Co-Fired Films

Bordia and Jagota [31] developed the first comprehensive model for crack growth in constrained films. They showed that the growth of pre-existing flaws during constrained sintering depends on three factors: the initial crack length, the film thickness, and the friction at the interface between the film and the substrate. They averaged the in-plane stress through the thickness and attained a combined parameter, R, to quantify the effect of the friction and film thickness. In their analysis they were able to obtain a failure map with these two parameters (R and crack length) and able to identify regions of crack growth. This map is shown in Figure 2.9.

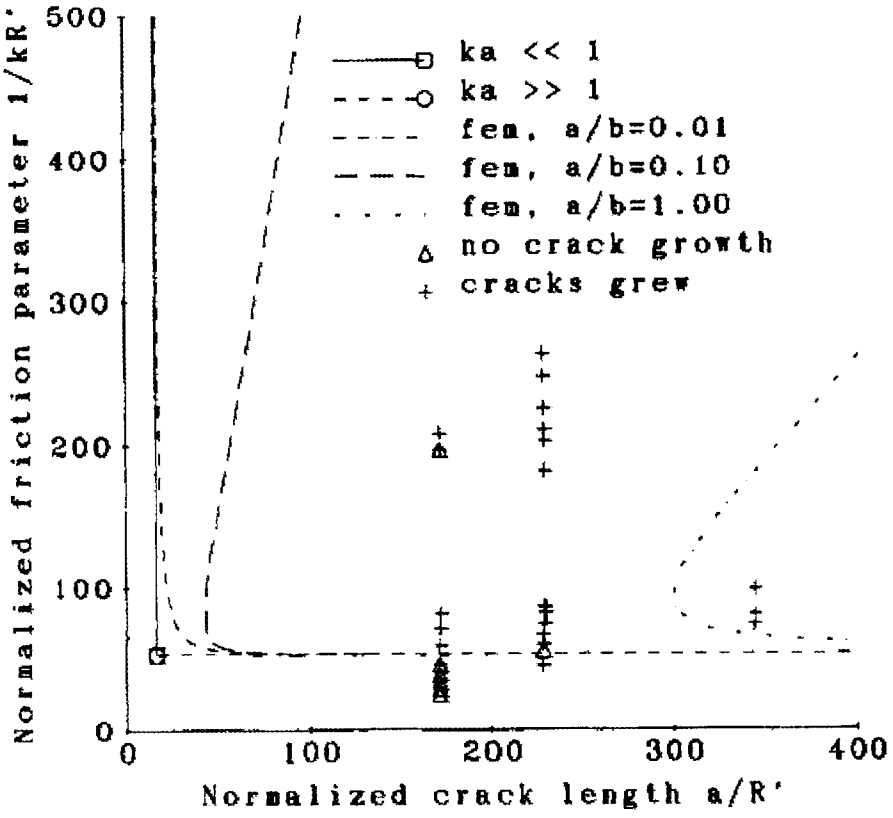

Figure 2.9 Crack growth map for a sintering film[31]

One important parameter to predict crack growth is the fracture criteria for porous ceramics. Zimmerman et al. [47] analyzed the fracture of alumina samples with artificially introduced pores. They found that spherical cavities act as stress concentrators and promote micro-cracks in the matrix. Existing models for fracture in brittle solids were evaluated with this data and extended to develop failure criteria for porous bodies based on fracture mechanics.

Maximenko and Biest [48] developed a model for predicting the development of damage in a constrained film during sintering. They approached this problem by homogenizing all sintering behavior in a film into just one single neck between particles and applying it to the whole film. Using their analysis, they propose that they can predict the necessary level of external pressure or variation of the geometrical structure of the composite to avoid damage formation. The model they presented predicts only the macroscopic behavior of the powder and cannot follow mesoscopic structural changes in damaged material.

II.6.2 Experimental Results on Cracks and Damage in Constrained and Co-Fired Films

Bordia and Jagota [31] studied the effect that constraint has on the development of artificially introduced cracks into glass and alumina films. They introduced these defects using a glass blade to cut into the film. This study was to experimentally validate the analysis presented in this paper. In order to vary the interface friction parameter, they constrained the films with different substrates. Their study of the growth of cracks showed that there is a critical friction parameter that controls the growth of cracks in the glass films. The experimental results on alumina films were not as conclusive due to the difficulties in introducing sharp cracks.

Flinn et al. [49] studied the evolution of the defect size and strength of alumina compacts that included controlled sized pores. They used an alumina powder with polystyrene spheres of controlled sizes to introduce defects into their samples. First they sintered the samples to controlled densities and evaluated the pore development. They found that the pore size evolved in a linear fashion with density. Next they tested the fracture strength of the samples with the different controlled pore sizes. They observed a weak dependence of the strength on the pore size, even though the fracture initiated at the pores.

II.7 SINTER FORGING

De Jonghe and Rahaman [50, 51] built and demonstrated the first loading dilatometer in 1984. The loading dilatometer was capable of applying a controlled uniaxial stress to a powder compact while sintering it. Further, the loading dilatometer could measure the axial strain of the sintering sample during sintering. Their study of Cadmium Oxide showed that the densification rate and uniaxial creep decreased with time, but the densification rate was independent of stress. They applied relatively low uniaxial stresses. Rahaman and De Jonghe continued studying the sintering of Cadmium Oxide on their loading dilatometer [52, 53]. They observed the simultaneous effect of creep and sintering in their samples. When compared to free sintered data, they could separate the creep from the sintering stress and develop a relationship between the creep rate, sintering stress and density. Their analysis showed that grain boundary diffusion is the rate controlling step in both creep and densification.

Later, Bordia [54] and Venkatachari and Raj [55] further developed a sinter-forging unit capable of also measuring the radial strain of the sintering powder compact in addition to the axial strain and capable of applying larger stresses. Using this system, Bordia was able to quantify the effect of uniaxial stress on densification and creep, and Venkatachari and Raj studied the enhancement of the strength of powder compacts

processed with this system. Through uniaxially loading a sample they showed that the pores in a sample could be reduced in size, and further removed during sintering. This reduction in sintering flaws markedly increased the strength of the sinter-forged sample.

II.7.1 Experimental Studies on Effect of Sinter-Forging on Microstructure and Mechanical Properties

He et al. [56] investigated the ability to increase the mechanical properties of zirconia-toughened alumina by sinter forging. They sintered both pressureless and sinter forged compacts of 85 wt% alumina and 15 wt% zirconia. The bending strength was measured using a four-point bend test, and fracture toughness using a three-point single-edge notched beam. The fracture surfaces were analyzed using SEM. The sinter forging of the samples showed a large increase of strength and toughness, up to a factor of 1.5-2 compared to the pressureless samples. The fracture energy was increased by a factor of two. Their microstructural analysis showed that the predominant mechanism for increasing the strength of the samples was through grain boundary strengthening. A 40 MPa stress could effectively remove all of the processing flaws otherwise seen in the pressureless samples. This group later studied the enhanced mechanical properties of ultra-fine-grained TZP by grain boundary strengthening [57]. Of particular note, they showed that sinter forging increased grain boundary strength by suppressing impurity segregation, and preventing a continuous impurity forming at the boundary. Instead, the sinter forging forces the impurities to segregate at grain boundary intersections, maintaining much stronger grain boundaries.

Skandan et al. [58] studied the effect that an applied stress through sinter forging had on the densification of a nano-powder zirconia. After processing their nanopowder through inert gas condensation, the powder compacts were sinter forged with varying loads at similar heating profiles. Their experiments showed a direct correlation between the relative density and the applied pressure above 10MPa. The increased sintering rate

prevented large amounts of coarsening, so final grain sizes were still kept below 45nm. Samples above 99% density were made with this process.

Boutz et al. [59] studied the characteristics of low-temperature sinter-forged nanostructured Y-TZP and YCe-TZP. Compacts of these materials were sinter-forged at varying pressures between 1100° and 1200°C. Sinter-forged samples at these temperatures could reach an equivalent density 20-600 times faster than the non-loaded samples. They also observed that the creep strains imposed on the samples during sintering were effective in eliminating residual flaws. The size and number of observed flaws decreased as the strain increased. At the temperature these samples were sintered, all flaws (pores) could not be removed. Similarly to Panda et al. [60], the densification and creep rate show a non-linear relationship to applied load.

Hague and Mayo [61] studied the densification mechanisms for both small inter-crystalline pores, and large inter-agglomerate pores. Their system was sinter-forged nanocrystalline zirconia. Their results showed that large pores were only removed through plastic strain, while the small pores were removed via diffusion mechanisms. They found that grain growth during sintering was limited by the porosity during intermediate stage densification. To minimize grain growth during densification, they showed that high strain rates are effective in closing large pores and increasing density at lower temperatures, while small pores are still present to restrict grain growth.

Owen and Chokshi [62] studied the final stage free sintering and sinter forging behavior of a yttria stabilized tetragonal zirconia powder. This comprehensive study, amongst other things, evaluated the parameters for densification and deformation. They found that the application of a uniaxial load significantly increased the rate of densification for their 3 mol% YSZ compacts. Their analysis showed that the densification was proportional to the square of the stress.

Zuo et al. [63] evaluated the microstructural evolution of sinter forged samples, and the free sintering behavior of partially sinter forged samples. For their experiment a new sinter forger was developed that utilizes high-resolution laser scanners to measure the radial dimensions of the sample during sintering, instead of the contact systems previously used. Samples of alumina were sintered at various loads up to 80% relative density. Their microstructure was analyzed for pore orientation. They found that the pore orientation would become parallel to the loading direction at high loads. In addition, samples were sinter forged to 80% relative density and were subsequently free sintered to investigate the anisotropy in densification behavior. The sintering strain in the radial and axial direction was measured for these samples. The samples that were sinter forged at higher loads were found to have larger radial and axial strains during free sintering. The higher loaded samples also were shown to have higher densification rates.

II.7.2 Use of Sinter-Forging to Measure Constitutive Parameters

Panda et al. [60] Sinter-Forged fine grained Zirconia/Yttria (2.85 mol%) powder with a constant axial displacement rate. The samples were forged with varying displacement rates. When the densification rate is plotted versus hydrostatic pressure the curve is very non-linear. If densification were taking place by diffusional transport, than this line would be linearly proportional to the negative intercept along the pressure axis, the magnitude of which would be equal to the sintering pressure. This leads to the conclusion that densification is being accomplished by dislocation plastic flow rather than diffusion. This is contrary to what has been shown for other materials such as silicon nitride and alumina. However, in this study, much larger stresses were used and this postulated to be the reason for the non-linearity.

Chu et al. [64] used a loading dilatometer to determine the relationship between the densification-rate to creep-rate ratio with temperature. Using zinc oxide and alumina

powder compacts they sintered the samples at constant heating rates and constant isothermal conditions. The samples were either sintered with no load, or a small stress. Using Rahaman and De Jonghe's method [52, 53], they could separate creep and sintering stress to aid their analysis. Their study found that the densification/creep rate ratio was fairly independent of temperature. This shows that there is little benefit to be expected from non-isothermal sintering schemes.

Bordia and Raj [65] used sinter-forging to obtain the creep and densification viscosities of fine grained TiO_2 under isothermal conditions. Their results were used in comparing their experimental results on the densification of composites to the model that they had developed for the densification of particulate reinforced composites [66]. They also showed that low uniaxial stresses can significantly enhance the densification behavior of composites [67].

Cai at el. [68] developed a cyclical loading dilatometry technique to measure the constitutive properties of the sample. By selecting appropriate loading and temperature profiles, Young's modulus and uniaxial viscosity could be determined. Because of the intermittent nature of the loading during sintering, one run can be used to determine the elastic and viscous properties at any temperature for a sample. Their experiments on alumina and zirconia samples showed that they behave elastic below 950°C, but become viscous above that.

Zuo et al. [69, 70] in two studies experimentally determined the sintering stresses, sintering viscosities and the Viscous Poisson's coefficient of alumina compacts through discontinuous sinter forging. Discontinuous sinter forging was used to prevent the microstructural bias caused by continuous uniaxial loads. Their microstructural analysis of the sinter-forged samples with constant stress showed anisotropic behavior and reduced grain growth, invalidating the viscous analogy using density as the sole microstructural variable. The measured viscosities matched up well with Rahaman and

the Ventakachari models [53, 71]. The viscous Poisson's ratio was also measured quite accurately with discontinuous sinter forging. Samples were first free sintered to a desired temperature, and then sinter forged with a desired load while measuring the strain on the sample. The varying starting densities gave accurate measurements from unbiased microstructures. The measured viscous Poisson's coefficient matched up well with Venkatachari's model [71].

In a subsequent study, Zuo et al. [26] used a sinter forger to sinter a low-temperature cofired ceramic system with zero-radial shrinkage. To maintain a zero-radial strain rate for the cofired ceramic system the uniaxial load had to be constantly adjusted to compensate for the changing sintering stress. This is the first time this technique has been demonstrated for the entire sintering cycle.

II.7.3 Analysis of Sinter-Forging

An interesting sinter-forging experiment with direct analogy to constrained densification is "zero-radial strain rate" sinter-forging. In this experiment, a body is sintered under an applied uniaxial stress (σ_3) such that the strain rate perpendicular to the applied stress is equal to zero (i.e. $\dot{\varepsilon}_2 = \dot{\varepsilon}_3 = 0$). Using the isotropic constitutive models [25], the axial stress required to sinter-forge a sample with zero radial strain can be described as the following:

$$\sigma_3 = \frac{E^p \dot{\varepsilon}^{free}}{\nu^p} = \frac{\Sigma(1-2\nu^p)}{\nu^p} \qquad (2.19)$$

Where $\dot{\varepsilon}^{free}$ is the free sintering strain rate (in the absence of stress), E^p is the uniaxial viscosity, ν^p is the viscous Poisson's ratio and Σ is the sintering potential. Using this, the axial strain rate can be calculated as:

$$\dot{\varepsilon}_3 = \frac{1+\nu^p}{\nu^p}\dot{\varepsilon}^{free} \tag{2.20}$$

This analysis does not however take into consideration possible anisotropic microstructural evolution. This study has shown that microstructures do develop anisotropically during sinter-forging. Bordia et al. [24] developed a transversely isotropic viscous formulation for sintering bodies that takes into account anisotropic sintering behavior.

To fully describe the sintering behavior of transversely isotropic viscous bodies, five independent viscous sintering parameters and two free sintering strain rates are needed as a function of microstructure. In the case of the sinter forging experiment to maintain a zero radial strain on a sample during sintering, the new transversely isotropic model calculates the axial stress needed as follows:

$$\sigma_3 = \frac{E_3^p \dot{\varepsilon}_1^{free}}{\nu_{31}^p} \tag{2.21}$$

$$\dot{\varepsilon}_3 = \dot{\varepsilon}^{free} + \frac{1}{\nu_{31}^p}\dot{\varepsilon}^{free} \tag{2.22}$$

Where $\dot{\varepsilon}_i^{free}$ is the free strain rate (in the absence of stress), and E_i^p is the uniaxial viscosity in the i direction. ν_{ij}^p is the appropriate viscous Poisson's ratio and σ_3 and $\dot{\varepsilon}_3$ are the stress and strain respectively in the 3-direction (axial direction).

Notes to Chapter II

1. Nernst, W., *Verfahren zur erzeugung von elektrischem gluhlicht.* DRP 104 872, filed 6.7.1897, 1899.

2. Haber, F., *Verfahren zur erzeugung von elektrischer energie aus kohle und gasformigen brennstoffen.* Oster Pat 27 743, filed 5.8.1905, 1907.

3. Baur, E. and WD, T., Brennstoffelement. DRP 325 783, filed 20.9.1916, 1920.

4. Baur, E. and Preis, H., *Fuel cells with rigid conductors.* Zeitschrift fuer Elektrochemie und Angewandte Physikalische Chemie, 1937. 43: p. 727-32.

5. Blomen, L.J.M.J. and Mugerwa, M.N., *Fuel cell systems* 1993, New York :: Plenum Press. xix, 614 p. :.

6. Wagner, C., *The mechanism of electric conduction in the nernst glower.* Naturwissenschaften, 1943. 31: p. 265-8.

7. Nernst, W., *Material for electric-lamp glowers.* US-P 685 730, filed 24.8.1899, 1901.

8. Hund, F., *Anomalous solid solutions in the system zirconia-yttria. Crystal structure of nernst glowers.* Zeitschrift fuer Elektrochemie und Angewandte Physikalische Chemie, 1951. 55: p. 363-6.

9. Iacomini, D.C.S., *Http://ares.Ame.Arizona.Edu/materials/crystal.Html.*

10. Yashima, M., Kakihana, M. and Yoshimura, M., *Metastable-stable phase diagrams in the zirconia-containing systems utilized in solid-oxide fuel cell application.* Solid State Ionics, 1996. 86-88(Part 2): p. 1131-1149.

11. Ondik, H.M., McMurdie, H.F., Clevinger, M.A. and Cedeno, C.L., *Phase diagrams for zirconium and zirconia systems* 1998, Westerville, Ohio :: American Ceramic Society. viii, 525 p. :.

12. Raj, R., *Analysis of the sintering pressure.* Journal of the American Ceramic Society, 1987. 70(9): p. C/210-C/211.

13. Coble, R.L., *Sintering crystalline solids. Ii. Experimental test of diffusion models in powder compacts.* Journal of Applied Physics, 1961. 32: p. 793-9.

14. Coble, R.L., *Sintering crystalline solids. I. Intermediate- and final-state diffusion models.* Journal of Applied Physics, 1961. 32: p. 787-92.

15. Ashby, M.F., *Sintering diagrams.* Acta Metallurgica, 1974. 22(3): p. 275-89.

16. Scherer, G.W. and Garino, T., *Viscous sintering on a rigid substrate.* Journal of the American Ceramic Society, 1985. 68(4): p. 216-220.

17. Bordia, R.K. and Raj, R., *Sintering behavior of ceramic films constrained by a rigid substrate.* Journal of the American Ceramic Society, 1985. 68(6): p. 287-292.

18. Hsueh, C.H., *Sintering of a ceramic film on a rigid substrate.* Scripta Metallurgica, 1985. 19(10): p. 1213-1217.

19. Bordia, R.K. and Scherer, G.W., *On constrained sintering-i. Constitutive model for a sintering body.* Acta Metallurgica, 1988. 36(9): p. 2393-2397.

20. Jagota, A. and Hui, C.Y., *Mechanics of sintering thin films. Ii. Cracking due to self-stress.* Mechanics of Materials, 1991. 11(3): p. 221-234.

21. Jagota, A. and Hui, C.Y., *Mechanics of sintering thin films. I. Formulation and analytical results.* Mechanics of Materials, 1990. 9(2): p. 107-119.

22. Zhao, Y. and Dharani, L.R., *Theoretical model for the analysis of a ceramic thin film sintering on a non-sintering substrate.* Thin Solid Films, 1994. 245(1-2): p. 109-114.

23. Carroll, D.R. and Rahaman, M.N., *An initial stage model for the sintering of constrained polycrystalline thin films.* Journal of the European Ceramic Society, 1994. 14(5): p. 473-9.

24. Bordia, R.K., Zuo, R., Guillon, O., Salamone, S.M. and Rodel, J., *Anisotropic constitutive laws for sintering bodies.* Acta Materialia, 2006. 54(1): p. 111-118.

25. Bordia, R.K. and Scherer, G.W., *On constrained sintering-ii. Comparison of constitutive models.* Acta Metallurgica, 1988. 36(9): p. 2399-2409.

26. Zuo, R., Aulbach, E. and Rodel, J., *Shrinkage-free sintering of low-temperature cofired ceramics by loading dilatometry.* Journal of the American Ceramic Society, 2004. 87(3): p. 526-8.

27. Garino, T.J. and Bowen, H.K., *Deposition and sintering of particle films on a rigid substrate.* Journal of the American Ceramic Society, 1987. 70(11): p. 315-317.

28. Garino, T.J. and Bowen, H.K., *Kinetics of constrained-film sintering.* Journal of the American Ceramic Society, 1990. 73(2): p. 251-7.

29. Choe, J.W., Calata, J.N. and Lu, G.-Q., *Constrained-film sintering of a gold circuit paste.* Journal of Materials Research, 1995. 10(4): p. 986-994.

30. Bang, J. and Lu, G.-Q., *Constrained-film sintering of a borosilicate glass: In situ measurement of film stresses.* Journal of the American Ceramic Society, 1995. 78(3): p. 813-815.

31. Bordia, R.K. and Jagota, A., *Crack growth and damage in constrained sintering films.* Journal of the American Ceramic Society, 1993. 76(10): p. 2475-2485.

32. Busso, E.P., Travis, R.P. and Chandra, L., *Residual stress generation during constrained sintering of layered ceramic thin film structures.* Materials Research Society Symposium Proceedings, 1998. 505(Thin-Films--Stresses and Mechanical Properties VII): p. 547-552.

33. Du, Z.Z. and Cocks, A.C.F., *Constitutive models for the sintering of ceramic components - ii. Sintering of inhomogeneous bodies.* Acta Metallurgica et Materialia, 1992. 40(8): p. 1981-94.

34. Du, Z.Z. and Cocks, A.C.F., *Constitutive models for the sintering of ceramic components - i. Material models.* Acta Metallurgica et Materialia, 1992. 40(8): p. 1969-79.

35. Besson, J. and Abouaf, M., *Rheology of porous alumina and simulation of hot isostatic pressing.* Journal of the American Ceramic Society, 1992. 75(8): p. 2165-72.

36. Stech, M., Reynders, P. and Roedel, J., *Constrained film sintering of nanocrystalline tio2.* Journal of the American Ceramic Society, 2000. 83(8): p. 1889-1896.

37. Lin, Y.-C. and Jean, J.-H., *Constrained sintering of silver circuit paste.* Journal of the American Ceramic Society, 2004. 87(2): p. 187-191.

38. Bordia, R.K. and Scherer, G.W., *On constrained sintering-iii. Rigid inclusions.* Acta Metallurgica, 1988. 36(9): p. 2411-2416.

39. Majumdar, S., Claar, T. and Flandermeyer, B., *Stress and fracture behavior of monolithic fuel cell tapes.* Journal of the American Ceramic Society, 1986. 69(8): p. 628-633.

40. Cheng, T. and Raj, R., *Flaw generation during constrained sintering of metal-ceramic and metal. Glass multilayer films.* Journal of the American Ceramic Society, 1989. 72(9): p. 1649-1655.

41. Lu, G.Q., Sutterlin, R.C. and Gupta, T.K., *Effect of mismatched sintering kinetics on camber in a low-temperature cofired ceramic package.* Journal of the American Ceramic Society, 1993. 76(8): p. 1907-14.

42. Chang, C.-R. and Jean, J.-H., *Effects of silver-paste formulation on camber development during the cofiring of a silver-based, low-temperature-cofired ceramic package.* Journal of the American Ceramic Society, 1998. 81(11): p. 2805-2814.

43. Jean, J.-H. and Chang, C.-R., *Cofiring kinetics and mechanisms of an ag-metalized ceramic-filled glass electronic package.* Journal of the American Ceramic Society, 1997. 80(12): p. 3084-3092.

44. Jean, J.-H. and Chang, C.-R., *Camber development during cofiring ag-based low-dielectric-constant ceramic package.* Journal of Materials Research, 1997. 12(10): p. 2743-2750.

45. Jean, J.-H., Chang, C.-R. and Chen, Z.-C., *Effect of densification mismatch on camber development during cofiring of nickel-based multilayer ceramic capacitors.* Journal of the American Ceramic Society, 1997. 80(9): p. 2401-2406.

46. Cai, P.Z., Green, D.J. and Messing, G.L., *Constrained densification of alumina/zirconia hybrid laminates, i: Experimental observations of processing defects.* Journal of the American Ceramic Society, 1997. 80(8): p. 1929-1939.

47. Zimmermann, A., Hoffman, M., Flinn, B.D., Bordia, R.K., Chuang, T.-J., Fuller, E.R., Jr. and Roedel, J., *Fracture of alumina with controlled pores.* Journal of the American Ceramic Society, 1998. 81(9): p. 2449-2457.

48. Maximenko, A.L. and Van Der Biest, O., *Modelling of damage development during sintering.* Journal of the European Ceramic Society, 2001. 21(8): p. 1061-1071.

49. Flinn, B.D., Bordia, R.K., Zimmermann, A. and Rodel, J., *Evolution of defect size and strength of porous alumina during sintering.* Journal of the European Ceramic Society, 2000. 20(14-15): p. 2561-2568.

50. De Jonghe, L.C. and Rahaman, M.N., *Loading dilatometer.* Review of Scientific Instruments, 1984. 55(12): p. 2007-10.

51. Rahaman, M.M. and De Jonghe, L.C., *Sintering of cadmium oxide under low applied stress.* Journal of the American Ceramic Society, 1984. 67(10): p. C205-C207.

52. Rahaman, M.N., De Jonghe, L.C. and Brook, R.J., *Effect of shear stress on sintering.* Journal of the American Ceramic Society, 1986. 69(1): p. 53-58.

53. Rahaman, M.N., De Jonghe, L.C. and Hsueh, C.H., *Creep during sintering of porous compacts.* Journal of the American Ceramic Society, 1986. 69(1): p. 58-60.

54. Bordia, R., *Sintering of inhomogenous or constrained powder compacts: Modelling and experiments*. 1986, Cornell University.

55. Venkatachari, K.R. and Raj, R., *Enhancement of strength through sinter forging.* Journal of the American Ceramic Society, 1987. 70(7): p. 514-520.

56. He, Y.J., Winnubst, A.J.A., Verweij, H. and Burggraaf, A.J., *Improvement of mechanical properties of zirconia-toughened alumina by sinter forging.* Journal of Materials Science, 1994. 29(22): p. 5868-74.

57. He, Y.J., Winnubst, A.J.A., Sagel-Ransijn, C.D., Burggraaf, A.J. and Verweij, H., *Enhanced mechanical properties by grain boundary strengthening in ultra-fine-grained tzp ceramics.* Journal of the European Ceramic Society, 1996. 16(6): p. 601-612.

58. Skandan, G., Hahn, H., Kear, B.H., Roddy, M. and Cannon, W.R., *Effect of applied stress on densification of nanostructured zirconia during sinter-forging.* Materials Letters, 1994. 20(5-6): p. 305-309.

59. Boutz, M.M., Winnubst, L., Burggraaf, A.J., Nauer, M. and Carry, C., *Low-temperature sinter forging of nanostructured y-tzp and yce-tzp.* Journal of the American Ceramic Society, 1995. 78(1): p. 121-128.

60. Panda, P.C., Wang, J. and Raj, R., *Sinter-forging characteristics of fine-grained zirconia.* Journal of the American Ceramic Society, 1988. 71(12): p. 507-509.

61. Hague, D.C. and Mayo, M.J., *Sinter-forging of nanocrystalline zirconia: I, experimental.* Journal of the American Ceramic Society, 1997. 80(1): p. 149-156.

62. Owen, D.M. and Chokshi, A.H., *Final stage free sintering and sinter forging behavior of a yttria-stabilized tetragonal zirconia.* Acta Materialia, 1998. 46(2): p. 719-29.

63. Zuo, R., Aulbach, E., Bordia, R.K. and Roedel, J., *Critical evaluation of hot forging experiments: Case study in alumina.* Journal of the American Ceramic Society, 2003. 86(7): p. 1099-1105.

64. Chu, M.-Y., De Jonghe, L.C. and Rahaman, M.N., *Effect of temperature on the densification/creep viscosity during sintering.* Acta Metallurgica, 1989. 37(5): p. 1415-1420.

65. Bordia, R.K. and Raj, R., *Sintering and titania-alumina composites: A model experimental investigation.* Journal of the American Ceramic Society, 1988. 71(4): p. 302-10.

66. Raj, R. and Bordia, R., *Sintering behavior of bi-modal powder compacts.* Acta Metallurgica, 1984. 32(7): p. 1003-1019.

67. Bordia, R.K. and Raj, R., *Hot isostatic pressing of ceramic/ceramic composites at pressures <10 mpa.* Advanced Ceramic Materials, 1988. 3(2): p. 122-6.

68. Cai, P.Z., Messing, G.L. and Green, D.L., *Determination of the mechanical response of sintering compacts by cyclic loading dilatometry.* Journal of the American Ceramic Society, 1997. 80(2): p. 445-452.

69. Zuo, R., Aulbach, E. and Rodel, J., *Experimental determination of sintering stresses and sintering viscosities.* Acta Materialia, 2003. 51(15): p. 4563-4574.

70. Zuo, R., Aulbach, E. and Roedel, J., *Viscous poisson's coefficient determined by discontinuous hot forging.* Journal of Materials Research, 2003. 18(9): p. 2170-2176.

71. Venkatachari, K.R. and Raj, R., *Shear deformation and densification of powder compacts.* Journal of the American Ceramic Society, 1986. 69(6): p. 499-506.

CHAPTER III

SCOPE OF THIS RESEARCH

The goal of this study is to investigate the microstructural development and evolution of defects in ceramics that are undergoing a modification of their densification during sintering through an external applied stress or constraint. The first part of this study will be accomplished with tape cast and slip cast 8 mole % YSZ. The samples will be sinter-forged using a sinter-forger built for this study. The anisotropy of the microstructure will be characterized by focusing on the pore development. The pore development will be analyzed using ImageJ. Further investigation of pore development will be done with slip cast compacts with fine, controlled sized pores introduced to compare the evolution of intrinsic and extrinsic pores.

The second part of this study is focused on understanding the effect that the constraint has on the development of defects during sintering in a fully constrained YSZ film. Artificial defects will be introduced into centrifugally cast 8 mol% YSZ films constrained by varying substrates. These defects will be introduced into the green film utilizing a Focused Ion Beam. The focus will be on the development of a fundamental understanding of the effect of various parameters on the growth of defects in constrained films.

The results of this work will provide a detailed understanding of the development of anisotropic microstructures and growth of defects in ceramics sintered under external or internal stresses. The internal stresses are generated due to the constraint.

CHAPTER IV

EXPERIMENTAL TECHNIQUES

IV.1 MATERIALS

IV.1.1 Powder

The powder used for most experiments was as-received Yttria Stabilized Zirconia (YSZ) from Tosoh Corporation. The YSZ powder, TZ-8Y, is 92 mole percent ZrO_2 and 8 mol percent Y_2O_3. It has a specific surface area of 16 m^2/g. The median particle diameter ($D_{(50)}$ By Vol.) is 0.58μm. The theoretical density of TZ-8Y is 5.90 g/c^3.

For the pore behavior transition study a smaller powder is used to determine dependence on particle size. For this experiment an as-received YSZ-8 was used from Fuel Cell Materials Inc. with same composition as the TZ-8Y. The specific surface area of the powder is 6.1m^2/g (this is a tape cast grade YSZ powder). The median particle diameter ($D_{(50)}$ By Vol.) is 0.25μm. The theoretical density for the YSZ-8 is the same as TZ-8Y.

IV.1.2 Binder

In order to increase the mechanical strength of the green compacts, a binder is commonly used. The binder material used in this study is Polyethylene Glycol (PEG). The PEG used for any samples made by me was bought from DOW Carbowax products Inc. The chemical formula for PEG is shown in Equation (4.1), 'n' is the number of oxyethylene groups and it controls the molecular weight of the polymer. For all samples except the tape cast one, a PEG with a value of n equal to 3000 was used. It was made

by Dow Carbowax Products, Inc. The tape cast films also had PEG as the binder, however the value of n and its manufacturer is unknown.

$$H\text{-}(OCH_2CH_2)_n\text{-}OH \tag{4.1}$$

IV.1.3 Films

Tape cast films were bought from NextTech Materials Inc. The tapes were made using TZ-8Y from Tosoh Corporation. The tapes were 3 feet by 6 inch roles backed by a Mylar film. Four 50 μm thick tape cast pieces were stacked together for the experiments. The desired sample geometry was achieved by stamping out the shape from the roll of tape cast material. The stamping was conducted using a commercial steel die.

IV.2 EXPERIMENTAL SETUP

IV.2.1 Sinter-Forger

A sinter-forger, or sometimes referred to as a loading dilatometer, was first introduced by De Jonghe and Rahaman [1]. A sinter-forger is a furnace that is capable of sintering a sample while simultaneously loading the sample with a uniaxial strain rate, or specified load. This sinter-forger is designed to measure the dimensions of the sample in two orthogonal directions while it is sintering. The schematic of the set-up is shown in Figure 4.1. The actual unit is a significant modification of the set-up designed and used by Dr. Sam Salamone for his dissertation and publications [2, 3].

The modified unit designed and built for this study is shown in Figure 4.2. It consists of a CM Rapid Temperature Box Furnace with holes cut in the sides and top. The holes cut into the sides are for access of laser beams used to measure the dimensions of the

sample as it is sintering. This enables non-contact measurement of the sample dimensions. Initially we experimented with sapphire windows on the side holes. However, the windows diffracted a significant fraction of the laser and the sensor was not able to measure the dimensions accurately. So, in the final design, the side holes were left open. The lasers used are ZYGO 1100 Series with Model 1101 Dimensioning Sensors. The data from the laser system is input into a computer and recorded using Labview. From the top of the furnace a two-inch outer diameter closed end alumina tube drops down into the furnace. The alumina tube has an oval hole cut out perpendicular through the tube for the lasers to pass through. Around the top of the alumina tube is a brass sleeve with threads that is attached to the alumina tube via Crystal Bond® (Aremco Products). The outer part of the brass sleeve with the threads is screwed into the aluminum frame that the furnace is attached to. This gives a fairly rigid frame to hold the two components together. Around the brass sleeve is a cooling jacket through which water passes through to cool the tube outside of the furnace, this also aids in protecting the other devices from the heat.

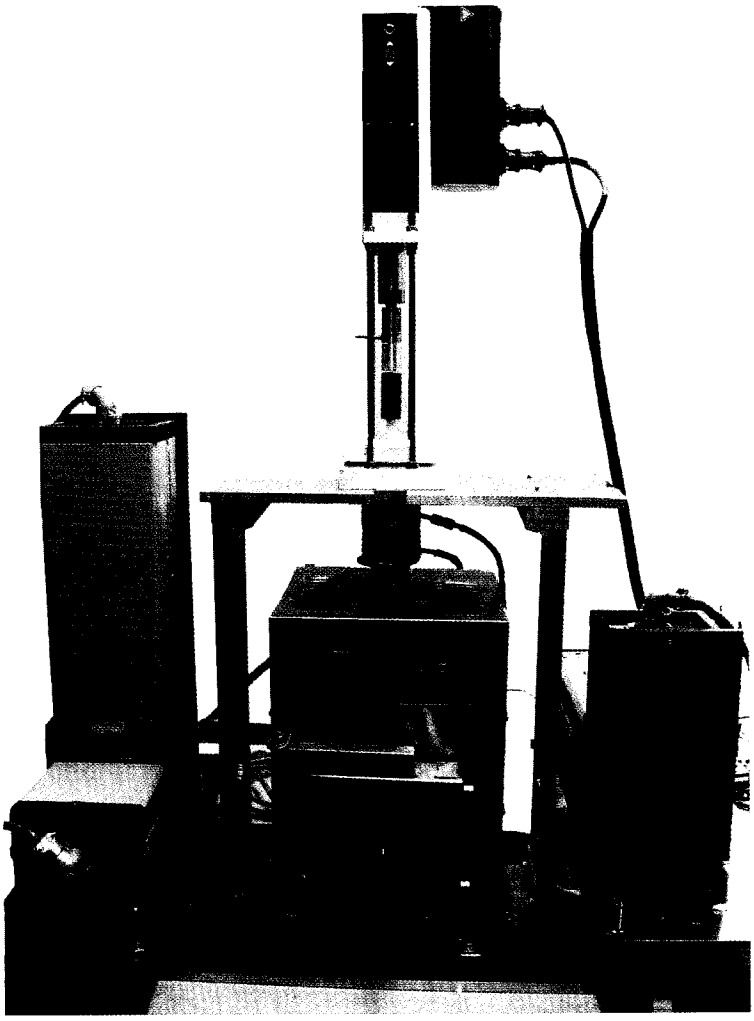

Figure 4.1 Sinter forger built for experiments.

In order to load the sample during sintering an Electric Cylinder model: EC3-B32-70-04A-100MF1-FT1E from International Devices Corporation is mounted on the aluminum frame. The Electric Cylinder is controlled via an International Devices Corporation B8961 controller with keypad. To apply the load to the sample while it is sintering a half-inch flat bottom alumina tube is attached in-line with the electric cylinder. Single crystal sapphire substrates are placed below and above the sample in

order to prevent chemical reaction between the sample and the alumina. To measure and record the applied load a load cell is placed between the alumina loading rod and the electric cylinder. The load cell is a 1000lb button cell from Entran model ELPM-T3E*-1KL-/Z4. The load cell is powered by an Entran PS-30-1 voltage source. To measure temperature of the furnace near the sample a B-type thermocouple is inserted into the furnace. The temperature is measured using a National Instruments SCB-68 DAQ board. All the data is received and recorded using Labview.

The system is designed to withstand 1000lb loads repeatedly up to 1450°C; the system has been tested successfully up to 1250 lbs without incident. A further experiment up to 1300 lbs ended with a fracture of the bottom of the closed end tube. The fracture initiated at a pre-existing crack that had formed from extensive use. The pre-existing crack had formed at the bottom of the oval cut perpendicular through the tube. The rest of the setup had no damage or fatigue from these high loads. The electric cylinder that applies the load via an alumina tube can be moved in 1μm increments, and up to 2cm per second. This electric cylinder allows for the precise control of speed or position of the actuating rod. Force control is also an option with the addition of an upgraded controller.

IV.2.2 Suggestions for the Further Improvements of the Sinter-Forger

The current design of the sinter-forger is a significant improvement over the version that was used in earlier studies. In particular the use of lasers to measure the dimensions and the electric cylinder to apply the load are two significant enhancements. In order to continue to improve the capabilities of the sinter-forger some additional work will need to be done. One limitation that the current setup has is the inability to permanently position the lasers in the desired location with respect to the sample. This is important to ensure repeatability. The system should be mounted on a thick metal plate or rigid frame where the lasers are rigidly and directly connected to the sample stage. The lasers

can then be used to accurately measure the flatness of the stage and the loading rod. In addition, the laser receivers, which are responsible for the actual sample measurements from the sample shadows, do have some limitations. The accuracy of the laser system does need to be improved in order to be competitive with the best sinter-forgers now in operation, such as the device built by Emil Aulbach at the Technical University in Darmstadt [4-6].

IV.3 EXPERIMENTAL PROCEDURES

IV.3.1 Processing of samples

IV.3.1.1 PREPARING TAPES FOR LOADING DILATOMETRY

The loading dilatometry experiments used tape cast YSZ to study the effect of a uniaxial load on the development of natural submicron pores in the microstructure. One-quarter inch circles were stamped out of the 50μm tape cast sheets from NextTech Materials Inc. Four of these circles were stacked and pressed together before being sintered. Four circles were used at a time instead of one, in order for a more accurate measurement of the sintering strain. These experiments were conducted in the sinter-forger.

IV.3.1.2 SLIP CASTING

For the pore analysis studies with controlled sized pores, all of the samples were prepared via slip casting. This was the second part of the study. The YSZ slurries were prepared in DI water with 20 volume percent solids using TZ-8Y powder from Tosoh Corp. Polystyrene spheres of varying sizes from Duke Scientific Inc. were introduced at 2-3 wt% of the solids used. The size of the spheres used was 0.2, 1.0, and 2.0μm. Polystyrene spheres were used to control the pore size because the polymer burns off

and leaves a controlled pore size at temperatures before any sintering can occur. This technique was used successfully to study the fracture toughness of alumina with controlled size pores [7, 8]. The slurries contained 3% Carbowax 3000 powder to increase the strength of the "green" compact. The slurries were mixed via a stir-bar on a stir plate, and homogenized in an Ultrasonic Homogenizer. The samples were slip cast on a flat gypsum mold wetted slightly before casting. A Teflon mold with 9mm holes was placed on the gypsum mold and the slurry was poured into the holes to cast the pellets. The molds were covered with Parafilm in order to slow the drying of the samples and prevent cracking. After drying the samples were sanded slightly in order to achieve more parallel faces.

In the experiment to study pore behavior transition with respect to particle size a smaller powder was used. This powder, the YSZ-8 from Fuel Cell Materials Inc., the processing procedure for making the slip cast samples was the same as for the TZ-8Y except for the following: The volume percent loading of the YSZ-8 in DI water was 10 percent solids, and the polystyrene spheres used for this experiment to create controlled sized pores were 0.5μm in diameter from Duke Scientific Inc.

IV.3.1.3 CENTRIFUGAL CASTING

For the third part of this dissertation, a Focused Ion Beam was used to introduce well defined flaws in the "green" ceramic films. The films were prepared by centrifugal casting. Centrifugal casting consists of three main parts: slurry/substrate preparation, casting the films, and removal/drying of the sample. This technique has been used elsewhere for YSZ, alumina, and other ceramics [9, 10].

In a 60ml centrifuge tube from KOKUSAN, 30 ml of Ethanol was added to a measured amount of YSZ. To the 60ml slurry, 4 drops of HNO3 was added to make the slurry acidic, which aids in increasing the inter-particle attraction of the slurry. Ten drops of

Ammonium Chloride was added to the slurry to coagulate the particles. The rheology of YSZ slurries has been studies extensively. The techniques I used were thoroughly discussed in literature [10-12]. The slurry was sonicated in a SMT UH-50 Ultrasonic Homogenizer for 20 minutes before the substrates were added. The slurry would be sonicated again briefly after the substrates were added to disperse the coagulated slurry once more.

Films of three thickness were made that are designated A, B, and C which corresponds to 10, 20, and 40 μm thick. To control the film thickness at 10/20/40 μm regardless of the beaker, the amount of YSZ powder in the beaker used with respect to the cross section of the beaker for the A sample was 17.69, B=8.84, C=4.42 milligram/cm^2.

Substrates of alumina, sapphire, and platinum coated sapphire were used in centrifugal casting. The 99.8% alumina substrates were 8mm diameter and 2mm thick and were bought from CoorsTek Inc. The single crystal sapphire substrates were 9mm in diameter and 3 mm thick and were received from Saint-Gobain Crystals. Half of the sapphire substrates were coated with platinum by DC sputtering. Professor Masumoto at Tohoku University in Sendai, Japan prepared the platinum coated sapphire substrates by DC sputtering. The alumina and sapphire substrates were sonicated in ethanol for 20 minutes in a sonic bath to clean them. The platinum coated substrates were sonicated at low power in ethanol with the SMT UH-50 for 5 minutes.

The substrates were placed carefully in the center of the flat bottom centrifuge tubes before being carefully lowered into the centrifuge. If necessary, extra substrates would be used to position the substrate perfectly in the center of the tube. Extra care was taken during these steps in order to prevent the film from being cast non-parallel to the substrate. The centrifuge was a Kokusan H-19FM. The samples were spun at 26K rpm for 30 minutes, or approximately 1800 times gravitational acceleration. After the centrifuge stopped the supernatant was pipetted off, with care not to disturb the cast

film. The sample was removed from the centrifuge tube and placed on an alumina block in a second beaker with a shallow ethanol "moat" around the alumina block. The beaker was covered with Parafilm and a few narrow holes were punctured into the Parafilm. The ethanol in the second beaker was used to prevent rapid drying of the sample and subsequent cracking of the film. The beaker was then placed in a sealable plastic Tupperware-like box for 24-48 hours.

IV.3.1.4 FOCUSED ION BEAM

The Focused Ion Beam (FIB) technique was developed in the late 70's and early 80's, with commercial FIBs introduced in the late 80's [13]. The ion beam is generated from a liquid metal ion source, usually Gallium. The effect of the ions on the surface of the subject material can lead to sputtering of neutral and ionized atoms (milling), electron emission (enables imaging, but may cause charging), displacing of atoms (damage), and emission of phonons (heating) [14]. The FIB technique can be used for many ultra fine milling geometries useful in fabricating integrated circuits [15], and optoelectronic devices [16]. The FIB technique can also be used for specimen preparation of TEM samples [17]. Some other creative uses of a FIB are creating surface markers to study local creep in lead-free solder [18], and for pre-cracking a coating to measure its fracture toughness [19].

In this study the FIB was used to introduce cracks and holes into the green centrifuge-cast YSZ films. The FIB used was a Hitachi FB2000A. To prepare a sample for milling in the FIB it first has to be mounted. A steel substrate is used to prevent any unnecessary handling of the fragile film-coated substrates. The steel substrates were first cleaned by sonicating in ethanol for 20 minutes. Carbon tape was placed on the 1 inch by 1 inch and 4 mm thick square steel substrates. The film-coated substrates were placed on the carbon tape. Silver paste was applied to the edge of the sample connecting

it to the steel substrate for a conduction path. The mounted sample would then be coated with gold-palladium in a JEOL sputterer for 200 seconds at 10mA.

Unwanted damage of a sample from the FIB beam has been discussed previously in literature [20]. The prepared sample would be inserted into the FIB and imaged with the lowest beam to prevent any unnecessary beam damage. For milling, the highest strength SEM-sample-stage beam was used to increase the milling rate. The milling would preferable be done at the center of the sample and far away from edges, damage, or silver paste. Some slight damage was done every time to the milling area from a single scan needed to map the milling area.

IV.3.2 Sintering

IV.3.2.1 SINTER-FORGER

For the experiments that needed to be done using the sinter-forger, such as the pore analysis experiments with the tape cast YSZ and the slip cast YSZ, the sintering procedure was the same. The samples all contain some Polyethylene Glycol binder so a binder burnout step in the sintering cycle is necessary. It is necessary to burn off all of the binder slowly so that the expansion of the gasses does not exert too much pressure on the sample and cause it to crack or explode. When using polystyrene spheres in the sample, it is also very important to burn off the polymer slowly. This is needed in order to maintain the structure of the artificial spherical pores.

To determine at which temperature the binder burns off, a Thermo Gravimetric Analyzer was used. It measures the weight of the sample as it heats up and measures any weight loss or gain. As can be seen in Figure 4.2, all of the binder is decomposed by 420°C. Thus, the binder burn-out step in the sintering cycle was a heating rate of 2°C/min from room temperature up to 420°C, then a one-hour isothermal hold at 420°C.

After the burnout step the heating rate was increased to 5°C/min up to 1000°C. At 1000°C the ramp rate was increased further to 15°C/min until the isothermal sintering temperature had been reached. The temperature at which the ramp rate was increased, 1000°C, was decided from dilatometry experiments shown in Figure 4.3. From the dilatometer curve in can be seen that the TZ-8Y sample starts to sinter at about 1000°C. The dilatometer used was a Netzsch Instruments, Inc. Dilatometer DIL 402C. A dilatometer is a furnace with an alumina rod that applies a very small load and measures the strain of the sample as it sinters.

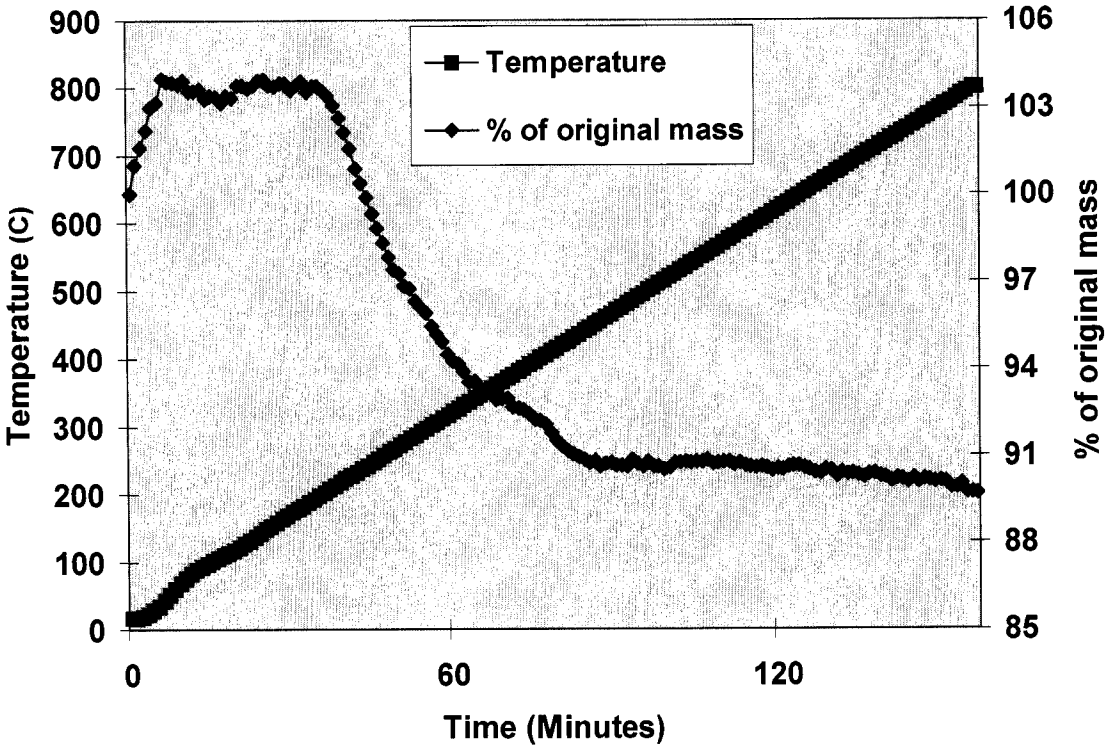

Figure 4.2 DSC analysis of YSZ powder w/9 wt% Polyethylene Glycol binder

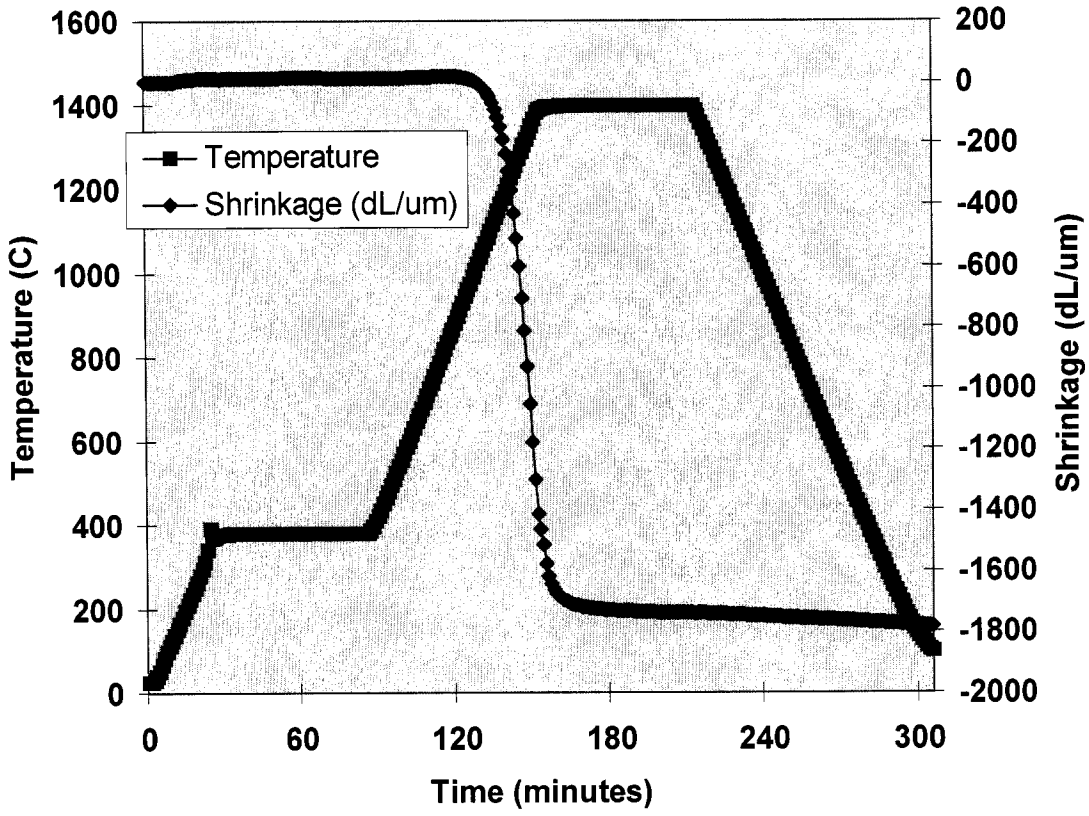

Figure 4.3 Dilatometry data of sintering YSZ

The ramp rate was increased before the sample started to sinter in order to reach the isothermal temperature quickly to prevent any unnecessary sintering before the isothermal temperature was reached. This was to ensure that the strain measurements are for as broad a density range as possible at isothermal temperature. All samples were held at the isothermal temperature for one hour, and were then cooled down to room temperature at 15°C/min.

The uniaxial load that was applied to the samples during sintering for the sinter-forging experiments was applied starting at room temperature, and continued as a constant load until the furnace had completed the sintering cycle and returned to room temperature. All experiments were conducted in air.

IV.3.2.2 FURNACE FOR CONSTRAINED SINTERING STUDIES

The constrained sintering studies were conducted in a FJ31 Yamato Scientific Co. high temperature box furnace at Tohoku University in Sendai, Japan. The heating rate for the samples was 2°C/min up to 1350°C. The slow heating rate was to prevent excess cracking in the films. The samples were held at 1350°C for one hour and then cooled down to room temperature at 2°C/min. The slow cooling rate was to minimize the formation of cracks due to thermal expansion mismatch. The FIB samples, which had been attached to a steel substrate before FIB and SEM work had been conducted, were removed from the steel substrate before being placed into the furnace for sintering. The experiments were conducted in air.

IV.3.3 Characterization

IV.3.3.1 SEM

Scanning Electron Microscopes were used to analyze the microstructure for all the samples. In the pore orientation study the SEM used was a JEOL 840A at the University of Washington. For the FIB study the SEMs that were used were a Hitachi 4700 and 4300 at Tohoku University.

The pore orientation study samples were polished before being imaged in the SEM. All samples were sliced using an ISOMET Low Speed Saw (Buehler Ltd) through their cross section. Samples were then set in Kwikset epoxy (Buehler), and polished using a

RotoPol-21 and a RotoForce-3 (Struers) down to 1um. Gold-Palladium was used to coat all samples for SEM use to make them conductive.

FIB samples were simply sputtered with gold-palladium before being imaged. After sintering, the samples were again sputtered with gold-palladium to image the crack growth.

IV.3.3.2 PORE ORIENTATION ANALYSIS

For the analysis of pore orientation, ImageJ software was used to analyze many pores simultaneously. ImageJ is free software developed by the Nation Institute of Health for analyzing images. This software has many features making it useful for this application. It was used to recognize the pores in a SEM image, and to analyze the size, shape, orientation of the long axis, circumference, long axis length, and short axis length. ImageJ was used to analyze between 300-500 pores at a time on each microstructure. This robust tool allowed a very precise analysis of the distribution of pore geometry, particularly the orientation, which was critical in this study.

Notes to Chapter IV

1. De Jonghe, L.C. and Rahaman, M.N., *Loading dilatometer.* Review of Scientific Instruments, 1984. 55(12): p. 2007-10.

2. Salamone, S., *Densification of and constitutive laws for ceramic matrix composites and multilayered systems* 2003, University of Washington. p. 214.

3. Salamone, S.M., Stearns, L.C., Bordia, R.K. and Harmer, M.P., *Effect of rigid inclusions on the densification and constitutive parameters of liquid-phase-sintered yba2cu3o6+x powder compacts.* Journal of the American Ceramic Society, 2003. 86(6): p. 883-892.

4. Zuo, R., Aulbach, E., Bordia, R.K. and Roedel, J., *Critical evaluation of hot forging experiments: Case study in alumina.* Journal of the American Ceramic Society, 2003. 86(7): p. 1099-1105.

5. Zuo, R., Aulbach, E. and Rodel, J., *Experimental determination of sintering stresses and sintering viscosities.* Acta Materialia, 2003. 51(15): p. 4563-4574.

6. Zuo, R., Aulbach, E. and Roedel, J., *Viscous poisson's coefficient determined by discontinuous hot forging.* Journal of Materials Research, 2003. 18(9): p. 2170-2176.

7. Flinn, B.D., Bordia, R.K., Zimmermann, A. and Rodel, J., *Evolution of defect size and strength of porous alumina during sintering.* Journal of the European Ceramic Society, 2000. 20(14-15): p. 2561-2568.

8. Zimmermann, A., Hoffman, M., Flinn, B.D., Bordia, R.K., Chuang, T.-J., Fuller, E.R., Jr. and Roedel, J., *Fracture of alumina with controlled pores.* Journal of the American Ceramic Society, 1998. 81(9): p. 2449-2457.

9. Chang, J.C., Velamakanni, B.V., Lange, F.F. and Pearson, D.S., *Centrifugal consolidation of alumina and alumina/zirconia composite slurries vs. Interparticle potentials: Particle packing and mass segregation.* Journal of the American Ceramic Society, 1991. 74(9): p. 2201-4.

10. Liu, J. and Barnett, S.A., *Thin yttrium-stabilized zirconia electrolyte solid oxide fuel cells by centrifugal casting.* Journal of the American Ceramic Society, 2002. 85(12): p. 3096-3098.

11. Nagaishi, M., Takeuchi, K., Fukunaga, A. and Egashira, M., *Preparation of yttria-stabilized zirconia thin films by sedimentation from liquid suspension.* Key Engineering Materials, 1999. 159-160: p. 163-168.

12. Zhang, Y., Gao, J., Peng, D., Meng, G. and Liu, X., *Dip-coating thin yttria-stabilized zirconia films for solid oxide fuel cell applications.* Ceramics International, 2004. 30(6): p. 1049-1053.

13. Melngailis, J., *Focused ion beam technology and applications.* Journal of Vacuum Science & Technology, B: Microelectronics and Nanometer Structures, 1987. 5(2): p. 469-95.

14. Reyntjens, S. and Puers, R., *A review of focused ion beam applications in microsystem technology.* Journal of Micromechanics and Microengineering, 2001. 11(4): p. 287-300.

15. Abramo, M.T. and Hahn, L.L., *Application of advanced techniques for complex focused-ion-beam device modification.* Microelectronics and Reliability, 1996. 36(11-12): p. 1775-1778.

16. Orth, A., Reithmaier, J.P., Mueller, J., Kieslich, A., Forchel, A., Weber, J., Gyuro, I. and Zielinski, E., *Gain-modulated second order distributed feedback gratings fabricated by maskless focused ion beam implantation in gainasp heterostructures.* Microelectronic Engineering, 1995. 27(1-4): p. 343-346.

17. Tsuji, S., Tsujimoto, K. and Iwama, H., *Application of cross-sectional transmission electron microscopy to thin-film-transistor failure analysis.* IBM Journal of Research and Development, 1998. 42(3-4): p. 509-516.

18. Jud, P.P., Grossmann, G., Sennhauser, U. and Uggowitzer, P.J., *Local creep in snag3.8cu0.7 lead-free solder.* Journal of Electronic Materials, 2005. 34(9): p. 1206-1214.

19. Di Maio, D. and Roberts, S.G., *Measuring fracture toughness of coatings using focused-ion-beam-machined microbeams.* Journal of Materials Research, 2005. 20(2): p. 299-302.

20. Rubanov, S. and Munroe, P.R., *Damage in iii-v compounds during focused ion beam milling.* Microscopy and Microanalysis, 2005. 11(5): p. 446-455.

CHAPTER V

RESULTS AND DISCUSSION: DEVELOPMENT OF ANISOTROPY IN INTRINSIC & EXTRINSIC PORES

V.1 INTRODUCTION

During the sintering of a constrained ceramic film, atoms are required to diffuse further in order to densify because of the inability of the particles or grain centers to move in the planar direction (or reduced movement from partial constraint). As shown schematically in Figure 5.1 the diffusion distance required for the growth of grain boundary A is shorter than the diffusion distance required for the growth of grain boundary B. In order for the grain boundary A to grow the atoms only need to diffuse across the grain boundary, but in order to grow the grain boundary B, the atoms are going to need to diffuse from grain boundary A across the pore surface to grain boundary B. As a result of the difference in diffusion distances, the pores in a constrained film are expected to become anisotropic as densification proceeds.

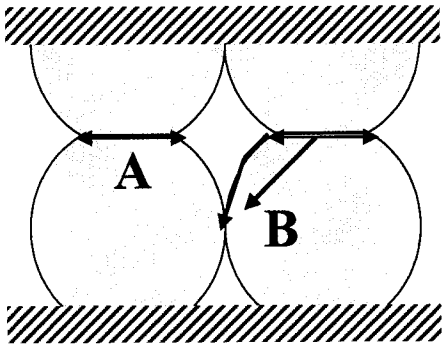

Figure 5.1 Constrained grains in sintering ceramic layer

The constraint of a rigid substrate can prevent the film from sintering because the tensile stresses generated reduce the driving force of sintering [1]. It has been shown in previous experiments with alumina and dielectric tape that this constraint leads to the reduction of the volumetric densification rate of the material [2].

There are two main competing forces that affect the shape of pores in stressed samples; diffusion control and strain control. Diffusion controlled shape development means that the diffusion of atoms to the areas of highest surface energy is the major force determining the development of the cavity. Strain controlled development means that strain around the cavity causes creep to occur which will be the determining force in cavity shape development.

These two forces are competing because they are both acting on the cavity at all times. The smaller a cavity is, the smaller the strain effect will be and more significant the diffusion effect will be. The larger the cavity is, the larger the strain effect will be, and the less significant the effect of the diffusional growth will be on cavity shape evolution. We predict that this is due to competing effects; there will be a critical size in the ceramics sintered under a constraint or sintered under external stress. One of the goals of the research is to determine the critical size in relation to the grain/particle size. A related goal is to determine the differences in the development of the shape of pores that are smaller and larger than the critical size.

V.2 CONSTRAINED/UNIAXIAL LOADING ANALOGY

In order to study the densification and microstructural evolution of a constrained layer we need a system that allows us to study this effect in a controlled manner. The constraint/uniaxial loading analogy provides one means to analyze this system. By uniaxially loading a sample we can mimic the microstructure that a constrained sample

would have. The microstructure that a fully constrained sample has is equivalent to the microstructure that a uniaxially loaded sample of the same density has if the load is applied in a manner that maintains a constant diameter. Looking at Figure 5.2, tension in the planar direction or compression in the z direction has the same effect on the samples microstructure (at the same density). For a sample that is being partially constrained, the diameter can be allowed to shrink to some extent in order to mimic the microstructure of a partially constrained film. And to mimic a fully constrained film, we can control the radial strain rate of the sinter forged sample so there is zero radial strain. Fundamentally, the analogy is based on the assumption that the pore evolution is governed by the strain state and not the stress state. This assumption is intuitively apparent although there is no experimental confirmation of this. In this study, this assumption will be accepted as valid. It can be seen from Figure 5.2 that if the starting density is the same, then the strain state at a given density is the same for the constrained film and the sinter forged sample. Experimentally, it is significantly easier to have a uniformly sinter-forged sample than a uniformly constrained film. As a result, sinter-forging will be used in this study to investigate anisotropic pore evolution.

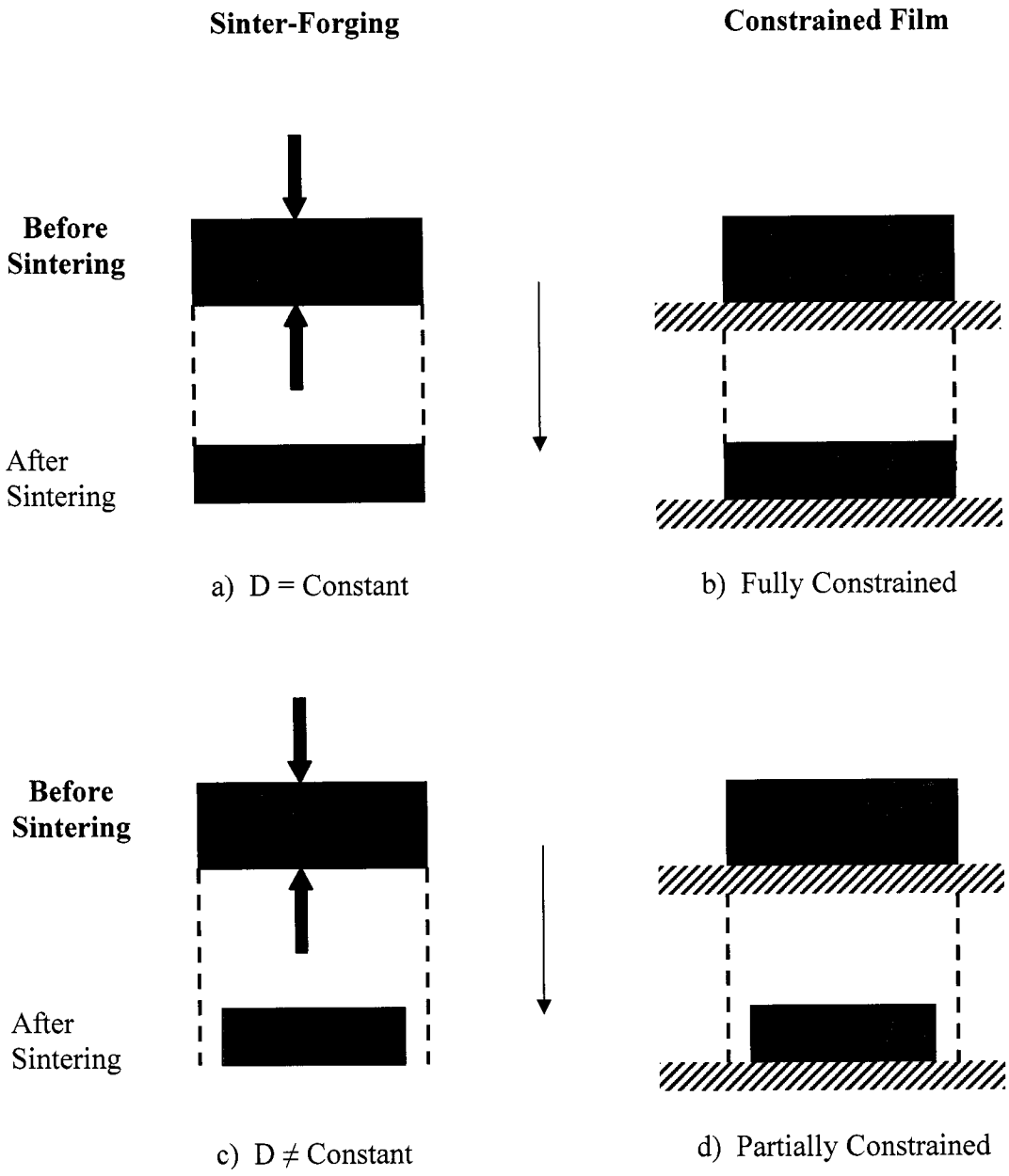

Figure 5.2 Uniaxially loading/constraint analogy. Before and after sintering for constant and changing diameter.

V.3 SINTER FORGED TAPE CAST YSZ

The experiments in this project are designed to study the development of anisotropic microstructures in sinter forged samples. In this section we have focused on the following.

The first objective is to show that the densification of a uniaxially loaded YSZ sample is modified from an unloaded sample. We need to determine if the uniaxial load is modifying the densification, which we are predicting will lead to anisotropic microstructure. This will be accomplished by sintering tape cast YSZ films with and without a uniaxial load. The uniaxial load will be applied using the sinter-forger that was described in Section IV.2.1. The sinter-forger will measure strain of the sample while it sinters so we can study the effect of the uniaxial load on densification.

To increase the understanding of the development of the predicted anisotropic microstructure, some parameters will be controlled. The temperature at which the loaded sample is sintered will be varied in order to determine its effect on the evolution of the pore shape. From an application point of view, this is very useful to know, in order to be able to control the microstructure. In addition, by varying the level of the uniaxial load on the sample, the degree to which loading the sample will affect the anisotropy of the pores will be determined. From the start point of the analogy described in the previous section, the load level in sinter-forging is related to the extent of the constraint in the constrained film. A higher load level corresponds to a higher degree of constraint.

In order to analyze the anisotropy of the sinter-forged samples, the microstructure will be analyzed using Image J. The microstructure analysis will include plotting the orientation of the pores with respect to the load axis in order to determine trends with respect to the applied load and the processing temperature. Further analysis will include

a quantitative analysis of the average pore orientation in the sample. This should provide a quantitative assessment of the effect of the variables on anisotropic microstructural evolution.

V.3.1 Densification

The first step in this study is to show that varying the applied uniaxial load will modify the densification of the Yttria Stabilized Zirconia system. This is important since a constraint is known to affect densification [2], and in order to maintain the analogy between sinter-forging and constraint the uniaxial stress during sinter-forging must alter densification.

In this experiment the tapes were sintered with and without loads at multiple temperatures. The measured strains were converted into relative density using final and green state densities.

Densification results for the set of samples sintered at 1400°C are shown in Figure 5.3. Samples with a uniaxial pressure of 0.0, 0.3, and 1.0MPa are shown. The results show that the greater the load during isothermal sintering, the greater the densification. The densification curves for the 1200°C and 1300°C samples followed the same pattern, but because of the lesser degree to which the samples densified at the lower temperatures the results were not as pronounced as those for the 1400°C samples.

Despite the increase in the heating rate after 1000°C to prevent excessive pre-isothermal densification, there was still variation in the amount of densification for the 1400°C sample before reaching the isothermal hold. Note that for these experiments, a fast heating rate of 15°C/min was used between 1000°C and 1400°C. Since the samples were under loading during the heat up, there are differences in the density at the start of the isothermal hold.

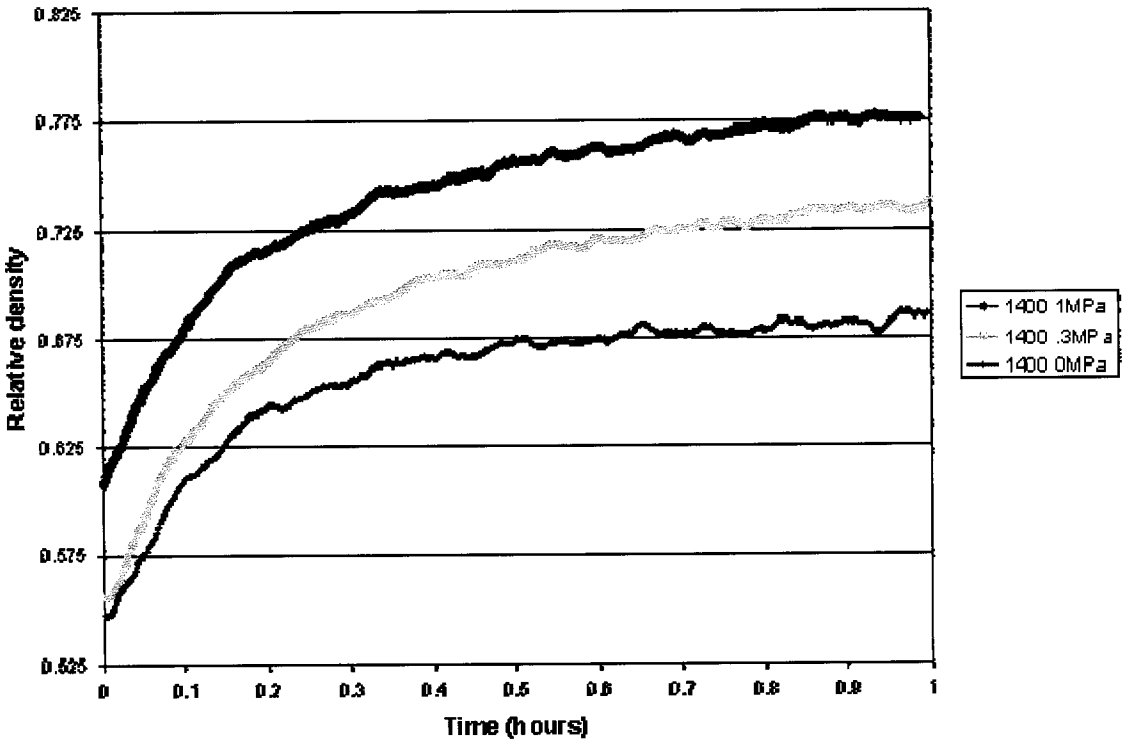

Figure 5.3 Densification data of uniaxially loaded YSZ tape cast layers at 1400℃

The densification curves for the tape cast YSZ in Figure 5.3 clearly show that as the uniaxial load increases the density of the sintered film increases. The compressive forces increase the densification of the samples. The samples also have a higher density as the load is increased before the isothermal is reached, most significantly shown in the 1.0MPa sample. The load on the sample was applied when the sample was at room temperature.

V.3.2 Definition of Intrinsic and Extrinsic Pores

In the samples analyzed in this dissertation there are two types of pores; intrinsic and extrinsic. Intrinsic pores are pores that are created during green processing. They lay within the natural compact of the particles. For this reason they are within an order of the size of the mean powder diameter and smaller. Extrinsic pores are pores that are created during green processing or during the heating cycle. Their source can be from expanding gasses, the cavity left behind from burnt foreign bodies, and cavities created from agglomerated powder. Their size is an order above the mean particle diameter and above. It is important to reiterate that extrinsic pores are larger than the intrinsic pores that are being studied and the behavior of the two is significantly different.

V.3.3 Evolution of Intrinsic Pore Anisotropy in Tape Cast Films

The second focus of this part of the study is to analyze the pore structure to see if the pores did develop anisotropically as was anticipated. In order to get a better understanding of the pore orientation distribution, the pore angles were plotted in polar plots. For this study, the angle is the measured angle between the X-axis and the long axis of the pore and the magnitude is the number of pores that have that angle (as shown in Figure 5.4). Image J was used as described earlier to measure the pore orientations. The pore orientations collected from image J measure the pores' orientation from 0 to 180°. In order to complete the polar plots the complimentary angles (180-360°) were created by adding 180° to the collected data. Note, in the polar plots there is equivalence between angle θ and $180 - \theta$ as shown schematically in Figure 5.4.

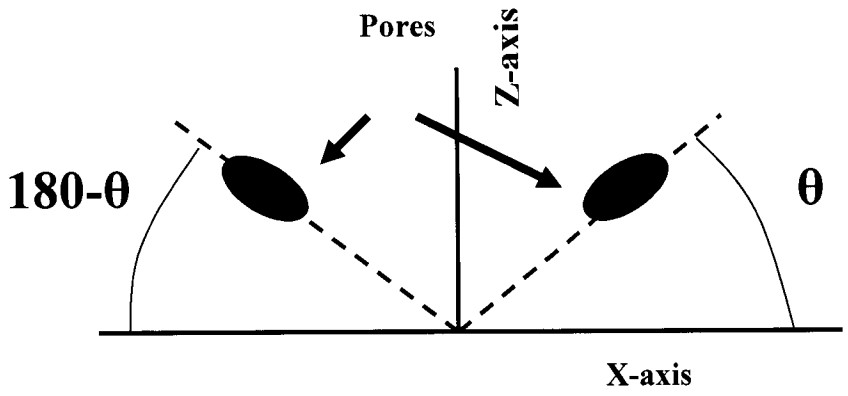

Figure 5.4 Schematic of measured pore angles and complimentary pore angles.

The microstructures of the samples analyzed are shown in Figure 5.5. As can be seen, the density of the samples increases for both increasing temperature and increasing load. This is consistent with the densification calculated from strain measurements.

The polar plots for all samples are shown in Figure 5.6. The 0.0MPa samples all have a very similar pore distribution regardless of sintering temperature. The 0.0MPa 1200°C sample does look a little different than the 1300°C and 1400°C samples, but due to the equivalence shown in Figure 5.4, these pore orientations are similar. The 0.3MPa samples start to show a more significant orientation adjustment towards the uniaxial load. The 1.0MPa samples show significantly more pore orientation towards the uniaxial load with the 1400°C sample being the most anisotropic.

From these plots it can be clearly seen that the applied stress is inducing anisotropy in the samples. The larger the load that is applied to the sample the higher the anisotropy in the sample. This supports the hypothesis that anisotropy is induced in all constrained samples, with larger constraint leading to a higher level of anisotropy.

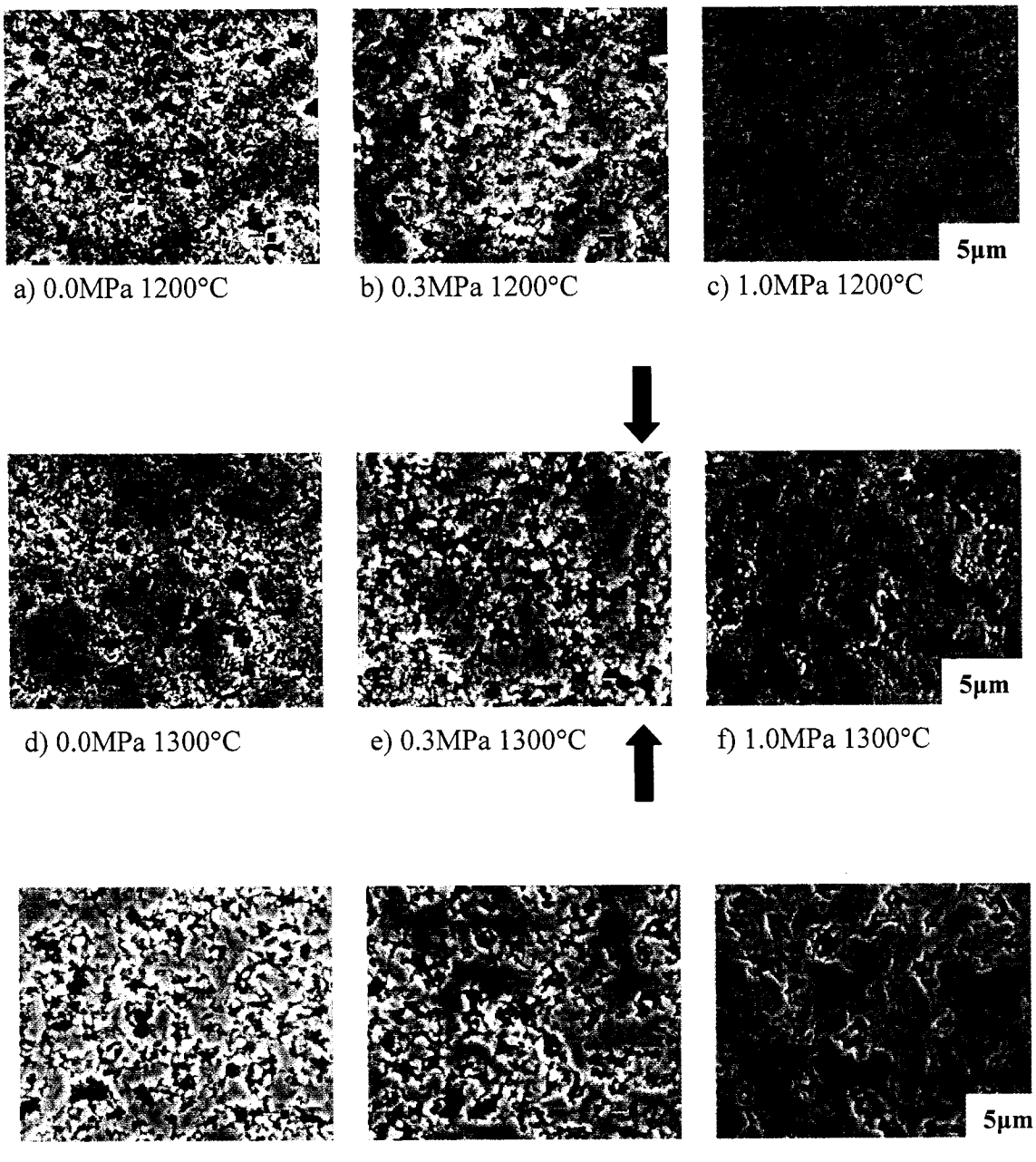

a) 0.0MPa 1200°C b) 0.3MPa 1200°C c) 1.0MPa 1200°C

d) 0.0MPa 1300°C e) 0.3MPa 1300°C f) 1.0MPa 1300°C

g) 0.0MPa 1400°C h) 0.3MPa 1400°C i) 1.0MPa 1400°C

Figure 5.5 Sinter forged tape cast YSZ samples

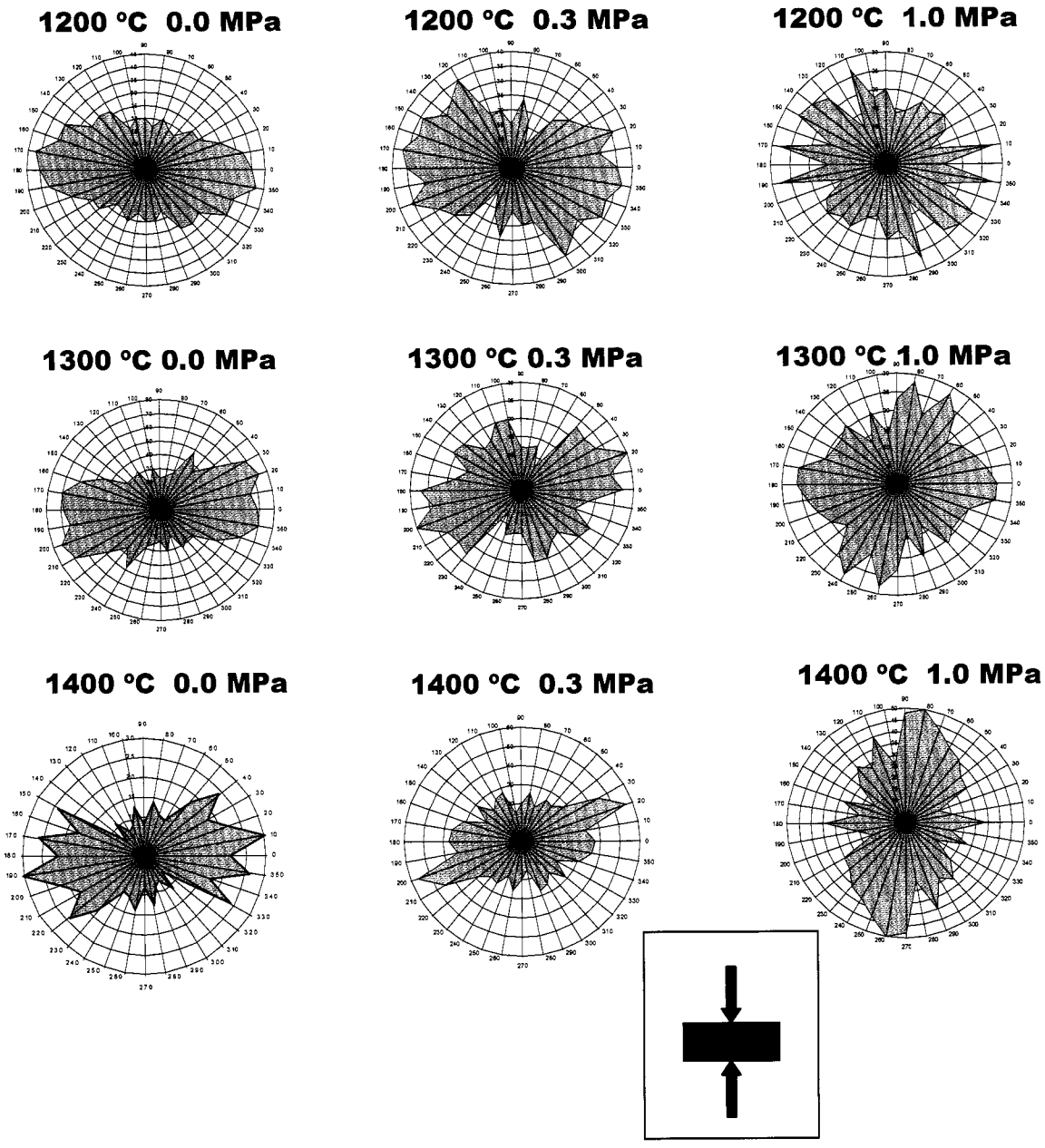

Figure 5.6 Polar plots of pore orientation for all samples.

V.3.4 Comparison of Pore Anisotropy in Loaded Tape Cast Films

The polar plots are effective in visually displaying the development of anisotropic pore structure due to load. In order to more accurately compare the orientation of the pores, the average pore angle for all the samples was determined. Since the angles were measured from 0-180°, the angles from 91-180° were mirrored across the Z-axis. Because we are only interested in the reorientation towards the Z-axis the samples with orientations from 90-180° are equivalent to samples with angles from 90-0°. During Image J analysis all cavities that were too small (20 pixels or less, below .005 μm^2, mainly from random dark spots on the micrograph) or cavities that were too big (above 9 μm^2, from voids in the material or grain pullout) were excluded. Results of the average pore orientation are shown in Figure 5.7.

In the unloaded sample (0.0MPa), we expected to see an average pore angle of 45°. In an isotropic material the pore angles should be evenly distributed between 0° and 90° with an average of 45°. In all three samples, the material seems to exhibit an anisotropic behavior while being freely sintered. This anisotropic behavior in the freely sintered sample must be attributed to the green state processing. It should be noted that the samples were tape cast and tape casting is known to induce a preferred texture.

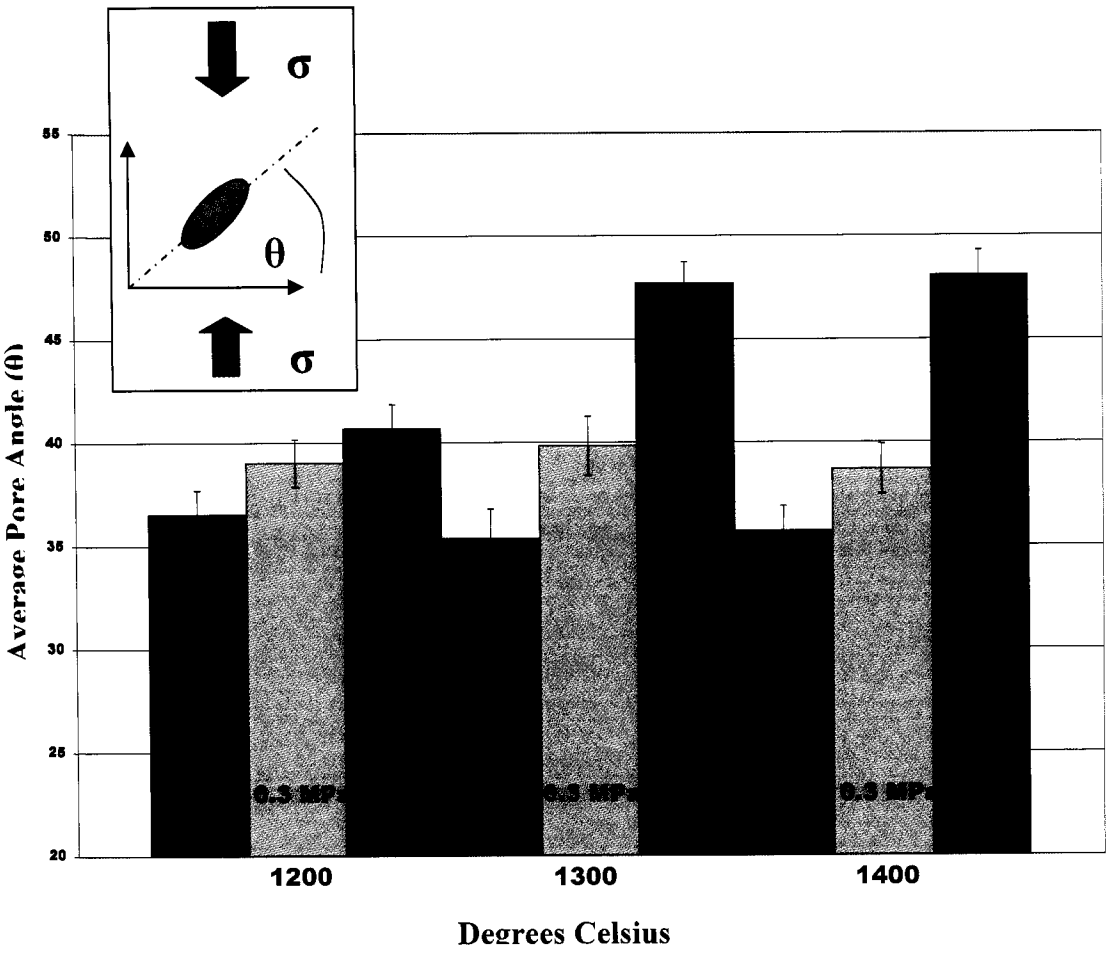

Figure 5.7 The average pore angle of loaded films

The uniaxial pressure of 0.3MPa appears to be sufficient to orient the pores parallel to the direction of the load. Applied load appears to have a more significant effect on pore orientation as compared to differences in the temperature for the 0.3MPa samples.

An applied stress of 1.0MPa had a significant effect on the pore orientation. For this high load, the difference between 1200°C and 1300°C sinter-forged samples is significant but the difference between 1300°C and 1400°C is insignificant. A full theoretical analysis of these effects is beyond the scope of this dissertation. However,

this dissertation has provided clear experimental analysis of the effect of stress and temperature on the development of anisotropy in pore orientation.

Fully constrained samples are going to experience a larger stress in the planar direction than a partially constrained sample, like in a co-fired situation. With the constraint/uniaxial loading analogy, these results show that varying degrees of constraint will affect the anisotropy of pores. It can be postulated that varying degrees of constraint will also affect the extent of anisotropy in the rest of the microstructure (e.g. grain size).

V.3.5 Discussion of Pore Anisotropy in Loaded Tape Cast Films

A constrained layer requires that atoms diffuse further in order to densify because of the inability of the particle/grain centers to move in the planar direction due to the planar constraint (or reduced movement from partial constraint). In this study, the analogy between sinter-forging and constrained sintering has been used and it is shown that microstructure (in particular pore orientation) becomes anisotropic. This, it is anticipated that in addition to modifying the densification behavior, the constraint will induce anisotropy in the microstructure.

Figure 5.8 schematically illustrates that the constraint increases the diffusion distance required for the growth of grain boundary B. The diffusion distance to grow grain boundary B is longer than the diffusion distance required for the growth of grain boundary A. This disparity in grain boundary growth rate causes the orientation of the pores to develop in the direction perpendicular to the constraint (Z-direction). In terms of the analogy between constrained sintering and sinter forging, the compressive stresses are applied along this direction in sinter-forging. Thus, the pores are expected to become anisotropic and orient their long axis along the direction of the compressive stresses. The extent of re-orientation and the magnitude of the anisotropy are expected

to increase as the compressive stress increases since this is the driving force for the induced anisotropy.

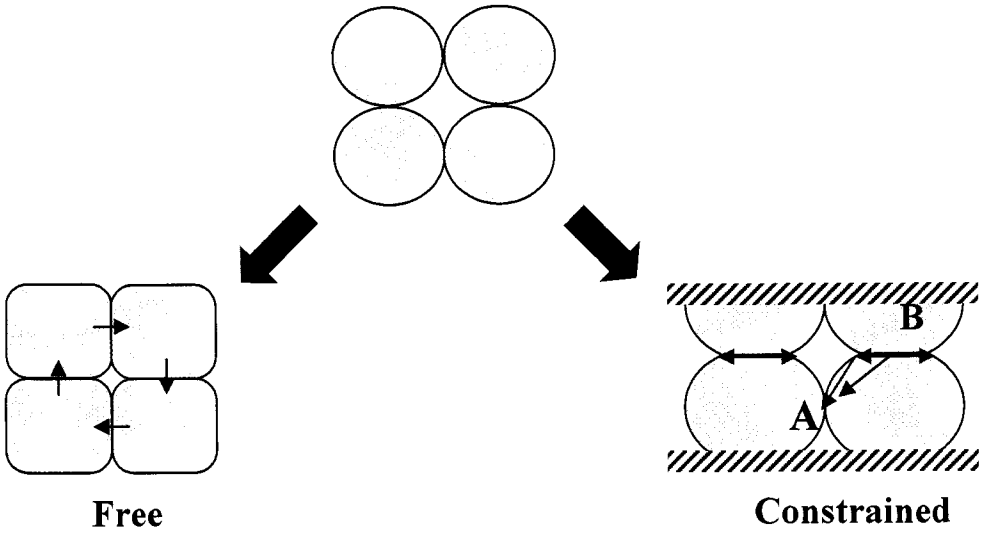

Figure 5.8 Pore development in a free and constrained system.

This phenomenon only occurs for pores between particles (of the order of particle sizes). For larger voids in the material, the orientation development is going to be reversed [3]. There is a critical pore size where the effect of strain becomes larger than the effect of diffusion in controlling the texture in pore orientation. Cavities larger than the critical size will orient perpendicular to the applied compressive stress.

V.4 SINTER-FORGED SLIP CAST YSZ WITH CONTROLLED PORES

As discussed earlier, the intrinsic pores re-orient in the parallel direction of the applied load during sinter-forging. It is expected that extrinsic pores greater than critical size in a sinter forged sample will orient themselves perpendicular to the applied load. An

important question, both fundamentally and from an application point of view is; what is the critical size and does it scale with the microstructure?

In this part of the study, controlled sized polystyrene spheres were introduced in the YSZ slurry so controlled sized pores could be studied in the sinter-forged compact. The volume fraction of the pores was between 2-5%. The samples were sinter-forged at 1.0MPa with spheres of 2.0, 1.0, and 0.2μm. The isothermal sinter-forging temperature was 1400˚C. These samples were processed by slip casting, and have a higher starting green density and increased homogenous particle packing than the tape cast materials used in the previous study. These sized pores were used based on a prediction that the transition point would be somewhere between half the size of the particle and four times the average particle diameter. The average particle size of this YSZ is 0.5μm.

V.4.1 Intrinsic Pore to Extrinsic Pore Transition in Slip Cast YSZ

This proposed experiment is to determine if there is a difference between large and small pores with respect to the evolution of anisotropy. There are multiple ways to investigate this transition. One method is to sinter-forge samples to moderate densities (80-90%) at which one could analyze the pores in Image J. This method would allow a large sampling of pores and evaluation of anisotropy. With this method it should be possible to determine a pattern that pores follow in a loaded sample based on their size. This method was tried, but the amount of control over the pore sizes was very difficult. As a result, specific conclusions regarding the critical pore size could not be drawn. Most likely this is due to the rather narrow size of the pores in the sample studied here.

The method that will be used in this study is to add polystyrene spheres of extremely narrow size distribution to the ceramic powder before sample processing. Polystyrene spheres can be bought in suspension form and of well controlled size. The sphere suspension allows easy integration into the ceramic slurry. During heating to the

sintering temperature the beads would burn off and leave controlled size pores in the compact. The samples with the controlled sized pores could then be sinter-forged, and the microstructural evolution of the pores could be studied in a more accurate and more controlled manner. Different sized spheres were used to study their evolution during sintering. The pore anisotropy will be evaluated with ImageJ. The pore transition point will be the point at which the pores are isotropic even after being sinter forged. The weight percent of the polystyrene spheres was about three percent. All samples were sintered or sinter-forged at 1350°C.

The 2.0μm diameter pores were studied first. As shown in Figure 5.9, it can be seen that this method is successful in creating consistent controlled sized pores in the microstructure that are easily identified. This micrograph is from a freely sintered sample. In Figure 5.10 a sinter forged sample loaded to 1.0MPa are shown. It can be seen that the pores orient themselves perpendicular to the uniaxial load, contrary to the intrinsic pores studied earlier in this project. This verifies that extrinsic pores do behave differently than intrinsic pores, and that there must be a critical pore size at which the transition occurs.

The samples with 0.2μm diameter pores were subsequently studied. These pores are on the order of the size of the natural pores studied in the sinter-forged films discussed earlier. This experiment was to determine if more uniformly shaped pores of the same approximate size would behave the same as the natural pores, and also verifies the accuracy of the earlier results. As can be seen in Figure 5.11, the unloaded samples have an even distribution of pore orientations, not unlike that of the unloaded samples with the larger pores (Figure 5.9). The 1 MPa sinter-forged sample with 0.2μm controlled pores is shown in Figure 5.12 clearly shows the pores have preferentially oriented themselves, parallel to the uniaxial load. This behavior is consistent with the natural pores studied in the sinter forged tape cast YSZ samples. It is interesting to note that the shape of the pores is not as accurately controlled as the pores in the 2.0μm. Presumably

this is due to the fact that the pores are now smaller than the size of the particles. They are of the same order as pores between particles and link with them.

The freely sintered sample with 1.0μm pores is shown in Figure 5.13. It again shows the ability to create a controlled sized microstructure. The sinter forged sample (1MPa) in Figure 5.14 lacks the anisotropic behavior shown in the other two samples. ImageJ analysis showed that the average pore aspect ratio is approximately equal to that of the control sample with no load. This leads to the conclusion that for a 1.0MPa loaded sample with an average particle size of 0.5μm transition pore size is of the order of 1.0μm.

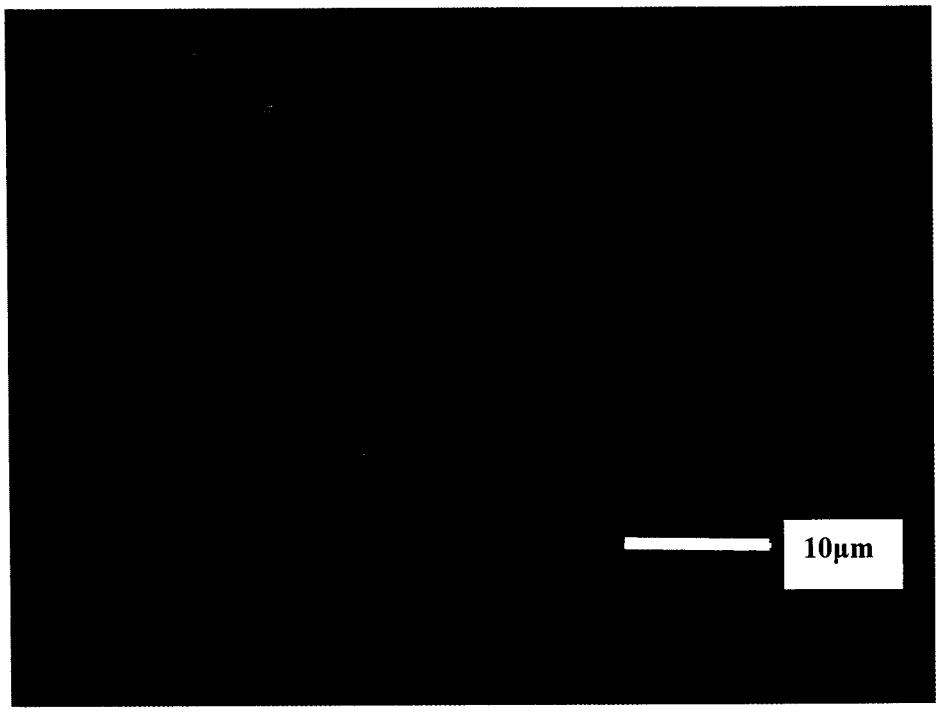

Figure 5.9 Sintered YSZ compact with 2.0μm polystyrene spheres. Sintered at 1350°C.

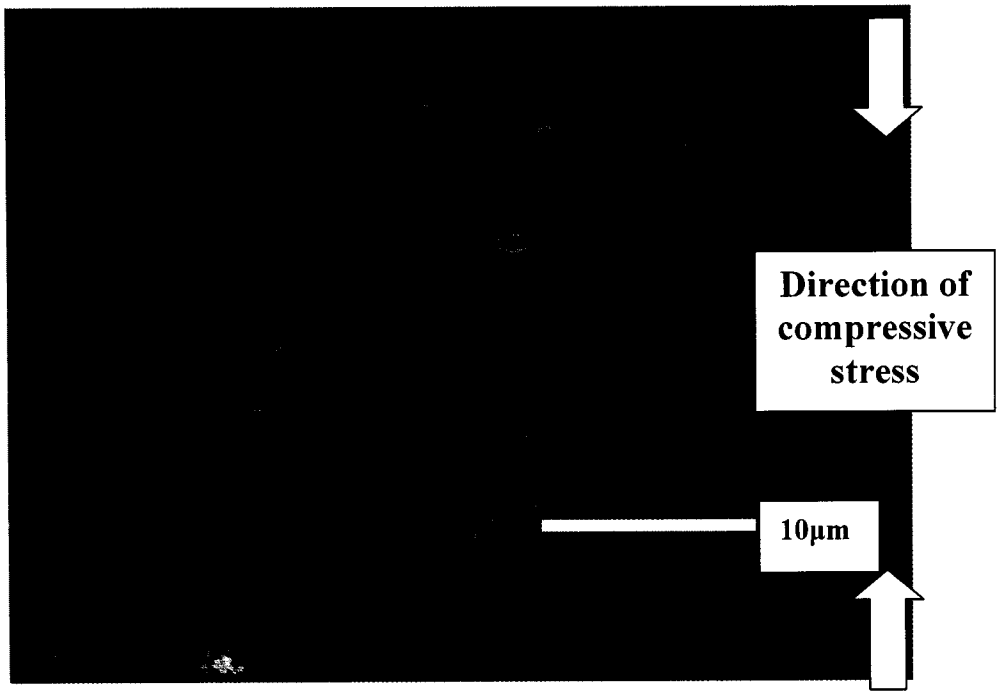

Figure 5.10 Sinter forged YSZ compact with 2.0μm polystyrene spheres at 1350°C and at a nominal stress of 1MPa.

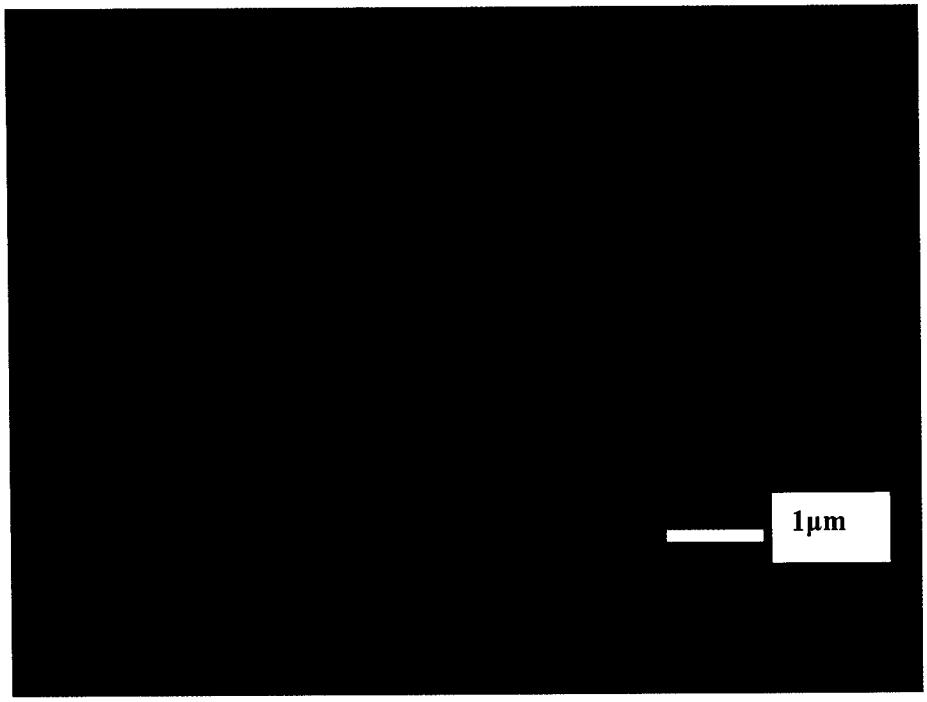

Figure 5.11 Sintered YSZ compact with 0.2µm polystyrene spheres. Sintered at 1350°C.

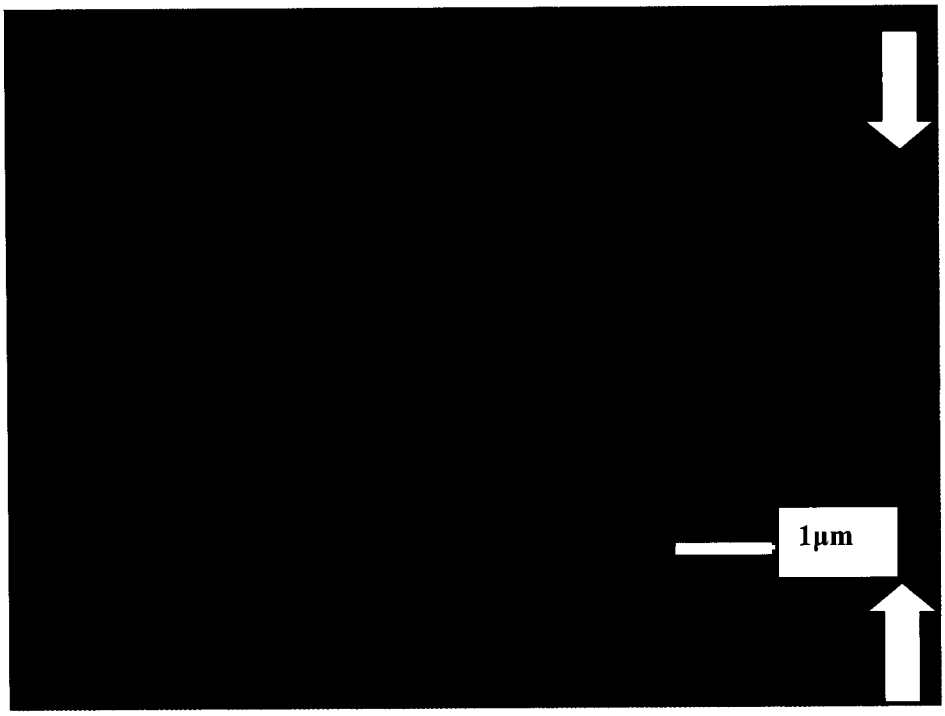

Figure 5.12 Sinter forged YSZ compact with 0.2µm polystyrene spheres at 1350°C and nominal stress of 1MPa.

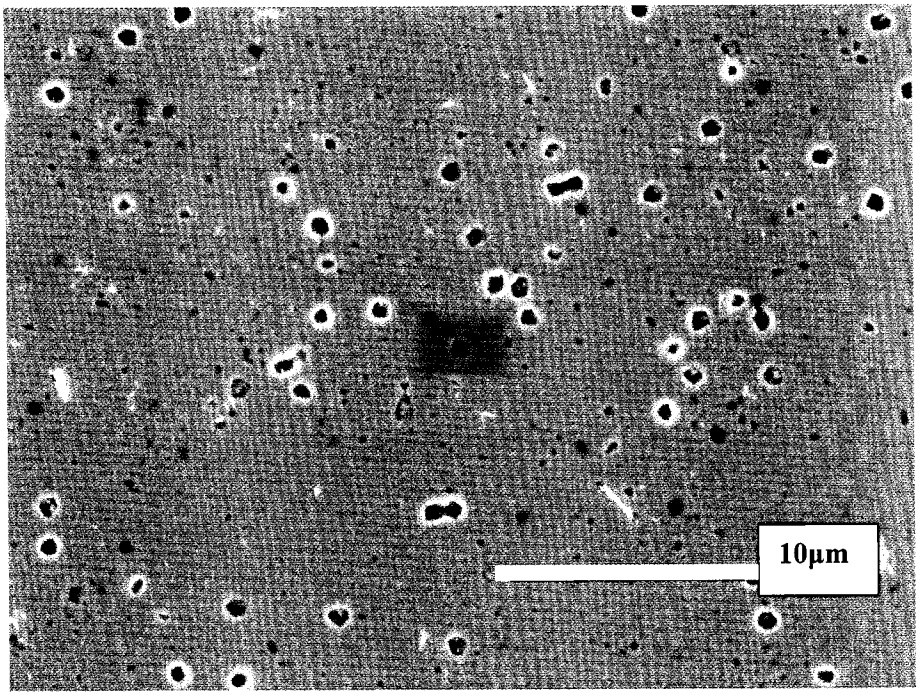

Figure 5.13 Sintered YSZ compact with 1.0µm polystyrene spheres. Sintered at 1350°C.

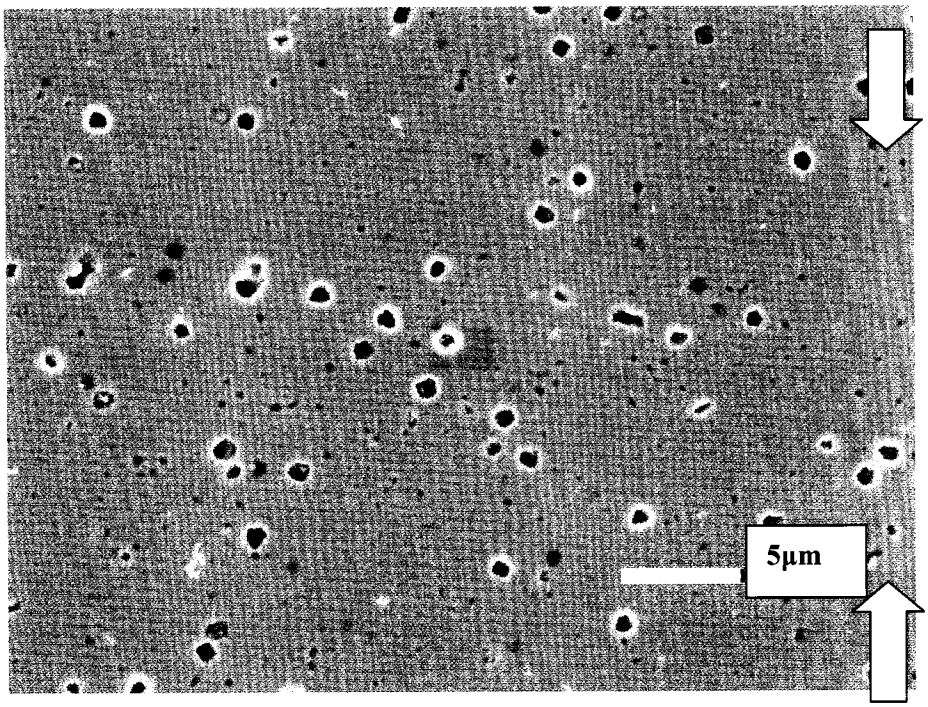

Figure 5.14 Sinter forged YSZ compact with 1.0µm polystyrene sphere sat 1350°C and a nominal stress of 1MPa.

The results for the intrinsic to extrinsic pore transition thus far have not been analyzed with respect to load or particle size. In order to increase our understanding of this transition point another experiment was conducted to determine the affect of load and particle size on the transition point. A YSZ powder with mean particle size of 0.25μm was used to see if the transition point scales with particle size. The polystyrene spheres used for this experiment were 0.5μm in diameter, twice the particle size. The particle size to sphere size ratio is the same as the previous transition study. The samples were sintered with the same heating profile and sintering temperature as the previous study. The samples in this study were sinter-forged at nominal stresses of 0.0, 0.5 and 1.0MPa to determine if the transition point is a function of load. The sinter-forging was conducted at 1350°C.

Figure 5.15 shows a cross-section of a sinter-forged YSZ sample made with the 0.25μm powder and a three percent weight percent of 0.5μm polystyrene spheres. This sample was sinter-forged at 1MPa. The samples were analyzed using ImageJ to measure the average pore orientation angle for each load. The results are shown in Figure 5.16. As can be seen in the graph, as the load increases, the pores became more anisotropic and their long axis orients preferentially, parallel to the uniaxial load. This behavior is representative of intrinsic pores.

There are two significant observations from this experiment. The first one is that the individual anisotropy in pore orientation is load dependent. For 1MPa, the average pore orientation changes from approximately 46° to approximately 53°. The significance of this will be discussed later. The second important observation is that the transition from intrinsic to extrinsic pore behavior does not occur at a fixed ratio of pore size to particle size. In the results presented earlier in this Section (on 0.5μm YSZ powders), the transition occurred at a pore size to particle size of 2. In the results presented in this

experiment, the same pore size to particle size ratio was studied but the pores behave like intrinsic pores. Further research is needed to study the particle size dependence of the transition from intrinsic to extrinsic pore response.

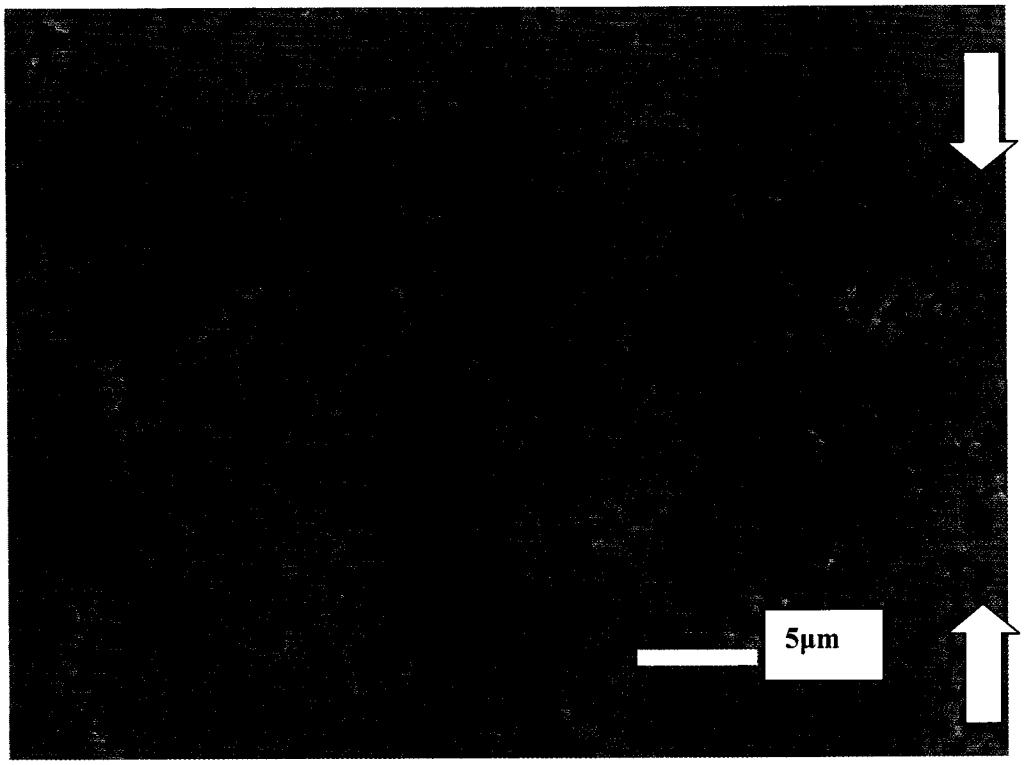

Figure 5.15 Sinter forged 0.25μm YSZ powder with 0.5μm introduced pores. Sinter forging was conducted at 1350°C and a nominal stress of 1MPa.

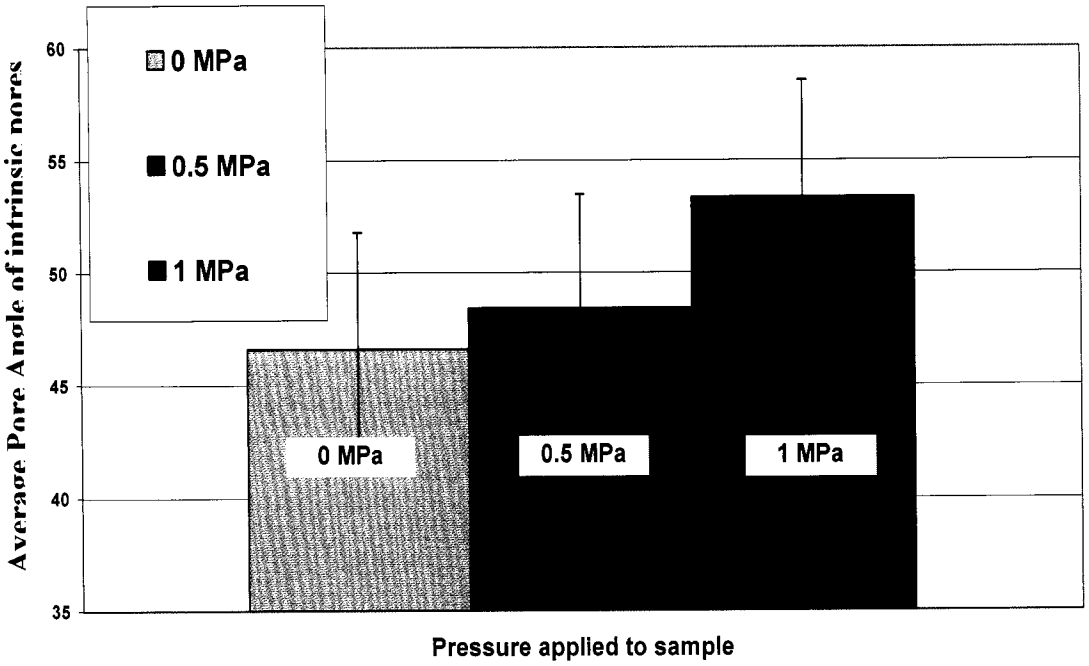

Figure 5.16 Pore orientation of artificially introduced 0.5μm pores in sinter-forged 0.25μm powder YSZ. The behavior is expected for intrinsic pores.

V.4.2 Evolution of Intrinsic Pore Anisotropy in Slip Cast Samples

The evolution of anisotropy of intrinsic pores as a function of temperature and nominal stress during sinter-forging has been investigated in tape cast YSZ films (Section V.3). However, due to the pre-existing anisotropy in the tape cast films it is desirable to further investigate the evolution of intrinsic pore anisotropy in a more controlled system without a large pre-existing microstructure anisotropy. This investigation in anisotropic intrinsic pore development will be to quantify the pore shape and size with respect to isothermal sintering temperature and uniaxial stress. The same method used for controlling pore size in the pore transition study will be used to study intrinsic pores. YSZ samples (powder size 0.5μm) with 0.2μm polystyrene spheres will be sinter-forged

at 0.0, 0.5 and 1.0 MPa. It has been shown earlier that pores of this size behave like intrinsic pores. The sintering temperatures will be 1250, 1300, and 1350°C. The cross-section of the samples will be analyzed using ImageJ to measure anisotropy.

In an unloaded sample the average pore angle should be around 45° to be called isotropic. In Figure 5.17 the average intrinsic pore angles for the samples at given temperatures and loads are shown. The unloaded pore angels are 46, 42 and 41°. These values are much closer to 45° than the tape cast samples.

The increase of pore angle orientation towards the uniaxial load with load is consistent in all samples except the 1350°C 1MPa sample, but the difference is small enough between the 0.5 MPa sample and 1 MPa sample that it is insignificant. The dependence of temperature on the pore orientation does not appear to be significant except for the 1250°C sample. The difference in these samples is probably the much lower sample density due to the lower sintering temperature.

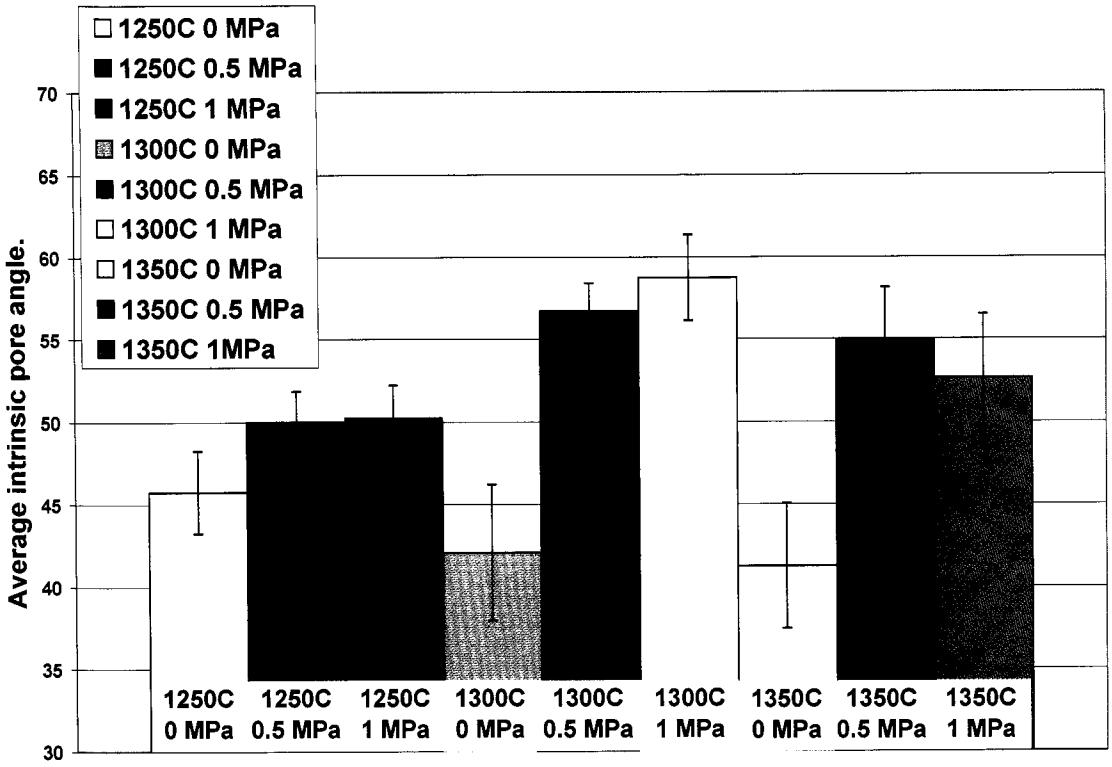

Figure 5.17 Average intrinsic pore angles for sinter-forged YSZ samples. Effect of temperature and nominal axial stress.

One interesting observation in the image analysis for the intrinsic pores is the dependence of anisotropy on the density of the sample. For the 0.2μm introduced pores, in the early stages of the study the pores were difficult to find, so images were taken where there were fewer pores. In these first samples where pores were difficult to find, the localized density was much higher; meaning that some areas of a sample were denser than others. When the pores were analyzed for orientation, all samples returned an orientation of around 45°. An example of these samples images is shown in Figure 5.18. Comparing this image to figure 5.12, you can see the significant difference in localized density.

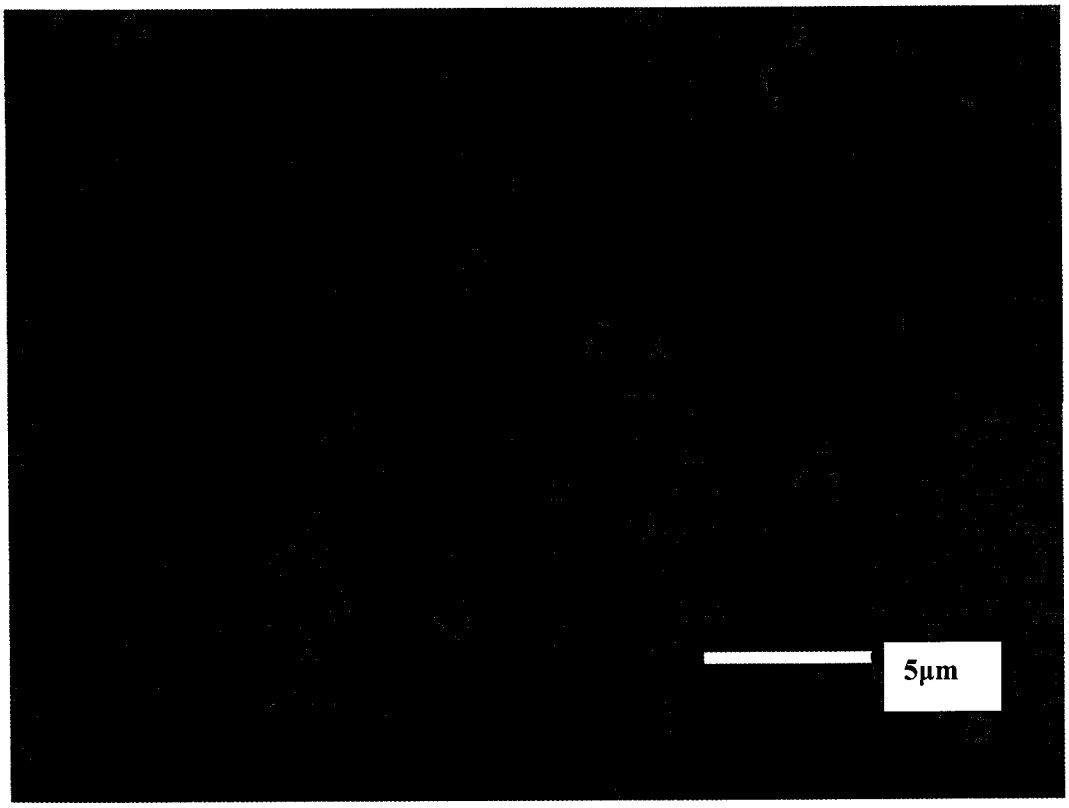

Figure 5.18 Sinter-forged sample with intrinsic pores in regions of high density

When the samples were re-done, areas of density consistent with what has been studied in this dissertation (meaning that there were just more pores present) were analyzed. When these areas were analyzed the results presented in Figure 5.17 were observed. Why would there be anisotropy in a sample with more pores (less density), and less anisotropy with fewer pores (higher density)? One possible explanation is a source-sink relationship. From the limited observations in this dissertation, it appears that intrinsic pores are more anisotropic at lower density. This observation needs to be further investigated and the causes of it studied. Plausible causes include transition from grain boundary to surface diffusion dominated regime or changes in diffusion distance. One

other study by Zuo et al. on intrinsic pore anisotropy also focused on samples with about 80% density [4].

V.4.3 Evolution of Extrinsic Pore Anisotropy in Slip Cast Samples

In the anisotropic study in tape cast YSZ films, it was observed that larger extrinsic pores behave differently than smaller intrinsic pores. This led to the investigation of the transition point between the two types of pores. However, it was noted that the tape cast films are anisotropic due to casting and this complicated the conclusions regarding the effect of temperature and load on the evolution of anisotropy. To correct this, slip cast samples have also been studied. In the last sub-section, the evolution of anisotropy for intrinsic pores was presented. Here the focus is on extrinsic pores.

This investigation into the evolution of extrinsic pores will quantify the pore shape and size with respect to isothermal sintering temperature and uniaxial stress. The same method used for controlling pore size in the intrinsic pore study will be used here. YSZ samples with 2.0μm polystyrene spheres will be sinter-forged at 0.0, 0.5 and 1.0 MPa. The sintering temperatures will be 1250, 1300, and 1350°C. The cross-section of the samples will be analyzed using ImageJ to quantify anisotropy.

In an unloaded sample the average pore angle should be around 45° to be called isotropic. In Figure 5.19 the average angles for the long axis of the extrinsic pores for the samples at given temperatures are shown. These angles for the unloaded samples are 38, 39 and 43° for the different temperatures. These values are a little lower than what would be ideal. It is not clear why the 0 MPa have a slight anisotropy to begin with. The pores analyzed for this calculation are the artificially introduced pores, and there was no load to deform them.

As can be seen in Figure 5.19, the pore orientations change significantly for the loaded samples. This is consistent with what was observed for the intrinsic pores. However, unlike the intrinsic pores, for the extrinsic pores, as the load increases, the pores tend to orient perpendicular to the axis of the load. This is the same behavior that was observed for the extrinsic pores in the tape cast samples.

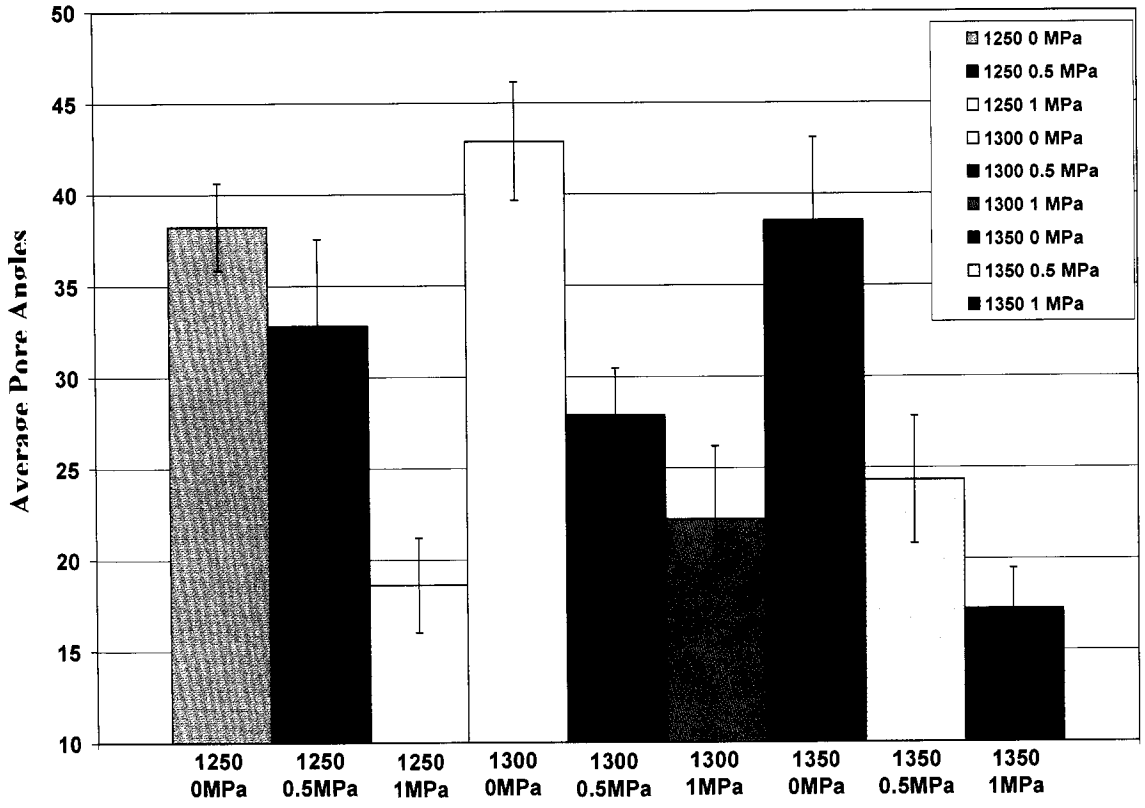

Figure 5.19 Extrinsic pore orientation in sinter-forged YSZ samples. Effect of the temperature and nominal external load.

One observation of the pore orientation angles brings up an important question. Why is the magnitude of the pore anisotropy for the intrinsic pores not as significant as the anisotropy developed for the extrinsic pores? For the extrinsic pores it was possible to get an orientation angle down to about 17°, which is a 28° difference from isotropic (45°). In the intrinsic pore experiment the most anisotropic measured was about 58°, or 13° difference from isotropic.

A possible explanation is that there is a strong driving force for sintering for the small radius pore tips that are being created for intrinsic pores. As these pores are developing anisotropically, the driving force to sinter the tip is counteracting some of the orientation development. The pores do still develop anisotropy parallel to the load, but the magnitude of anisotropy is not as great as it would be if the act of doing so did not also increase the sintering rate of the pore tips. This is not seen for the extrinsic pores because even though the pore tip radii are decreasing during sinter-forging, they are still much larger than any of the pore tips in the intrinsic pores. The increased sintering rate due to the decreased pore tip radius is just too small to have any effect on the pores anisotropy.

V.5 ANISOTROPY IN CONSTRAINED YSZ FILMS

In the previous sections the anisotropy of natural or artificially introduced pores was investigated in sinter-forged samples. The sinter-forging-to-constrained sintering analogy implies that the behavior observed in sinter-forging samples would also be seen in constrained samples. From the results shown, the investigation of natural pores in a naturally constrained film is of much interest. The goal of this section is to investigate the evolution of anisotropy in constrained films by focusing on intrinsic pores.

For this experiment, the constrained films were made by centrifugal casting, explained in detail in Section IV.3.1.3. The films were made with a high green density, as a result

there are very few natural large pores in the film. Most of the pores, as shown in Fig 5.20, are in the size scale of intrinsic pores. The films were sintered at 1350°C for 1hr. By using ImageJ, the porosity of the film can be calculated. The overall porosity of the film is calculated at about 20%, giving us a film density of about 80%.

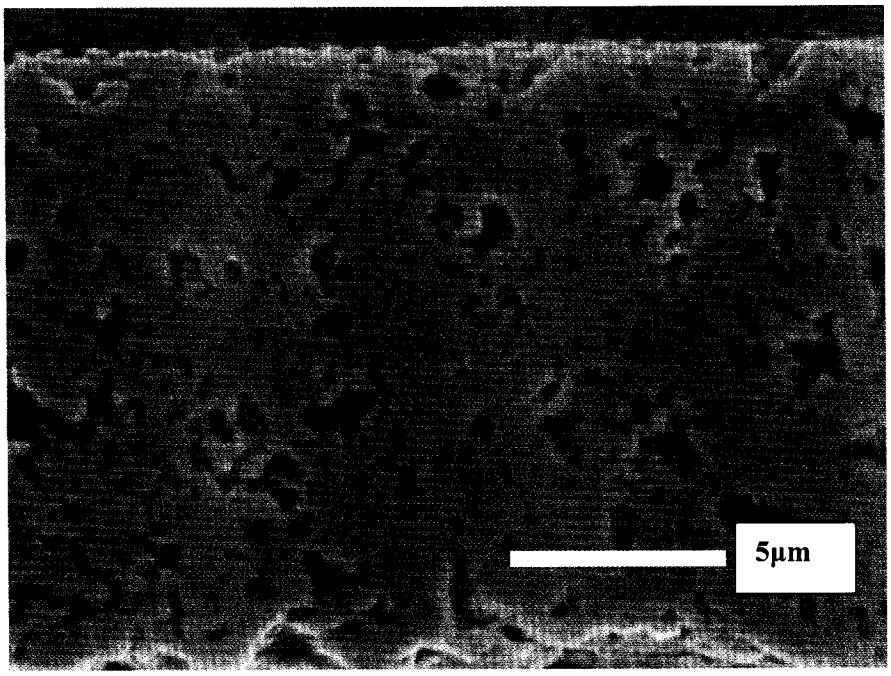

Figure 5.20 Cross-section of a constrained sintered YSZ film. Sintered at 1350°C for 1 hour.

By analyzing the intrinsic pores in the film, the average pore orientation can be determined. The few larger extrinsic pores were excluded from the analysis. Using the same method used in the previous studies, the average intrinsic pore anisotropy of the constrained film, as shown in Figure 5.21, is calculated at about 53°. Results are presented for three different films sintered at 1350°C for 1 hour.

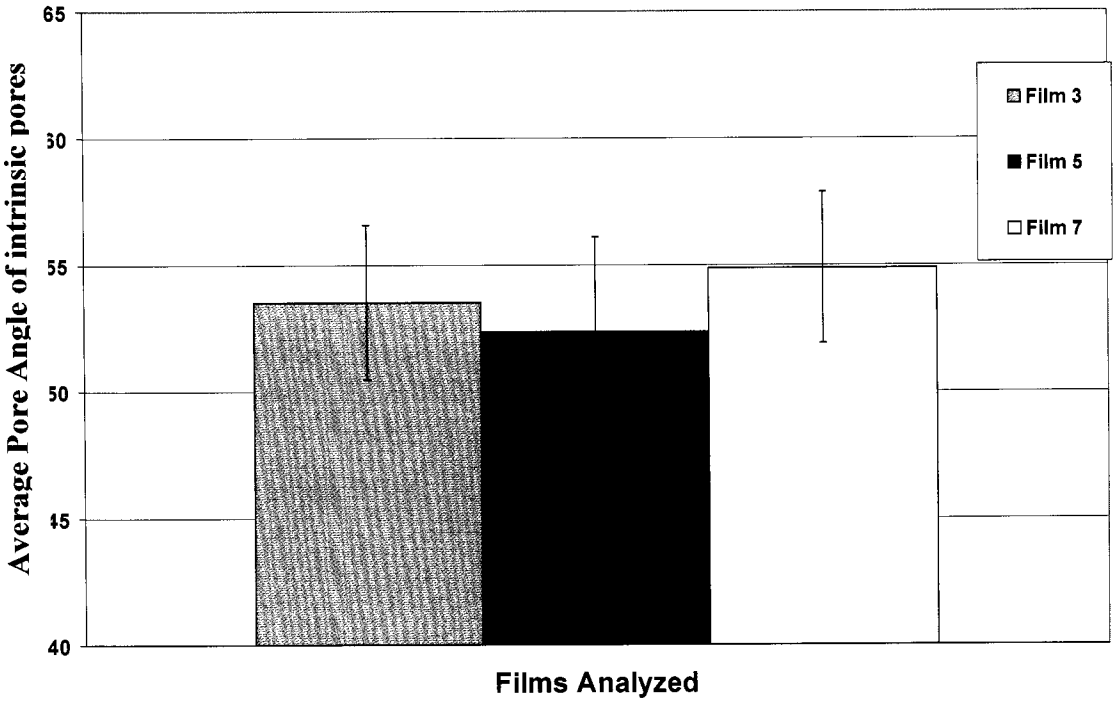

Figure 5.21 Intrinsic pore orientations in constrained sintered YSZ films. The films were sintered at 1350°C for 1 hour.

It is important to note that this average pore orientation angle is very close to the average pore orientation angle for the sinter-forged YSZ compact with controlled size intrinsic pores in Section V.4.2. The average pore orientation of the 1MPa samples was about 54°. This pore orientation is also very close to the measured pore orientation for the 1MPa sinter-forged samples of 0.25μm powder experiment of 53° (Section V.4.1). These results in the constrained YSZ film add validity to the experiments and results in the controlled intrinsic pore sinter-forged samples in both the 0.25μm and the 0.5μm YSZ powder that they can accurately mimic a constrained system.

While it was also the intention of this experiment to analyze the orientation of extrinsic pores in the naturally constrained samples, green state processing of constrained films with a uniform distribution of extrinsic pores turned out to be too difficult. The size of the pores would each be about $1/5^{th}$ the thickness of the film. Processing films with defects that large while still adhering to the substrate and still being a continuous film is very difficult. Using polystyrene spheres also did not work, as the spheres separated from heavier ceramic particles during centrifugal casting (the main method used in this dissertation to make constrained films).

V.6 CONCLUSIONS

- An investigation into the microstructural evolution of tape cast YSZ films has shown that the uniaxial loading of the sample leads to modified densification. The densification increased as the compressive load increased.

- The second part of this investigation into sinter-forging tape cast YSZ films demonstrated that uniaxial compressive loading leads to anisotropic pore development. The intrinsic pores preferentially oriented their long axis parallel to the uniaxial loading direction. The experiments showed that an increase in the axial stress leads to an increase in the extent of pore orientation anisotropy.

- A study of the behavior of pores based on size using controlled sized pores showed that there is a transition point between intrinsic pores and extrinsic pores. This transition point is where uniaxially loaded pores switch from orienting parallel to the compressive load, to perpendicular to the load. For sinter-forging 0.5μm particle size compacts with a nominal compressive stress of 1.0MPa, the critical size at which this transition occurs is approximately 1μm. Pores of this size remain isotropic even in the sinter-forged samples.

- A further investigation into this pore behavior transition point used a smaller particle sized YSZ powder with polystyrene spheres twice the powder diameter to determine if this transition point scaled with the powder size. The results showed that the transition point does not scale linearly with the particle size, and these pores behaved similarly as they would in a sample with larger initial powder diameter.

- An in-depth investigation was done to further quantify the behavior of the intrinsic pores anisotropic development. The orientation showed a strong

dependence on uniaxial load, and no significant relationship to temperature. The intrinsic pores preferentially oriented themselves parallel to the uniaxial load.The magnitude of the intrinsic pore re-orientation was not significant, the average pore angle was about 53° (as compared to 45° for isotropic).

- An in-depth investigation was also done to further quantify the behavior of micr-pore anisotroic development. These pores orientation also showed a strong dependence on uniaxial load, and no significant relationship to temperature. The extrinsic pores preferentially oriented themselves perpendicular to the uniaxial load. The magnitude of the pore re-orientation was more significant, with the 1MPa samples average angle about 20° (compared to 45° for isotropic).

- The microstructure of a constrained YSZ film was analyzed to compare to the sinter-forged samples which are intended to potentially mimic constrained or partially constrained systems. Intrinsic pore orientations in samples of similar density to that studied in the other experiments were investigated. The pores showed a preferential orientation of their pores perpendicular to that of the substrate (same direction as in the loaded samples). The average pore orientation was about 53°. This is extremely close to what was observed in the 1MPa sinter-forged samples (the samples closest to full constraint).

- The lower magnitude of re-orientation of the intrinsic pores during constrained sintering or sinter-forging is postulated to be due to the healing of these pores as a result of the high driving forces to sinter these pores of sharp radius of curvature. The increased sintering of the pore tip was not seen in the extrinsic pores as the tip radius is still much larger than the intrinsic pores.

- Another observation during the pore orientation investigation is the dependence of anisotropy to the localized density of the region that the pore is in. In a sinter-

forged sample, if an isolated pore is in a region of high density the pore will be isotropic, and if a pore is in a region of low density it will be anisotropic. This is postulated to be due to the atom source-sink relationship. The pore in the high density region has a large source to feed the sintering of the pore tip, whereas a pore in a low density region has few sources to fill the sink (pore tip).

Notes to Chapter V

1. Bordia, R.K. and Raj, R., *Sintering behavior of ceramic films constrained by a rigid substrate.* Journal of the American Ceramic Society, 1985. 68(6): p. 287-292.

2. Salamone, S., *Densification of and constitutive laws for ceramic matrix composites and multilayered systems* 2003, University of Washington. p. 214.

3. Speight, M.V. and Harris, J.E., *Kinetics of stress-induced growth of grain-boundary voids.* Metal Science Journal, 1967. 1: p. 83-85.

4. Zuo, R., Aulbach, E., Bordia, R.K. and Roedel, J., *Critical evaluation of hot forging experiments: Case study in alumina.* Journal of the American Ceramic Society, 2003. 86(7): p. 1099-1105.

CHAPTER VI

RESULTS AND DISCUSSION: CRACK AND HOLE GROWTH IN CONSTRAINED YSZ FILMS

VI.1 INTRODUCTION

While sintering a ceramic film on a substrate, in-plane stresses develop in the two layers due to their sintering rate mismatches. These stresses can lead to warping, cracking, anisotropic microstructural development, or the growth of other instabilities [1-4]. The goal of this part of the dissertation was to increase the fundamental understanding of how defects develop in a constrained film and to understand the stresses that cause them, in order to avoid, fix, or prevent them in the manufacturing of SOFCs.

One method that is being used to enhance the performance of SOFCs is to use thinner layers in the cells to decrease electrical resistance. Using thinner layers of YSZ is very successful at increasing the power density of a SOFC [5, 6], however it also increases the chance of cell failure during thermal cycling. As SOFCs heat and cool during operation, thermal expansion within the cell creates a potential for cell failure due to crack propagation in the multi-layer system when component materials are not strong enough. Increasing the long-term reliability of SOFCs is dependent upon increasing the strength of the ceramic films. This can be accomplished by a reduction in the number and size of flaws created in the ceramic during processing. The presence of micro-cracks, holes, and anisotropic pores all contribute to reducing the strength of the material.

The stresses that are created by the densification of a constrained layer can lead to micro-crack and micro-hole growth. Previous theoretical and experimental work done by Bordia and Jagota [2] on sintering constrained silica films on different substrates

showed that there is a critical film thickness, and a critical crack size above which the crack will grow and below which it will not. Their experimental results on glass films are in good agreement with their analysis. However, their study of crack growth in crystalline alumina films used introduced cracks that were many times wider than the width of the particles and did not go all the way through the film. Thus, their results on polycrystalline films were not conclusive.

In this project, the focus has been on investigating the parameters that control crack/hole growth in constrained sintering YSZ polycrystalline films. To create smaller and more controlled cracks and holes, a focused ion beam was used to make a crack, with a crack tip radius on the order of a few particles wide, all the way through the thickness of the film. These constrained films were then sintered and the evolution of the defects was studied to determine the critical parameters for propagation. Due to the technique of introducing cracks, these cracks are both good model cracks and representative of the expected initial defects in thin films.

Understanding the critical parameters that determine flaw propagation is important to control defects in films. Not only will a better understanding of how the film will behave increase the predictability of the sintering behavior, it will also provide processing guidance to sinter films under conditions that strength-limiting flaws can be avoided. Thus, this part of the research has focused on improving the reliability of SOFCs.

This research was conducted by the author as an exchange scholar in the Fracture & Reliability Research Institute led by Prof. Tetsuo Shoji at Tohoku University in Sendai, Japan.

VI.2 FRICTION BETWEEN THE SUBSTRATE AND THE SINTERING FILM

The interfacial friction between the constrained sintering ceramic film and the constraining substrate has a large role in the growth of cracks and defects on the film [2, 7, 8]. In order to fully understand the growth behavior of the introduced defects, the friction between the film and the substrate must be measured and controlled.

In order to measure interfacial friction, an experimental technique proposed in Ref. 2 was used. A cut was made across the entire film width all the way to the substrate. The amount the edge of the film recedes after sintering can be used to quantify the friction parameter for the interface [2]. To make this cut across the entire film and completely through the thickness of the film a femto-second laser was used. The FIB used for the defect introduction is too slow to make this cut, which the femto-second laser could make in a fraction of a second. The films used for this experiment were the thinnest films studied (thickness equaled 10μm). In order to vary the interfacial friction, three different substrates were used: polycrystalline alumina 99.8% purity, single crystal sapphire, and platinum coated sapphire. The unsintered films were placed under the femto-second laser beam using a #2 Aperture and 50mm lens. The focus point of the laser was difficult to control, which led to the larger width of the cuts than desired. However, as shown in Figure 6.1, the cuts were well defined and sufficient for the measurements.

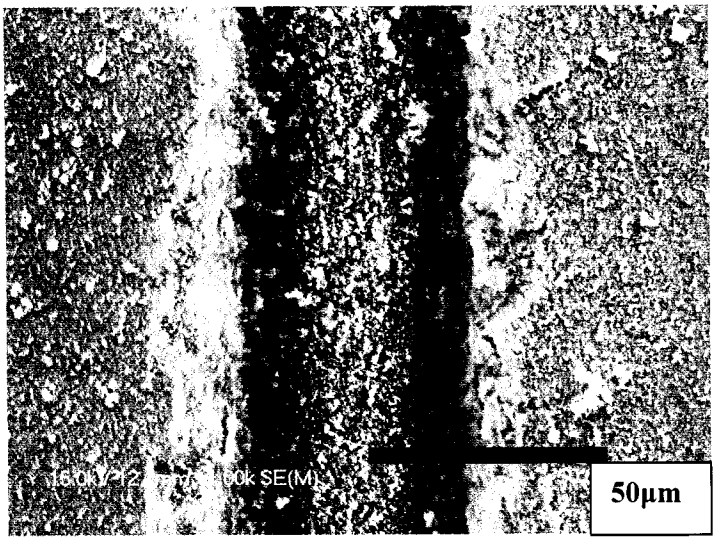

Figure 6.1 Milled cut in an unsintered film using a femto-second laser

After the cut was milled using the femto-second laser, the films were sintered using the same heating profile that was used on all FIB'd films. The heating rate from room temperature was 2°C/min to the isothermal temperature of 1350°C. The isothermal temperature was held for one hour and then the sample was cooled at 2°C/min back to room temperature. As can be seen in Figure 6.2, the milling path of the laser is still visible on the substrate. To analyze the friction of each sample, the width of each milled cut was measured before and after sintering in many places along its length. The average increase in width, as well as the average distance the free edge traveled was calculated for each substrate. These measurements are shown in Table 6.1. As was shown in Ref. 2, the interfacial friction is inversely proportional to the displacement of the free edge. The measurements show that the friction of the platinum substrate is much lower than that of the alumina or sapphire substrates, while the alumina has slightly larger friction than that of the sapphire. This similarity in the alumina and sapphire substrates is expected since both of them are polished high purity Al_2O_3. The

results are in good agreement with the measured friction parameters for alumina films on sapphire and platinum coated sapphire [2].

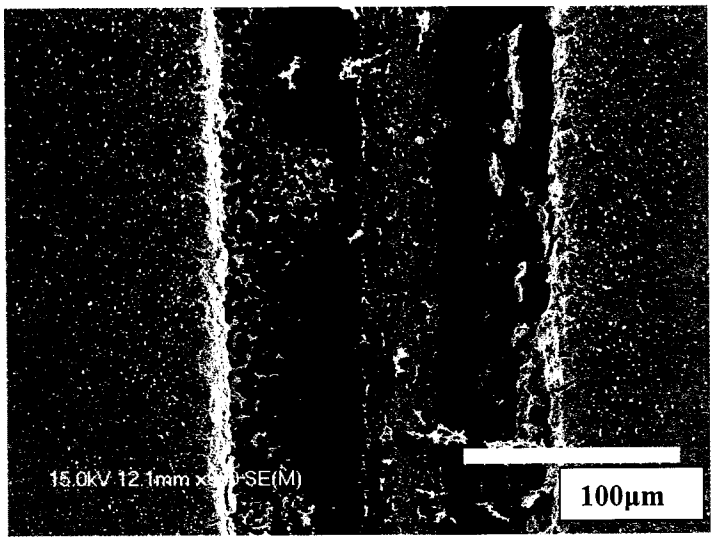

Figure 6.2 Sintered film with laser milled cut. Note the initial trace of the cut and the film opening.

Table 6.1 Measured behavior of receding free-edge cut in 10µm YSZ films via a femto-second laser

Substrate	Avg. Initial Width (µm)	Avg. Final Width (µm)	% Increase in width	Avg. Distance Free Edge Traveled (µm)
Alumina	38	60	58	11
Pt	38	170	347	66
Sapphire	38	68	79	15

In order to be able to be able to compare the friction between the different substrates and film thickness a friction parameter will be calculated. The value, k, will be calculated as the inverse distance a free edge travels for each sample as shown in Equation (6.1). This method was proposed by Bordia and Jagota [2].

$$k = \frac{1}{x} \tag{6.1}$$

The measured free edge distance traveled by the samples for the various substrates was only measured for the 10μm film thickness samples due to limited substrates. In order to get friction parameter values for the other films thickness, the values are calculated using Equation (6.2) for alumina and sapphire and Equation (6.3) for platinum. The 1/k value for alumina and sapphire scales roughly with the thickness of the film, while the 1/k value for platinum scales as the square root of the thickness [2, 9]. The calculated values for the friction parameter are shown in Table 6.2.

$$\frac{1}{k} = z \tag{6.2}$$

$$\frac{1}{k} = \sqrt{z} \tag{6.3}$$

Table 6.2 Values of friction parameter, k, for YSZ films of different thickness on different substrates.

Thickness / Substrate	10μm	20μm	40μm
Alumina	0.091 (1/μm)	0.045	0.023
Sapphire	0.066	0.033	0.016
Platinum	0.015	0.011	0.007

VI.3 INTRODUCTION OF CRACKS & HOLES IN GREEN FILMS

The cracks and holes were introduced in the green films using a Focused Ion Beam (FIB). This novel technique allowed the introduction of micron scale defects into a fragile "green" film without damaging the surrounding film. These artificially introduced cracks are intended to mimic a possible crack or processing defect in the film. With the mean particle diameter size being 0.5μm, it was desirable to create cracks with widths within one order of magnitude. The programmed width pattern was 2μm, but due to vibrations and beam instability the widths of the milled cracks were about 4μm. The length of the crack was varied in order to investigate the effect of initial crack length. The lengths of the cracks chosen were 10, 30, and 50μm. A representative example of an introduced 50μm crack is shown in Figure 6.3. YSZ films on three different substrates (polycrystalline alumina, sapphire, and platinum coated sapphire) were studied.

The holes that were introduced were intended to mimic a processing pinhole or other defect with round features. The holes that were introduced were actually rings, as less

material needed to be removed. As can be seen in Figure 6.4, the width of the circle did vary slightly due to vibrations and beam instability.

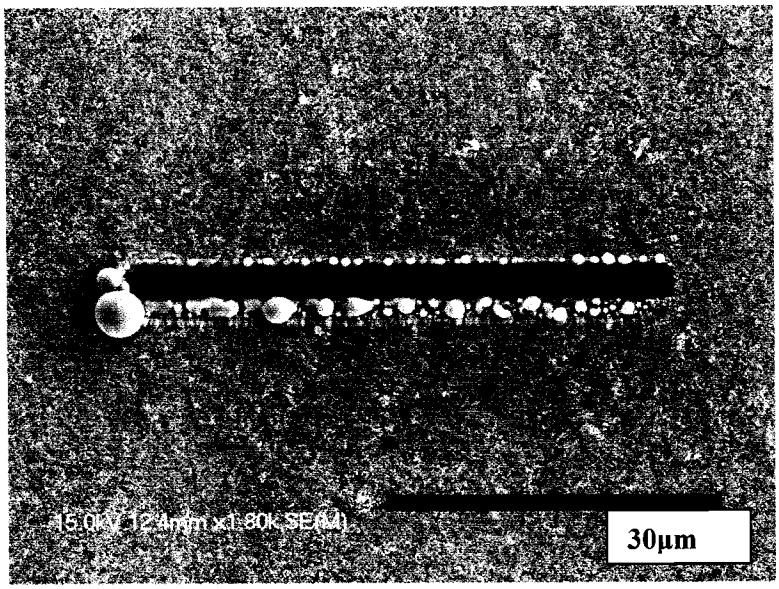

Figure 6.3 FIB introduced crack into green film

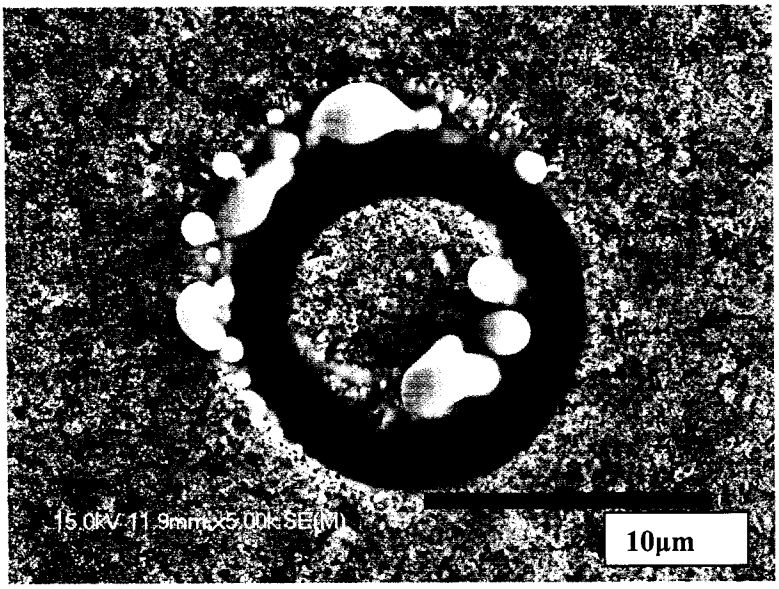

Figure 6.4 FIB milled circle into green YSZ film

The FIB took considerable time to remove the large amount of material needed to create cracks and holes that continued all the way to the interface. For some of the long cracks in the thick films, the milling could take 5-8 hours for one crack. The long time that was needed to create these defects, led to unexpected results created by the Gallium-ion FIB. The first is that there was deposition of gallium metal at the perimeter of the crack during milling. Figure 6.5 shows spherical gallium droplets around the rim and along the sides of the crack. This had no effect on the sintering behavior, as the metal vaporizes at significantly lower temperature than the sintering temperature.

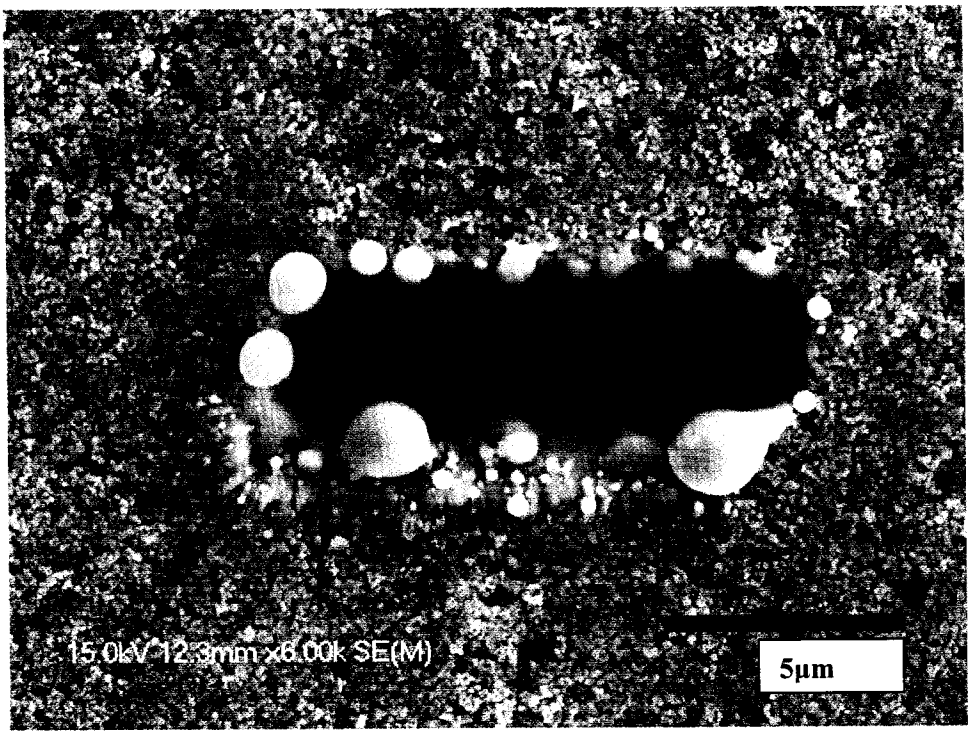

Figure 6.5 FIB'd crack showing the gallium metal deposits on the perimeter

The second phenomenon that the FIB created in the film is the partial sintering of the crack/hole walls. The extensive amount of milling time lead to the sintering of the particles exposed to the beam on the walls of the cracks/holes. Figure 6.6 is an image looking down the wall of a milled feature. The grain growth of the particles on the wall that were exposed for extended amounts of time can clearly be seen. The FIB causes localized heating of the particles to temperatures high enough to partially sinter them.

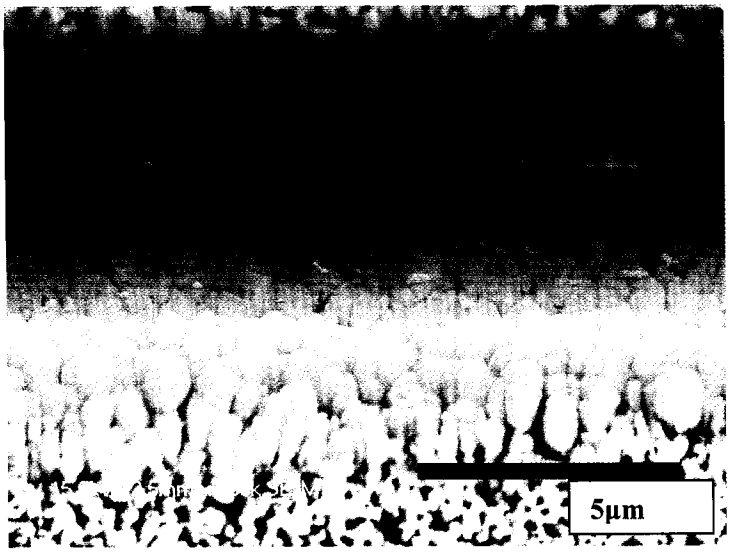

Figure 6.6 Sintered walls of a FIB introduced feature

The crack tip on the FIB'd feature did not however show sintering behavior. This was more likely due to the drift of the beam, and the shorter time the crack tip was exposed to the beam. As a result, it is postulated that crack growth parallel to the initial crack was not affected by this local sintering. However, there are some questions regarding the validity of the observations related to growth of the defects perpendicular to the cracks. Although initially it was a concern that the partially sintered walls would prevent crack growth in the perpendicular direction, observations of sintered samples indicates that this was not a significant effect. This is illustrated in Figures 6.7-6.9 (sintered films with cracks) and Figures 6.12 and 6.13 (sintered films with rings). In both these cases, there is void and crack growth, and also formation of channel cracks (discussed later) behind the sintered walls. These figures are discussed in detail in the following sections.

VI.4 MICROSTRUCTURE ANALYSIS OF CRACK GROWTH

After sintering the samples with introduced defects at 1350°C for 1 hour the growth of the defects was analyzed using SEM micrographs. The micrographs of one of each sample after sintering are shown in Figures 6.7-6.9. The new crack length and width was measured; multiple measurements for each were taken. Qualitative observations were also made regarding crack shape and damage in the surrounding films as discussed below.

From looking at the pictures of all the YSZ films on the alumina and sapphire substrate sample photos in Figures 6.7-6.9, it's difficult to tell them apart. The amount and character of the growth appears very similar. This can be attributed to the similarity in friction of the two materials. The cracks in the YSZ films on the platinum substrates do however show that the low interfacial friction of the films on this substrate leads to much larger crack growth and wider crack openings during sintering.

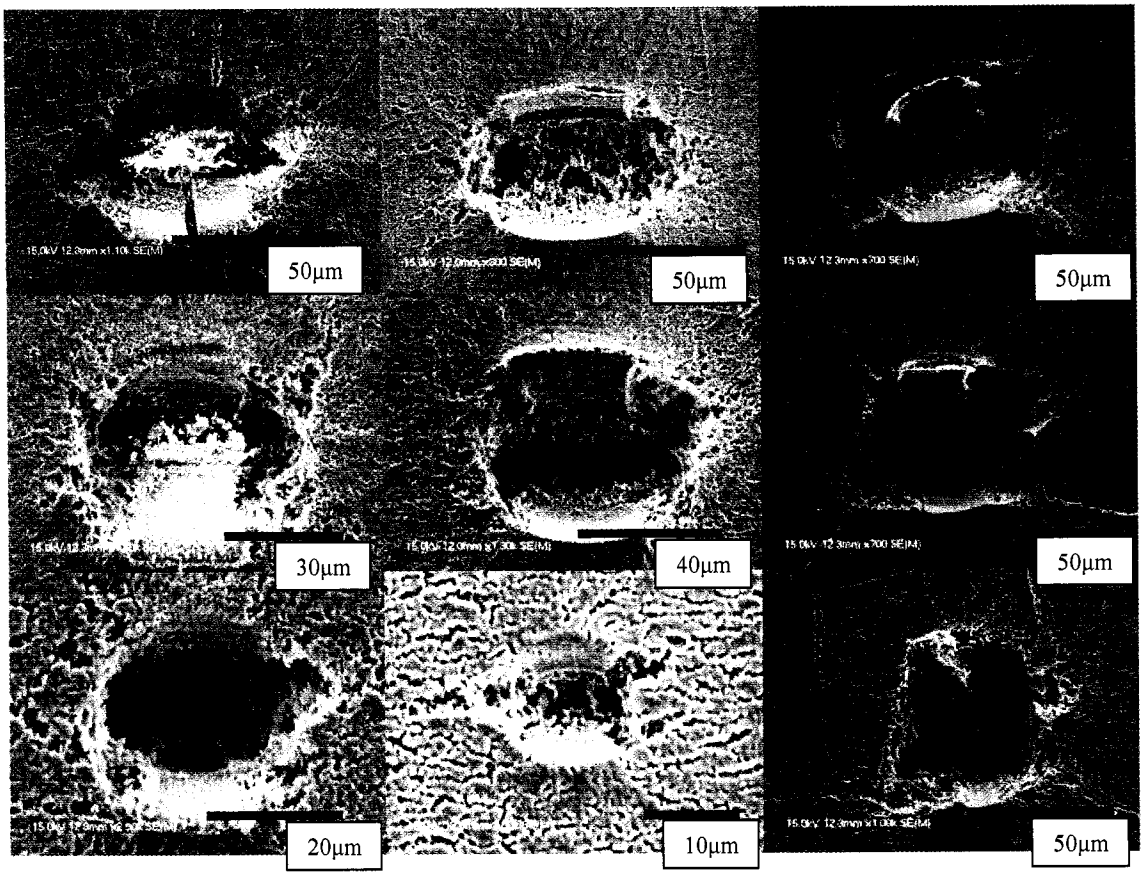

Figure 6.7 Sintered YSZ films (initial thickness ~38µm thick) with cracks of different initial length on different substrates. The films of this thickness are referred to as Sample A in the discussion: Alumina substrates (Left column), Pt coated sapphire substrates (Middle column), Sapphire substrate (Right column) Crack length: 50µm (top row), 30µm (middle row), 10µm (bottom row)

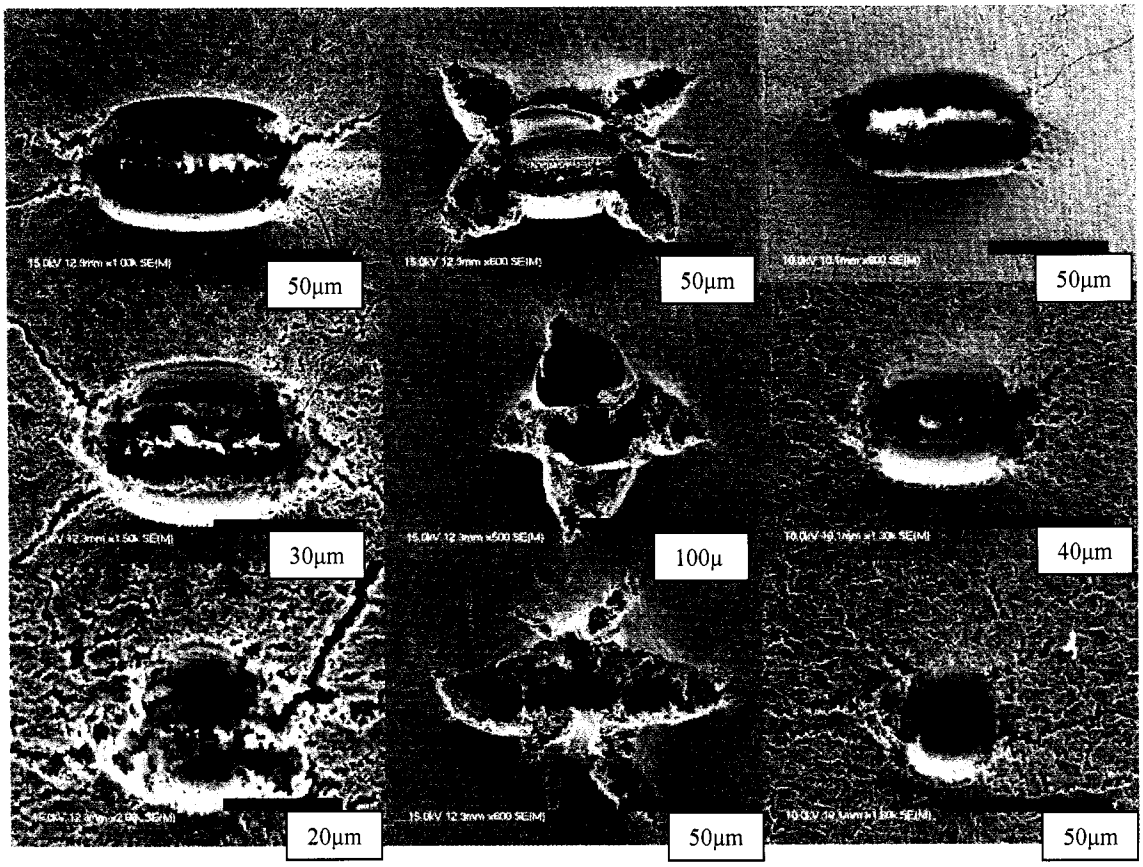

Figure 6.8 Sintered YSZ films (initial thickness ~19µm thick) with cracks of different initial length on different substrates. The films of this thickness are referred to as Sample B in the discussion: Alumina substrates (Left column), Pt coated sapphire substrates (Middle column), Sapphire substrate (Right column) Crack length: 50µm (top row), 30µm (middle row), 10µm (bottom row)

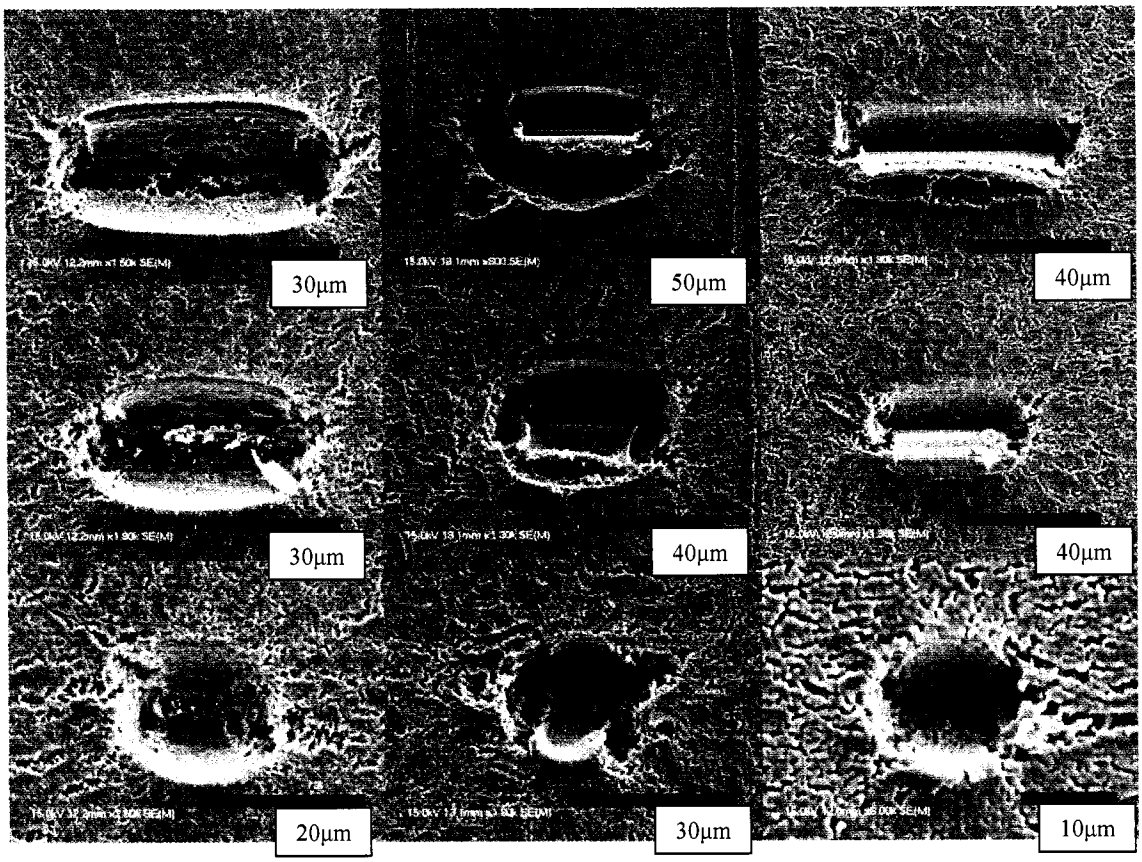

Figure 6.9 Sintered YSZ films (initial thickness ~10μm thick) with cracks of different initial length on different substrates. The films of this thickness are refered to as Sample C in the discussion: Alumina substrates (Left column), Pt coated sapphire substrates (Middle column), Sapphire substrate (Right column) Crack length: 50μm (top row), 30μm (middle row), 10μm (bottom row)

After sintering, the shortest cracks (10μm) turned into ovals, if not circles in most samples. This growth appears to be a function of the length to width ratio of the cracks. As the cracks get smaller, the length to width ratio drops to about 2.5:1 in this case. This geometry is much more susceptible to rounding than the larger cracks where the length to width ratio is up to 13:1. Another observation from the images in Figures 6.7 – 6.9 is that as the film gets thicker, the cracks tend to become more rounded at the top, similar to how the smaller cracks behave for all film thickness. This is due to the reduced affect of the interfacial constraint to restrict flow at the top of the film far away from the interface. Jagota and Hui discussed this based on the wetting factor [8]. This is evidence of the variation of stress along the thickness of the film.

The graph in Figure 6.10 shows the percent crack elongation of the top of the crack versus initial crack length. There are two important observations. First, for all crack lengths and film thickness, cracks on Pt-coated substrates grow more than those on alumina and sapphire. This is because of the lower interfacial friction between the film on this substrate and is as would be expected. The second observation is that on a percentage basis the smaller cracks grow more. This is an interesting observation which is not intuitively expected. In general longer cracks have higher stress intensity and therefore maybe expected to grow more. However, the explanation for this may lie in the fact that the longer cracks may be approaching the long crack limit as described in Ref. 2 and may have stress intensities that are independent of crack length. Another explanation may lie in the fact that cracks in these films grow by diffusion (as apposed to elastic crack growth) and the dependence of this on crack length maybe different.

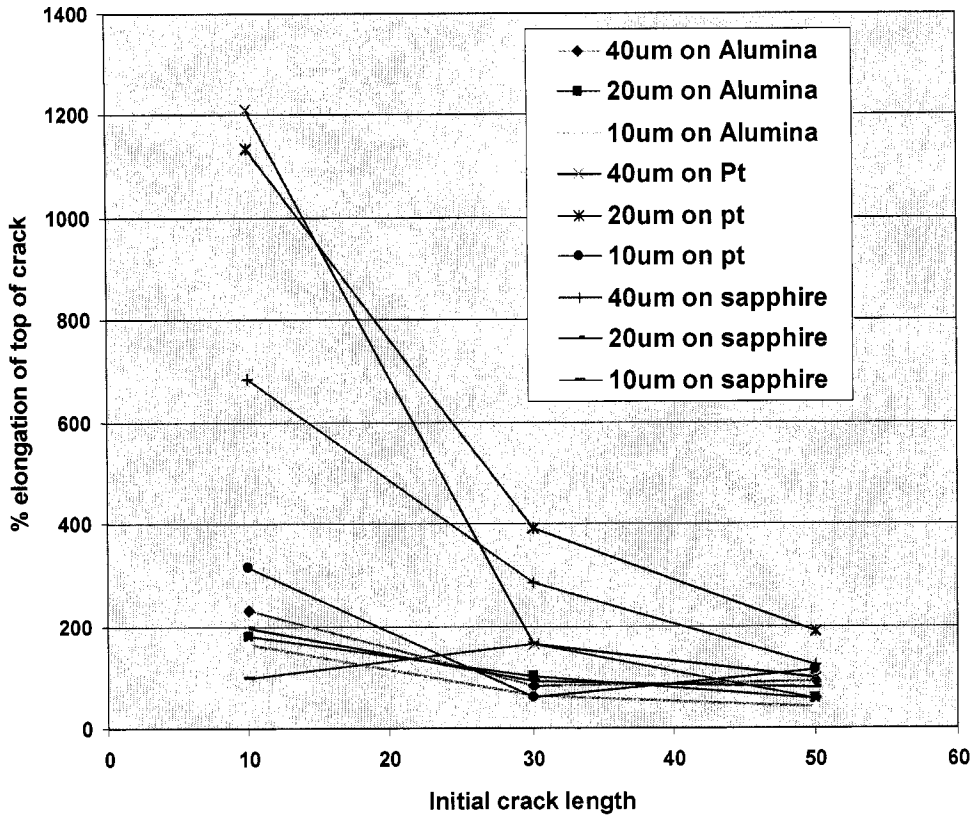

Figure 6.10 Percent crack elongation vs. initial crack length for YSZ films of different thickness on three substrates

The graph in Figure 6.11 shows the maximum percent crack width opening at the top of the crack versus the initial crack length. The trend in these results, with a few exceptions, is opposite of the trend in the results of the increase in length. The crack width increase as the crack length increases. The explanation for this may be in the tendency of the cracks to evolve to an equilibrium shape. There is no analysis for this in the literature and this is the first observation of this phenomenon. Once again, for a given length, cracks grow more on Pt-coated substrates as expected.

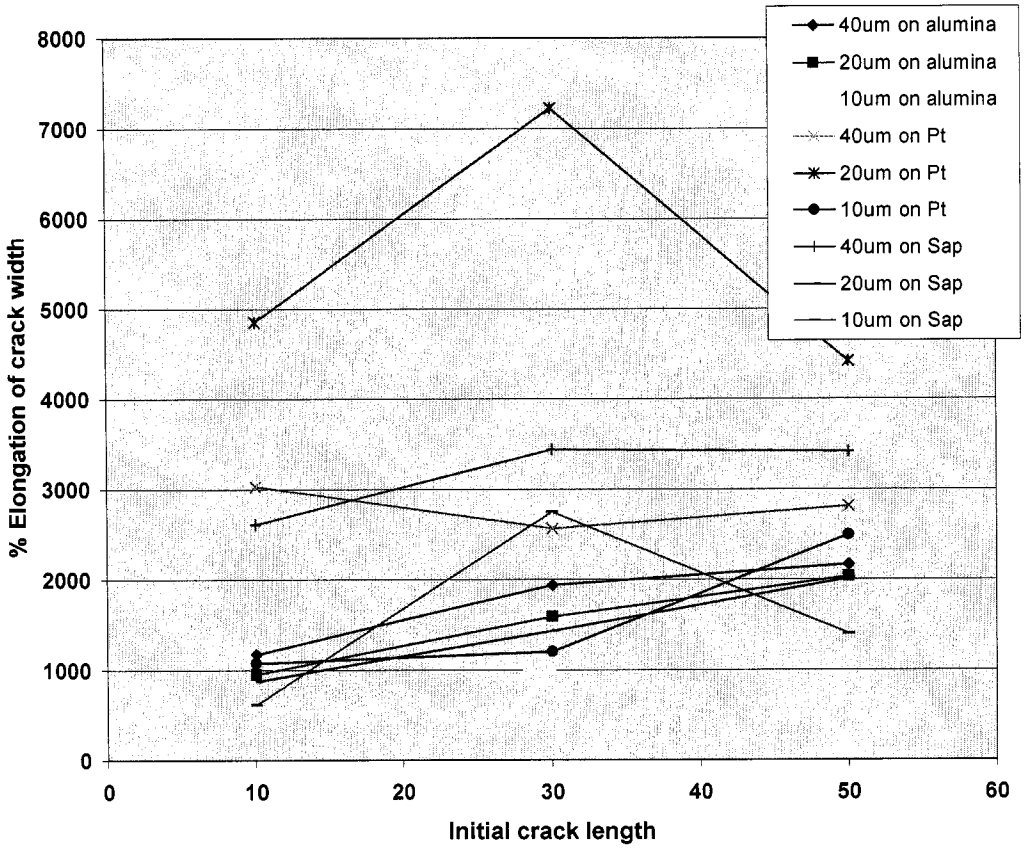

Figure 6.11 Percent crack width elongation vs. initial crack size for YSZ films of different thickness on three substrates.

The graph in Figure 6.12 is the total growth of the crack vs. the friction parameter for each sample (obtained from Table 6.2). Three sets of data have been plotted, one for each initial length of the crack. The further to the left on the graph is the lower friction samples, with the Pt substrate being furthest to the left. The further to the right is the higher friction samples, with the thinnest films on the alumina substrate being furthest to the right. Note that the friction parameter includes both the film thickness and the value of the film/substrate interface.

As can be seen, the 30μm and 50μm cracks have fairly steady growth with respect to the friction parameter between the film and the substrate. This suggests that for long cracks the extent of crack growth is independent of initial crack length. This is not the case for the 10μm cracks. At low friction the extent of crack growth is higher than predicted by steady state growth. At higher friction the crack growth is lower than what would be predicted with steady growth.

This behavior signifies a transition between small and large crack growth which maybe dependent on the friction parameter. The 30 and 50μm cracks have steady large crack growth behavior. The 10μm crack samples however do not show large crack behavior until the friction is reduced to an amount that will allow easier growth. This shows us that there is a dependence of this transition on interfacial friction.

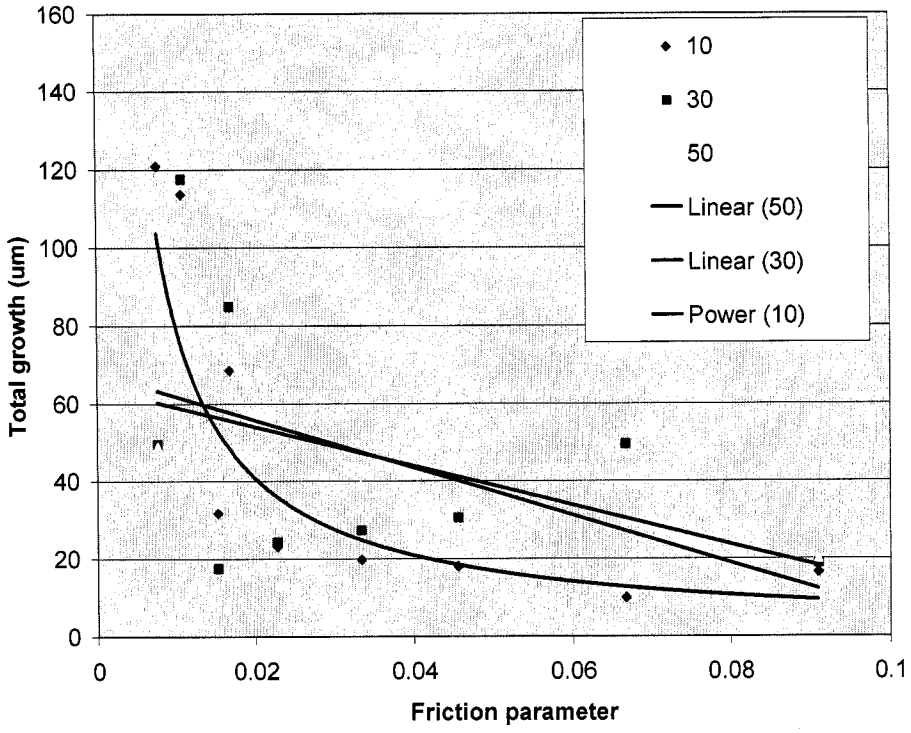

Figure 6.12 Total growth of cracks vs. friction parameter for cracks of different initial length

VI.5 ANALYSIS OF GROWTH OF MICRO-RINGS

The study of the growth of micro-rings was a good experiment to test the isotropy of the film in the X-Y plane. If there were anisotropic stress in the X-Y plane, the circle would become oval after sintering. As shown in Figures 6.13 and 6.14, the circles maintain their circularity very well after sintering. The diffused damage zone was also very homogenously distributed around them. As with the crack elongation experiments, the micrographs of these circles were analyzed for growth. The width of these rings was measured, at several locations, before and after sintering.

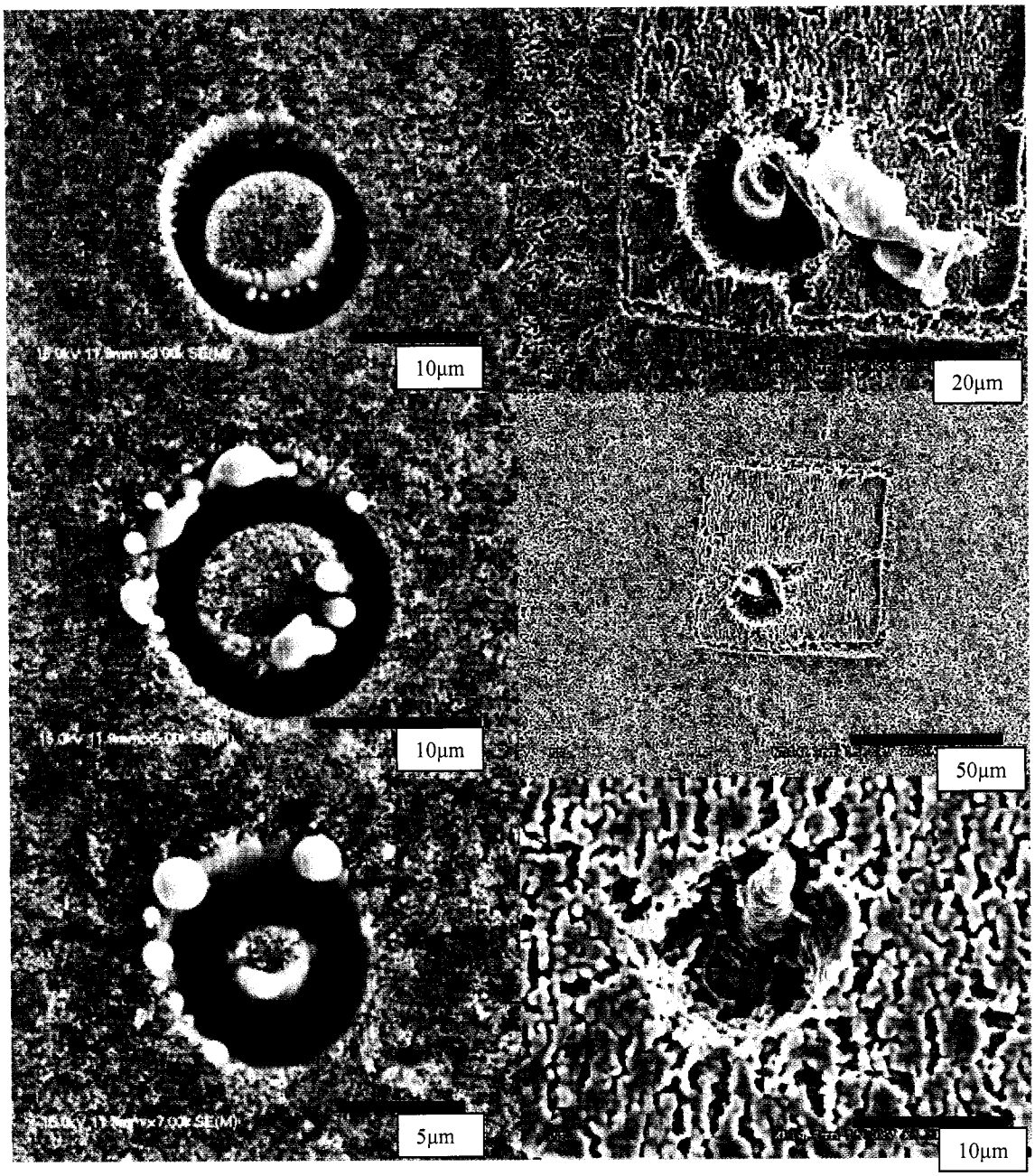

Figure 6.13 The growth of micro rings on 9μm YSZ films (Sample C) on sapphire. The rings in the top micrograph are 13um across, middle 10um, and bottom 5um. The left column shows the rings before sintering, and the right column shows the rings after sintering.

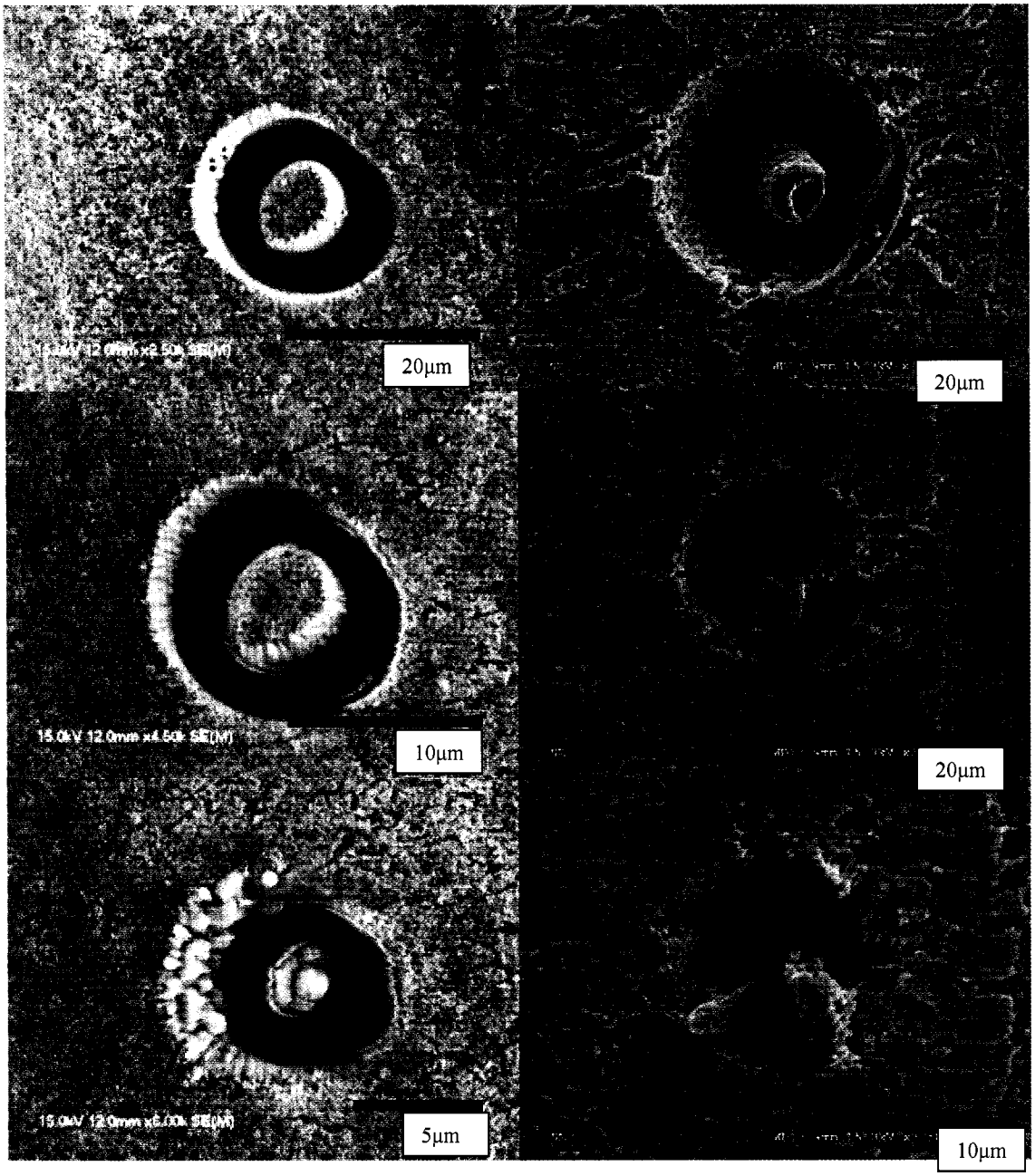

Figure 6.14 The growth of micro rings on 9µm YSZ films (Sample C) on alumina. The rings in the top micrograph are 13um across, middle 10um, and bottom 5um. The left column shows the rings before sintering, and the right column shows the rings after sintering.

The graph in Figure 6.15 shows the percentage circle width elongation versus the average initial circle diameter. It can be seen from the trend of the graph that the percent elongation decreases as the initial circle diameter increases; this trend follows the behavior of the percent crack length elongation versus initial crack length (Fig. 6.13). Not only the trend, but also the magnitude of the % elongation is comparable to that of the crack length.

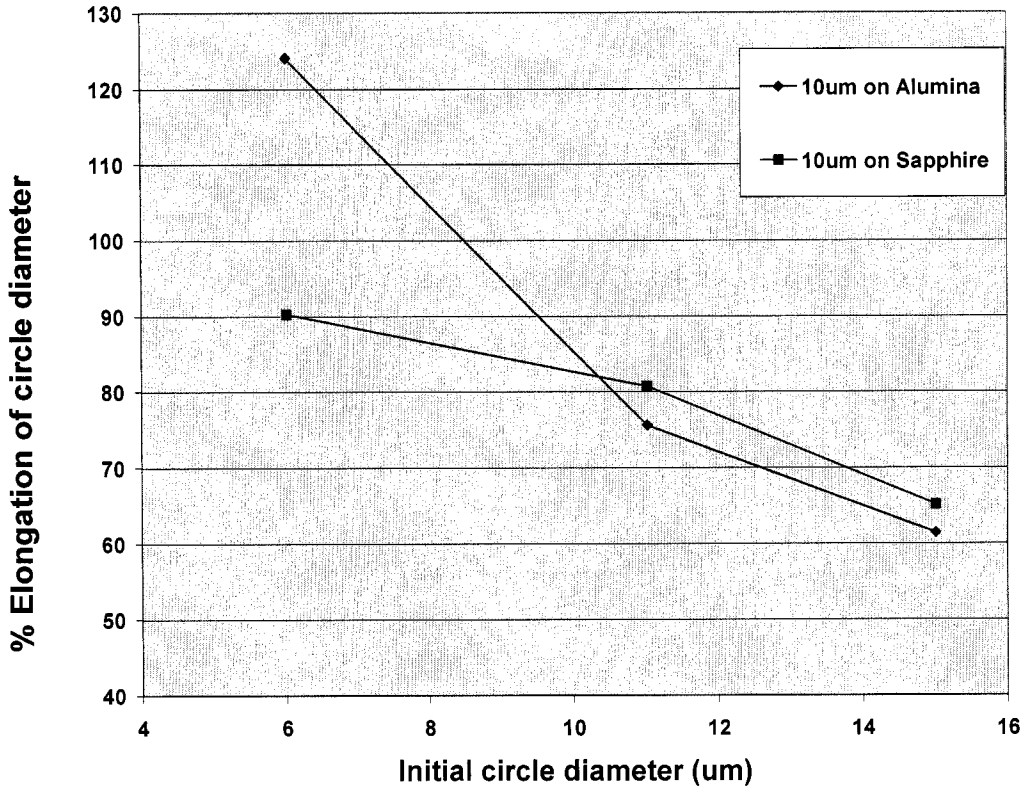

Figure 6.15 Circle elongation vs. circle diameter

The area around the milled circles exhibited more uniform damage in every direction compared to that of the cracks. However, as shown in Figure 6.16, there appeared to be a directional surface damage that had also been observed in the samples with cracking. In the crack samples the damage was always parallel to the cracks. Initially, the origin of this damage was not clear. One hypothesis was that it was due to stress concentrations around cracks. However, since it also is present in the samples with holes, an alternate explanation is needed. It turns out that the surface damage observed is from the single scan taken with the milling beam needed to map the milling area before milling begins. There is no known way to avoid this since this initial scan is needed to create a map of the area that includes the features to be milled. From the point of view of the goal of this study, this effect is not considered serious since the surface damage does not initiate defects. It may have a secondary effect by modifying the densification of the particles around the defect.

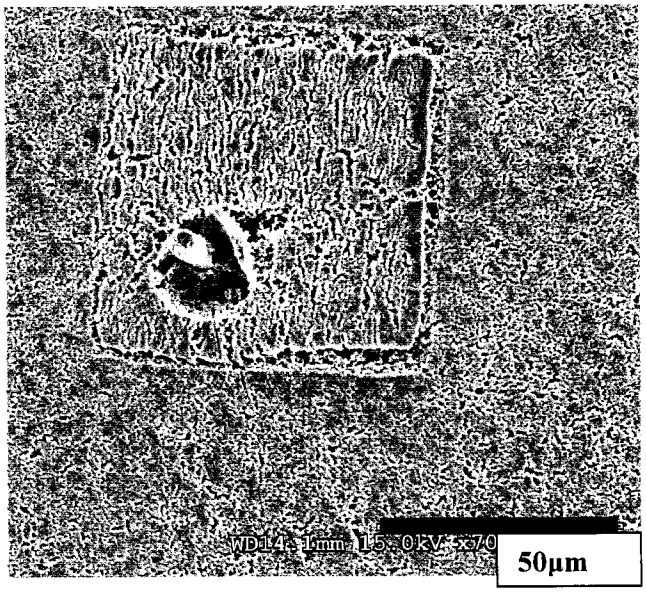

Figure 6.16 Sintered film with introduced circle defect showing the surface damage caused by the FIB

VI.6 CHANNEL CRACKS

During the microstructural analysis of the sintered cracks and holes, many "channel cracks" were observed. Channel cracks are very thin cracks (narrow crack opening displacement) created by the large stresses generated during cooling from the sintering temperature due to the mismatch in thermal expansion coefficients between the film and substrate. The thermal expansion coefficient for Tosoh 8 mol% YSZ is 9.5 X 10^{-6}/°C, the thermal expansion coefficient for alumina is 8.2 X 10^{-6}/°C, and the thermal expansion coefficient for sapphire is 8.8 X 10^{-6}/°C. This will lead to tensile stress in the film during cooling. The trans-granular nature of the cracks as shown in Figure 6.17 is clear evidence that these cracks have formed during cooling (after sintering). It can also be clearly seen that the cracks extend through the thickness of the film.

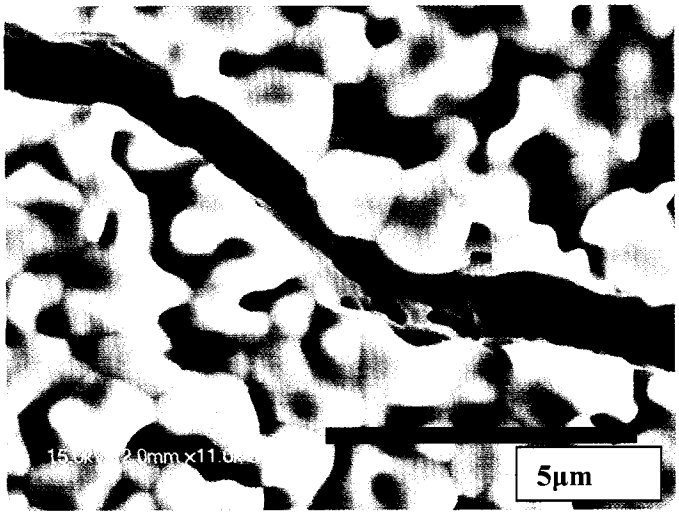

Figure 6.17 Channel crack across grains

Upon further careful analysis, it was observed that the channel cracks occurred in all of the sintered films that had introduced defects in them (cracks or holes). In the sintered films with no defects, channel cracks were not found. One example of this is shown in Figure 6.18. Note that this micrograph is from a large area of the film.

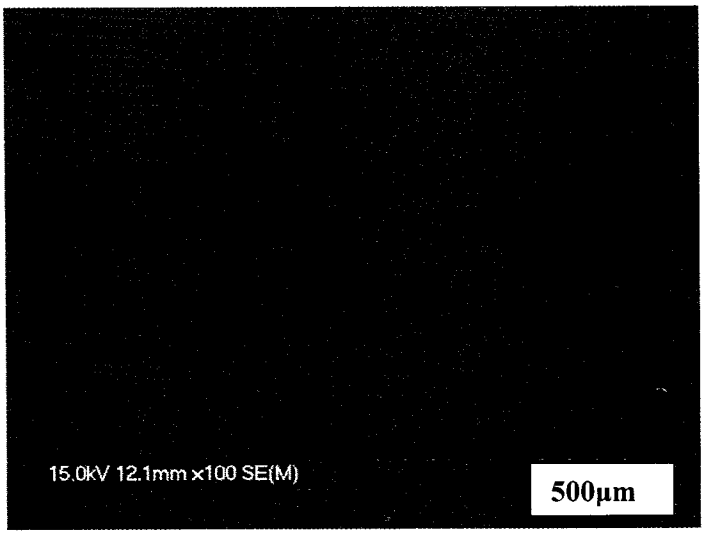

Figure 6.18 Sintered film with no FIB'd features or channel cracks

The stress in the film during cooling due to the thermal expansion mismatch is acting in every direction on the film around the crack. The schematic illustration in Figure 6.19 shows the difference between the diffusion growth of preexisting cracks and defects during sintering and the formation of channel cracks during cooling. During sintering, the biaxial sintering stresses acting on the constrained film leads to a growth in the length and width of the preexisting crack that was introduced. Mechanistically, this crack growth occurs by diffusion and is analogous to creep crack growth. In addition, due to stress concentrations ahead of the crack tip, diffused damage in the form of micro-cracks is generated.

During cooling, the film wants to shrink more than the substrate does, so in-plane tensile stresses develop in the film. The tensile stresses are going to be the highest near the corner of the crack tip, where the stress concentration is the largest. This is where the channel cracks should initiate. Due to the biaxial nature of the stresses, the cracks tend to propagate at 45° to the main crack. These general trends were observed in most samples.

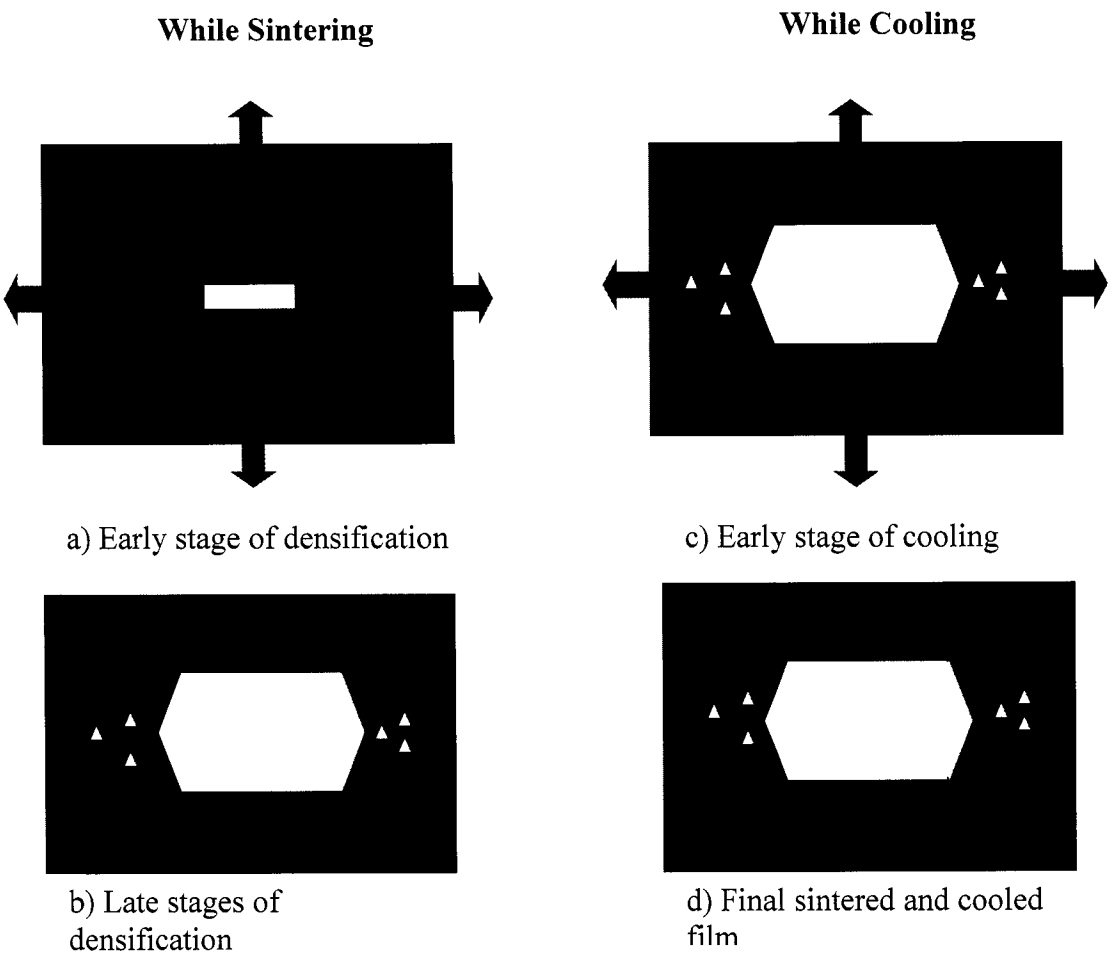

Figure 6.19 Schematic illustration of creep crack growth, and channel crack growth from thermal expansion mismatches

VI.6.1 STRESSES DUE TO THERMAL EXPANSION MISMATCH

In this subsection, the stresses that develop during cooling due to thermal expansion mismatch are calculated. These stresses are compared to the expected strength of the film in order to ascertain if they are sufficient to induce channel cracks. As was discussed in the last sub-section, channel cracks were only observed in films with defects introduced by FIB.

The calculation of the stresses generated due to coefficient of thermal expansion (CTE) mismatch is straightforward. In a film on a substrate, the elastic biaxial stresses are given by [10]:

$$\sigma_x = \sigma_y = (\alpha_1 - \alpha_2)E_p \times \Delta T \tag{6.4}$$

Where (α_1- α_2) is the difference in thermal expansion coefficient, ΔT is the temperature difference between the zero stress state and the temperature of interest and E is the elastic modulus of the film. There is a small error in using single values of α & E since in reality both thermal expansion coefficients and the modulus change as a function of temperature.

In order to calculate stresses using Equation (6.4), the elastic modulus and the CTEs are needed. The CTE for 8mol% YSZ is 9.5 x 10^{-6}/°C and for Al_2O_3 is 8.2 x 10^{-6}/°C (values given by the suppliers). The elastic modulus for fully dense 8mol% YSZ is 200MPa (from the supplier). It is recognized that the films are porous (Figure 6.20) with a porosity of approximately 20 vol% (measured by image analysis). There is a large body of literature on the effect of porosity on the elastic modulus of ceramics [11]. For well distributed porosity, one of the phenomenological relations that has been well established is [12]:

$$E_p = E_o (1 - 1.9P + 0.9P^2) \tag{6.5}$$

Where E_o and E_p are the modulus of fully dense and porous ceramic, respectively, and P is porosity. Using this relation, the modulus of the porous film is estimated to be 131 GPa.

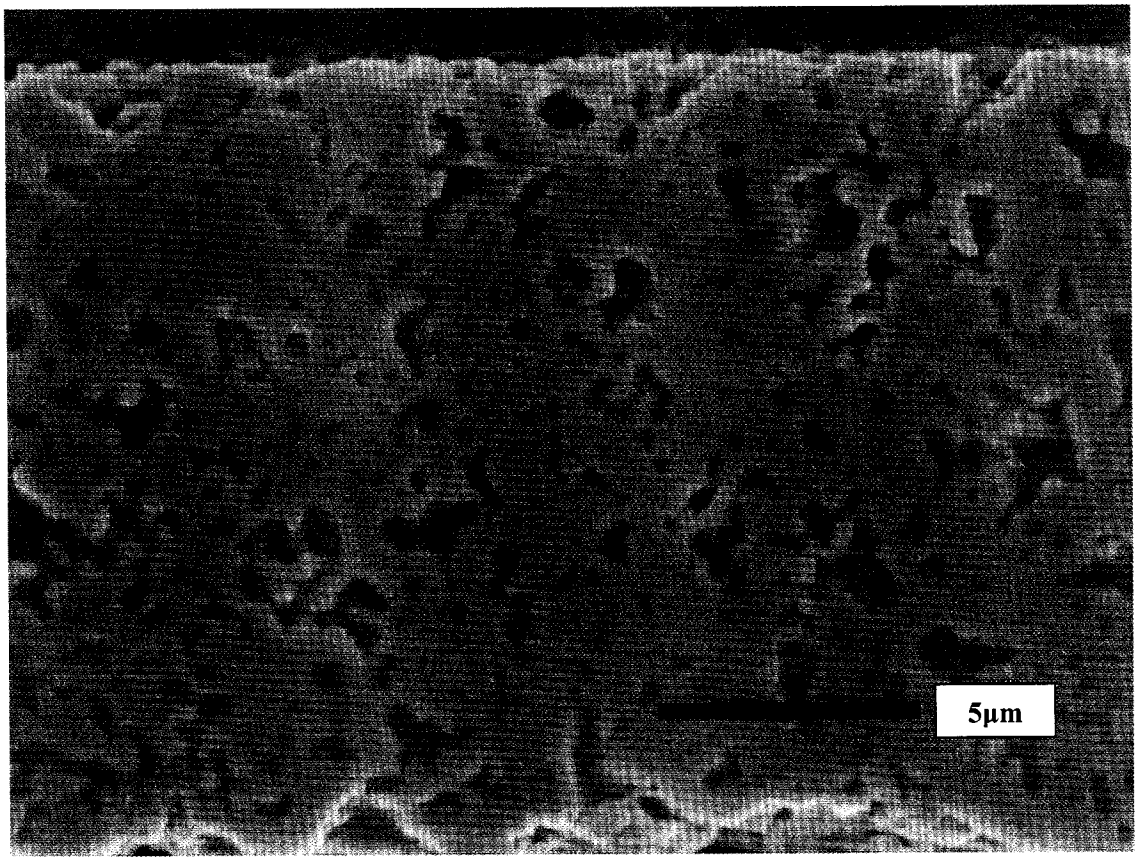

Figure 6.20 Cross-section of constrained YSZ film used for crack growth study.

Finally, in order to calculate the stress, a value of ΔT is needed. This is bounded by a maximum value of 1325°C (the difference between the sintering temperature of 1350°C and room temperature). A more realistic value is about 800°C since YSZ is known to creep at a temperature higher than approximately 800°C [13]. Creep leads to viscoelastic relaxation of stress and hence elastic stress only develops for temperatures less than 800°C. It should be noted that ageing effects in YSZ SOFCs have also been observed at temperatures above 800°C [14, 15]. Using these values for ΔT, the biaxial stress is calculated to be:

$$132MPa^{800C} < \sigma_{biaxial} < 226MPa^{1350C} \tag{6.6}$$

In order to evaluate if these stresses are sufficient to cause channel cracks around defects but not in the absence of defects, estimation is needed of the strength of the film and the stress concentration around defects. For long cracks thru the thickness of the film subjected to biaxial stresses, the stress intensity factor is about 4 and for holes the stress intensity factor is about 3 [10]. Since the channel cracks were observed around the holes and cracks but not in films without defects, it can be estimated that the strength of the film is less than $3\sigma_{min}$ (396MPa). A rather well established relation for the strength of porous ceramics is [12]:

$$(\sigma_f)_p = (\sigma_f)_o \exp(-np) \tag{6.7}$$

Where $(\sigma_f)_o$ and $(\sigma_f)_p$ are the strengths of the fully dense & the porous ceramics. Using a value of n=4 (typical for uniform porosity), porosity of 0.2 and strength of the dense film equal to 300MPa (from supplier), a value of the porous film is calculated to be 135MPa. This is within the stress window, and reasonable to assume a possible porous film strength.

In addition, these samples are very thin and uniform ceramic films. It is proven that for ceramics, the strength increases as the sample size decreases. For this reason it has to be assumed that the strength of the porous film is anywhere between the calculated 135MPa and $3\sigma_{min}$ or 396MPa (the lowest point where channel cracks were observed).

Using a value of n=4, porosity of 0.2 and porous strength of film equal to $3\sigma_{min}$, a maximum value of the strength of fully dense YSZ is calculated to be 881MPa. Although this number is higher than the quoted dense strength of 300MPa (by the manufacturer), it is not unreasonable since the films are very thin and uniform. Since no cracks were observed in the films without defects, it can be concluded that the strength of the corresponding fully dense YSZ film would be between 294MPa ($\sigma/3$) and 881MPa (σ).

VI.7 SINTERING CRACKS

Thin channel cracks formed during cool down from thermal expansion mismatch have been observed and discussed. Growth of introduced cracks in the constrained films, and the micro-crack development ahead of the tip has been discussed and their behavior analyzed. Whereas both of these types of defects were observed in all films with initial defects introduced by the FIB, another type of crack was observed in some of the films. These cracks, shown in Figure 6.21, are wider than the channel cracks and are not trans-granular. These cracks are also much longer, and have more irregular growth patterns. They originate from the introduced defects and are sintering cracks that develop during constrained sintering of the film. The driving force for them is the biaxial tensile stress in the film due to densification. These cracks must be sintering cracks that developed during sintering due to the fact that their crack opening displacements are large and their inter-granular nature. The length of these cracks shows that a critical stress in the film during sintering led to their propagation. Another observation from the microstructure analysis, obvious in Figure 6.21, is that the sintering cracks propagated

at roughly 45° from the tip of the defect due to the biaxial nature of the tensile stress due to constrained sintering [16].

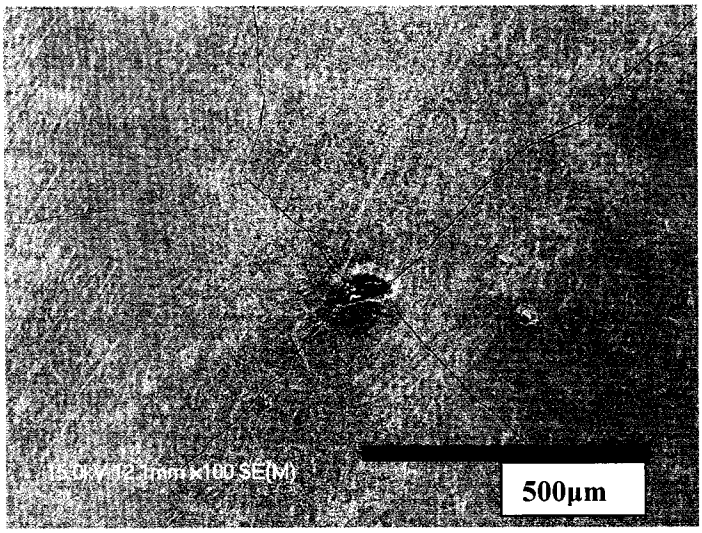

Figure 6.21 Sintered film with FIB'd defect and channel cracks

All films were carefully analyzed to see which ones had sintering cracks. Thicker films were observed to have a high occurrence of crack propagation except for the thick film on platinum substrates. Thinner films on all substrates tended not to have sintering cracks. None of the films on platinum substrates had sintering cracks. The observations are summarized in Table 6.3.

Table 6.3 Sintering crack observations for the various FIB samples

Film Thickness	Alumina substrate (largest sub. friction)	Sapphire substrate (less sub. friction)	Platinum Substrate (least sub. friction)
40μm	Crack growth (most samples)	Crack growth	None
20μm	Crack growth	None (most samples)	None
10μm	None	None	None
10μm (Circles)	None	None	

The interfacial friction between platinum & YSZ is low leading to easy sliding of the YSZ films at the sintering temperature. This sliding releases the constraint and reduces the stress concentration at the tip of the introduced defects. For films on sapphire and alumina, the films do not slide very easily and this leads to high stress concentration which favors the growth of sintering cracks. For these films, as predicted by the analysis, there is a critical film friction cracks grow if friction is greater than this[2]. To determine if there is a critical film friction for the films studied in this dissertation, the occurrence of sintering cracks for each sample was plotted on the "fracture map" plot of Ref. 2. The 'y' axis is the inverse of the friction parameters and the 'x' axis is the initial crack length. An X will signify that the sample has indeed developed sintering cracks from the FIB crack, and a box will indicate that the sample has not. For most of the experiments there is more than one sample, in this case if there are samples that cracked and ones that did not for a certain situation, an X is placed inside a box. The results are shown in Figure 6.22. The friction parameter for the films depends on the substrate as well as the thickness, as presented in Table 6.2

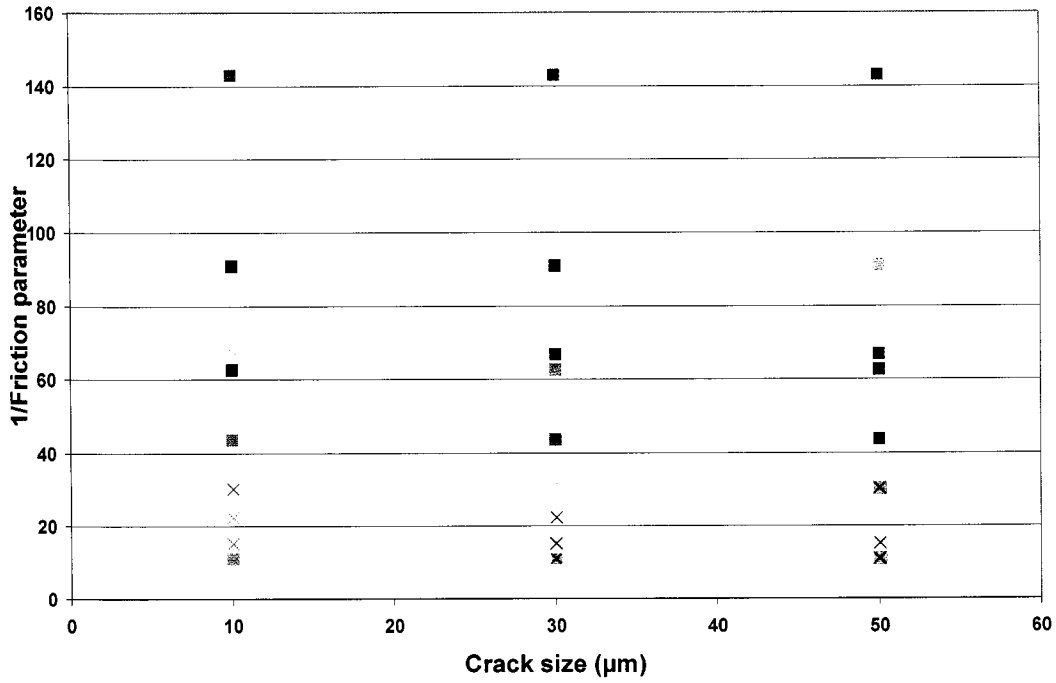

Figure 6.22 Sintering crack map for all of the FIB samples

The fracture map very clearly shows a critical 1/Friction Parameter value between about 33 and 42. This observation of a critical parameter is consistent with the prediction from crack growth models for constrained sintered films. Some of the samples below this critical friction parameter did not develop sintering cracks, however all samples above this critical point did not develop any sintering cracks. The few exceptions of crack growth below the critical friction parameter are believed to be due to normal variability in processing (e.g. differences in packing densities, film thickness, etc.).

In addition, since artificial cracks of all sizes led to sintering cracks for films in this study, it can be concluded that the critical crack size below which cracks will not propagate is below 10μm. Sintering cracks did not form around the artificial holes suggesting that the defects must be sharp to induce sintering cracks.

The sintering stress in the film acts in every direction (in the plane) on the film around the introduced crack. During sintering, the biaxial sintering stresses acting on the constrained film reaches a critical point at which the sintering cracks develop and grow by diffusion during sintering. The mismatch in thermal expansion still leads to stress during cool down. However, thermal expansion mismatch induced cracks (channel cracks) were not observed in films that had sintering cracks. It is postulated that the wide sintering cracks provide a location to relax thermal expansion mismatch stress.

VI.8 CONCLUSIONS

The Focused Ion Beam technique introduced in this study worked well to introduce artificial defects into a green ceramic film. This technique helped give insight into the microstructural development of constrained sintered films with micro-cracks or micro-holes. The following are the conclusions ascertained from this study.

- A stress concentration near a defect leads to damage. In addition, the introduced cracks & holes widen and grow. Lower interfacial friction was shown to lead to larger crack growth. A lower interfacial friction value (low wetability) leads to observed vertical crack walls, whereas higher friction leads to a variation in stresses along the thickness and the top of the wall tends to slope away from the interface at a constant slope.

- The dependence of the crack growth on the friction parameter for cracks of different length shows a transition from short crack to long crack. The crack growth for 30μm and 50μm is independent of the crack length, indicating a long crack response (stress intensities independent of crack length) while the 10μm long crack growth is different than the long cracks.

- Channel cracks due to thermal expansion mismatch are not present in the sintered films without pre-existing damage. The stress in the films was calculated with and without the introduced defects and shown that the films can withstand the stress from a defect-free film, but would not be able to sustain the stress from a concentrated stress near defects introduced in this study.

- Sintering cracks developed for some samples where the interface friction was higher, and when the film was thicker. This combination of high interfacial friction and thicker film (where the top is not restricted by the substrate) led to a

critical situation where sintering cracks initiate and propagate. These cracks are formed during densification of the film and are significantly wider than the channel cracks.

- Channel cracks and sintering cracks tended to follow 45-degree path from corner of main crack tip. If sintering cracks occurred first at the corner, channel cracks would not develop around the defect.

- Although FIB is a good technique to introduce controlled defects, it does induce some damage to the green film.

Notes to Chapter VI

1. Bang, J. and Lu, G.-Q., *Constrained-film sintering of a borosilicate glass: In situ measurement of film stresses.* Journal of the American Ceramic Society, 1995. 78(3): p. 813-815.

2. Bordia, R.K. and Jagota, A., *Crack growth and damage in constrained sintering films.* Journal of the American Ceramic Society, 1993. 76(10): p. 2475-2485.

3. Cheng, T. and Raj, R., *Flaw generation during constrained sintering of metal-ceramic and metal. Glass multilayer films.* Journal of the American Ceramic Society, 1989. 72(9): p. 1649-1655.

4. Hsueh, C.-h., Carneim, R.D., Becher, P.F. and Armstrong, T.R., *Constrained sintering of electrolyte films on porous electrodes.* Proceedings - Electrochemical Society, 2001. 2001-16(Solid Oxide Fuel Cells VII): p. 293-302.

5. de Souza, S., Visco, S.J. and De Jonghe, L.C., *Thin-film solid oxide fuel cell with high performance at low-temperature.* Solid State Ionics, 1997. 98(1,2): p. 57-61.

6. de Souza, S., Visco, S.J. and De Jonghe, L.C., *Reduced-temperature solid oxide fuel cell based on ysz thin-film electrolyte.* Journal of the Electrochemical Society, 1997. 144(3): p. L35-L37.

7. Jagota, A. and Hui, C.Y., *Mechanics of sintering thin films. Ii. Cracking due to self-stress.* Mechanics of Materials, 1991. 11(3): p. 221-234.

8. Jagota, A. and Hui, C.Y., *Mechanics of sintering thin films. I. Formulation and analytical results.* Mechanics of Materials, 1990. 9(2): p. 107-119.

9. Miller, K.T., Lange, F.F. and Marshall, D.B., *Instability of polycrystalline thin films. Experiment and theory.* Journal of Materials Research, 1990. 5(1): p. 151-160.

10. Callister, W.D., *Materials science and engineering : An introduction / william d. Callister, jr.* 6th ed ed. 2003, New York :: Wiley. xxi, 820 p. :.

11. Rice, R.W., *Porosity of ceramics / roy w. Rice.* 1998, New York :: M. Dekker. xii, 539 p. :.

12. Kingery, W.D., *Introduction to ceramics / w. D. Kingery, h. K. Bowen, d. R. Uhlmann.* 2d ed ed. 1976, New York :: Wiley. xii, 1032 p. :.

13. Lakki, A., Herzog, R., Weller, M., Schubert, H., Reetz, C., Gorke, O., Kilo, M. and Borchardt, G., *Mechanical loss, creep, diffusion and ionic conductivity of zro2 8 mol% y2o3 polycrystals.* Journal of the European Ceramic Society, 2000. 20(3): p. 285-296.

14. Ciacchi, F.T., Crane, K.M. and Badwal, S.P.S., *Evaluation of commercial zirconia powders for solid oxide fuel cells.* Solid State Ionics, 1994. 73(1-2): p. 49-61.

15. Suzuki, Y., *Activation energy for electrical conduction of y2o3-stabilized zro2 containing 8 mol% y2o3.* Solid State Ionics, 1996. 91(3-4): p. 239-241.

16. Bordia, R.K., Zuo, R., Guillon, O., Salamone, S.M. and Rodel, J., *Anisotropic constitutive laws for sintering bodies.* Acta Materialia, 2006. 54(1): p. 111-118.

CHAPTER VII

SUMMARY AND CONCLUSIONS

This experimental research has focused on the evolution of microstructure and defects in sinter-forged and constrained ceramic films. The topic is of significant interest for a variety of technologically important ceramics. Examples include multilayer ceramic systems and ceramic films and coatings. The focus of this study was 8mol% Y_2O_3 stabilized ZrO_2, the material used as electrolyte in solid oxide fuel cells. Following is a summary of the important findings of this study.

Modified densification and anisotropic pore development in sinter-forged YSZ

- An investigation into the microstructural evolution of tape cast YSZ films has shown that the uniaxial loading of the sample leads to modified densification. The densification increased as the compressive load increased.

- The second part of the investigation into sinter-forging tape cast YSZ films demonstrated that uniaxial compressive loading leads to anisotropic pore development. The intrinsic pores preferentially oriented parallel to the uniaxial loading direction. The experiments showed that an increase in the axial stress leads to an increase in the extent of pore orientation anisotropy.

- A study of the behavior of pores based on size using controlled sized pores showed that there is a transition point between intrinsic pores and extrinsic pores. This transition point is where uniaxially loaded pores switch from orienting parallel to the compressive load, to perpendicular to the load. For sinter-forging 0.5μm particle size YSZ compacts with a nominal compressive

stress of 1.0MPa, the critical size at which this transition occurs is approximately 1μm. Pores of this size remain isotropic even in the sinter-forged samples.

- A further investigation into this pore behavior transition point used a smaller particle sized YSZ powder with polystyrene spheres twice the powder diameter to determine if this transition point scaled proportional to the powder size. The results showed that the transition point does not scale proportional in proportion to the particle size, and the intrinsic pores behaved similarly as they would in a sample with larger initial powder diameter.

- An in-depth investigation was conducted to further quantify the behavior of the intrinsic pores anisotropic development. The orientation showed a strong dependence on uniaxial load, and no significant dependence on the temperature. The pores preferentially oriented parallel to the uniaxial load. The magnitude of the intrinsic pore re-orientation was not significant, the maximum pore angle was about 53° (compared to 45° for isotropic).

- An in-depth investigation was also conducted to further quantify the behavior of extrinsic-pore anisotroic development. The orientation also showed a strong dependence on uniaxial load, and no significant dependence on the temperature. The extrinsic pores preferentially oriented perpendicular to the uniaxial load. The magnitude of the pore re-orientation was more significant, with the average angle of 20° for samples forged at 1MPa (isotropic pores have an average orientation of 45°).

- The microstructure of a naturally constrained YSZ film was analyzed to compare to the sinter-forged samples which are intended to potentially mimic constrained or partially constrained systems. Intrinsic pore orientations in

samples of similar density to that studied in the sinter-forged experiments were investigated. The intrinsic pores showed a preferential orientation of their pores perpendicular to that of the substrate. The average pore orientation was about 53°. This is extremely close to the maximum observed for the sinter forged samples.

- The lower magnitude of re-orientation of the intrinsic pores during constrained sintering or sinter-forging is attributed to the healing of the pores due to the high driving forces to sinter the short radius tip curvature of the pores. The increased sintering of the pore tip was not seen in the extrinsic pores as the tip radius is still much larger than that for the intrinsic pores.

- Another observation during the pore orientation investigation is the dependence of anisotropy to the localized density of the region that the pore is in. In a sinter-forged sample (and initial data suggests in constrained films as well), if an isolated pore is in a region of high density the pore will be isotropic, and if a pore is in a region of low density it will be anisotropic. This observation needs to be further explored.

<u>Crack and hole development in constrained YSZ films</u>

- A stress concentration near a defect leads to damage. In addition, the introduced cracks & holes widen and grow. Lower interfacial friction was shown to lead to larger crack growth. A lower interfacial friction value (low wetability) leads to observed vertical crack walls, whereas higher friction leads to a variation in stresses along the thickness and the top of the wall tends to slope away from the interface at a constant slope.

- The dependence of the crack growth on the friction parameter for cracks of different length shows a transition from short crack to long crack. The crack growth for 30μm and 50μm is independent of the crack length, indicating a long crack response (stress intensities independent of crack length) while the 10μm long crack growth is different than the long cracks.

- Channel cracks due to thermal expansion mismatch are not present in the sintered films without pre-existing damage. The stress in the films was calculated with and without the introduced defects and shown that the films can withstand the stress from a defect-free film, but would not be able to sustain the stress from a concentrated stress near defects introduced in this study.

- Sintering cracks developed for some samples where the interface friction was higher, and when the film was thicker. This combination of high interfacial friction and thicker film (where the top is not restricted by the substrate) led to a critical situation where sintering cracks initiate and propagate. These cracks are formed during densification of the film and are significantly wider than the channel cracks.

- Channel cracks and sintering cracks tended to follow 45-degree path from corner of main crack tip. If sintering cracks occurred first at the corner, channel cracks would not develop around the defect.

- Although FIB is a good technique to introduce controlled defects, it does induce some damage to the green film.

CHAPTER VIII

FUTURE WORK

The experiments conducted in this dissertation have increased the qualitative and quantitative understanding of anisotropic microstructure pore development in sinter-forged and constrained compacts, as well as improved our understanding of defect growth in fully constrained YSZ films. The proposed work for further study is focused around investigating the anisotropic behavior of grain growth in sinter-forged and constrained compacts.

It is now clear that pore orientations in stressed compacts develop anisotropically, with the magnitude and angle depending on pore size, uniaxial load, sintering temperature and sample density. But there is one area of the anisotropic microstructure investigation that needs to be addressed. At higher sample densities when pores start to return to an isotropic shape, what effect is still present in the microstructure? Is the grain structure affected at all by the anisotropy of the pore development at lower densities, and at higher densities when the pore anisotropy is corrected, does the anisotropy, if any, still exist in the grains?

This grain behavior should be investigated for both sinter-forged samples as well as constrained films. Adding this anisotropic grain development work to the work done in this dissertation will provide a broad and complete picture of anisotropic microstructure development.

Some other areas identified as needing further investigation are:

a) A further investigation into intrinsic/extrinsic pore behavior. A more in depth study into what the pore behavior depends on, including the mechanisms of pore anisotropy evolution would be very helpful in understanding this difference in behavior.

b) Evolution of pore anisotropy as a function of density. Initial observations suggest that there may be a dependence of anisotropy on the density of the sample.

c) A model for the growth of cracks and holes in constrained films, including critical parameters that induce crack growth. While this study did increases the knowledge of crack growth in constrained films, a crack growth map would be advantageous to have to apply to many samples.

BIBLIOGRAPHY

Abramo, M. T. and L. L. Hahn (1996). "Application of advanced techniques for complex focused-ion-beam device modification." Microelectronics and Reliability 36(11-12): 1775-1778.

Ashby, M. F. (1974). "Sintering diagrams." Acta Metallurgica 22(3): 275-89.

Bang, J. and G.-Q. Lu (1995). "Constrained-film sintering of a borosilicate glass: in situ measurement of film stresses." Journal of the American Ceramic Society 78(3): 813-815.

Baur, E. and H. Preis (1937). "Fuel cells with rigid conductors." Zeitschrift fuer Elektrochemie und Angewandte Physikalische Chemie 43: 727-32.

Baur, E. and T. WD (1920). Brennstoffelement. DRP 325 783, filed 20.9.1916.

Besson, J. and M. Abouaf (1992). "Rheology of porous alumina and simulation of hot isostatic pressing." Journal of the American Ceramic Society 75(8): 2165-72.

Blomen, L. J. M. J. and M. N. Mugerwa (1993). Fuel cell systems New York :, Plenum Press.

Bordia, R. (1986). Sintering of Inhomogenous or Constrained Powder Compacts: Modelling and Experiments, Cornell University. Ph.D.

Bordia, R. K. and A. Jagota (1993). "Crack growth and damage in constrained sintering films." Journal of the American Ceramic Society 76(10): 2475-2485.

Bordia, R. K. and R. Raj (1985). "SINTERING BEHAVIOR OF CERAMIC FILMS CONSTRAINED BY A RIGID SUBSTRATE." Journal of the American Ceramic Society 68(6): 287-292.

Bordia, R. K. and R. Raj (1988). "Hot isostatic pressing of ceramic/ceramic composites at pressures <10 MPa." Advanced Ceramic Materials 3(2): 122-6.

Bordia, R. K. and R. Raj (1988). "Sintering and titania-alumina composites: a model experimental investigation." Journal of the American Ceramic Society 71(4): 302-10.

Bordia, R. K. and G. W. Scherer (1988). "On constrained sintering-I. Constitutive model for a sintering body." Acta Metallurgica 36(9): 2393-2397.

Bordia, R. K. and G. W. Scherer (1988). "On constrained sintering-II. Comparison of constitutive models." Acta Metallurgica 36(9): 2399-2409.

Bordia, R. K. and G. W. Scherer (1988). "On constrained sintering-III. Rigid inclusions." Acta Metallurgica 36(9): 2411-2416.

Bordia, R. K., R. Zuo, et al. (2006). "Anisotropic constitutive laws for sintering bodies." Acta Materialia 54(1): 111-118.

Boutz, M. M., L. Winnubst, et al. (1995). "Low-temperature sinter forging of nanostructured Y-TZP and YCe-TZP." Journal of the American Ceramic Society 78(1): 121-128.

Busso, E. P., R. P. Travis, et al. (1998). "Residual stress generation during constrained sintering of layered ceramic thin film structures." Materials Research Society Symposium Proceedings 505(Thin-Films--Stresses and Mechanical Properties VII): 547-552.

Cai, P. Z., D. J. Green, et al. (1997). "Constrained densification of alumina/zirconia hybrid laminates, I: experimental observations of processing defects." Journal of the American Ceramic Society 80(8): 1929-1939.

Cai, P. Z., G. L. Messing, et al. (1997). "Determination of the mechanical response of sintering compacts by cyclic loading dilatometry." Journal of the American Ceramic Society 80(2): 445-452.

Callister, W. D. (2003). Materials science and engineering : an introduction / William D. Callister, Jr. New York :, Wiley.

Carroll, D. R. and M. N. Rahaman (1994). "An initial stage model for the sintering of constrained polycrystalline thin films." Journal of the European Ceramic Society 14(5): 473-9.

Chang, C.-R. and J.-H. Jean (1998). "Effects of silver-paste formulation on camber development during the cofiring of a silver-based, low-temperature-cofired ceramic package." Journal of the American Ceramic Society 81(11): 2805-2814.

Chang, J. C., B. V. Velamakanni, et al. (1991). "Centrifugal consolidation of alumina and alumina/zirconia composite slurries vs. interparticle potentials: particle packing and mass segregation." Journal of the American Ceramic Society 74(9): 2201-4.

Cheng, T. and R. Raj (1989). "Flaw generation during constrained sintering of metal-ceramic and metal. Glass multilayer films." Journal of the American Ceramic Society 72(9): 1649-1655.

Choe, J. W., J. N. Calata, et al. (1995). "Constrained-film sintering of a gold circuit paste." Journal of Materials Research 10(4): 986-994.

Chu, M.-Y., L. C. De Jonghe, et al. (1989). "Effect of temperature on the densification/creep viscosity during sintering." Acta Metallurgica 37(5): 1415-1420.

Ciacchi, F. T., K. M. Crane, et al. (1994). "Evaluation of commercial zirconia powders for solid oxide fuel cells." Solid State Ionics 73(1-2): 49-61.

Coble, R. L. (1961). "Sintering crystalline solids. I. Intermediate- and final-state diffusion models." Journal of Applied Physics 32: 787-92.

Coble, R. L. (1961). "Sintering crystalline solids. II. Experimental test of diffusion models in powder compacts." Journal of Applied Physics 32: 793-9.

De Jonghe, L. C. and M. N. Rahaman (1984). "Loading dilatometer." Review of Scientific Instruments 55(12): 2007-10.

de Souza, S., S. J. Visco, et al. (1997). "Reduced-temperature solid oxide fuel cell based on YSZ thin-film electrolyte." Journal of the Electrochemical Society 144(3): L35-L37.

de Souza, S., S. J. Visco, et al. (1997). "Thin-film solid oxide fuel cell with high performance at low-temperature." Solid State Ionics 98(1,2): 57-61.

Di Maio, D. and S. G. Roberts (2005). "Measuring fracture toughness of coatings using focused-ion-beam-machined microbeams." Journal of Materials Research 20(2): 299-302.

Du, Z. Z. and A. C. F. Cocks (1992). "Constitutive models for the sintering of ceramic components - I. Material models." Acta Metallurgica et Materialia 40(8): 1969-79.

Du, Z. Z. and A. C. F. Cocks (1992). "Constitutive models for the sintering of ceramic components - II. Sintering of inhomogeneous bodies." Acta Metallurgica et Materialia 40(8): 1981-94.

Flinn, B. D., R. K. Bordia, et al. (2000). "Evolution of defect size and strength of porous alumina during sintering." Journal of the European Ceramic Society 20(14-15): 2561-2568.

Garino, T. J. and H. K. Bowen (1987). "DEPOSITION AND SINTERING OF PARTICLE FILMS ON A RIGID SUBSTRATE." Journal of the American Ceramic Society 70(11): 315-317.

Garino, T. J. and H. K. Bowen (1990). "Kinetics of constrained-film sintering." Journal of the American Ceramic Society 73(2): 251-7.

Haber, F. (1907). "Verfahren zur Erzeugung von elektrischer Energie aus Kohle und gasformigen Brennstoffen." Oster Pat 27 743, filed 5.8.1905.

Hague, D. C. and M. J. Mayo (1997). "Sinter-forging of nanocrystalline zirconia: I, experimental." Journal of the American Ceramic Society 80(1): 149-156.

He, Y. J., A. J. A. Winnubst, et al. (1996). "Enhanced mechanical properties by grain boundary strengthening in ultra-fine-grained TZP ceramics." Journal of the European Ceramic Society 16(6): 601-612.

He, Y. J., A. J. A. Winnubst, et al. (1994). "Improvement of mechanical properties of zirconia-toughened alumina by sinter forging." Journal of Materials Science 29(22): 5868-74.

Hsueh, C.-h., R. D. Carneim, et al. (2001). "Constrained sintering of electrolyte films on porous electrodes." Proceedings - Electrochemical Society 2001-16(Solid Oxide Fuel Cells VII): 293-302.

Hsueh, C. H. (1985). "SINTERING OF A CERAMIC FILM ON A RIGID SUBSTRATE." Scripta Metallurgica 19(10): 1213-1217.

Hund, F. (1951). "Anomalous solid solutions in the system zirconia-yttria. Crystal structure of Nernst glowers." Zeitschrift fuer Elektrochemie und Angewandte Physikalische Chemie 55: 363-6.

Iacomini, D. C. S. http://ares.ame.arizona.edu/materials/crystal.html.

Jagota, A. and C. Y. Hui (1990). "Mechanics of sintering thin films. I. Formulation and analytical results." Mechanics of Materials 9(2): 107-119.

Jagota, A. and C. Y. Hui (1991). "Mechanics of sintering thin films. II. Cracking due to self-stress." Mechanics of Materials 11(3): 221-234.

Jean, J.-H. and C.-R. Chang (1997). "Camber development during cofiring Ag-based low-dielectric-constant ceramic package." Journal of Materials Research 12(10): 2743-2750.

Jean, J.-H. and C.-R. Chang (1997). "Cofiring kinetics and mechanisms of an Ag-metalized ceramic-filled glass electronic package." Journal of the American Ceramic Society 80(12): 3084-3092.

Jean, J.-H., C.-R. Chang, et al. (1997). "Effect of densification mismatch on camber development during cofiring of nickel-based multilayer ceramic capacitors." Journal of the American Ceramic Society 80(9): 2401-2406.

Jud, P. P., G. Grossmann, et al. (2005). "Local creep in SnAg3.8Cu0.7 lead-free solder." Journal of Electronic Materials 34(9): 1206-1214.

Kingery, W. D. (1976). Introduction to ceramics / W. D. Kingery, H. K. Bowen, D. R. Uhlmann. New York :, Wiley.

Lakki, A., R. Herzog, et al. (2000). "Mechanical loss, creep, diffusion and ionic conductivity of ZrO2 8 mol% Y2O3 polycrystals." Journal of the European Ceramic Society 20(3): 285-296.

Lin, Y.-C. and J.-H. Jean (2004). "Constrained Sintering of Silver Circuit Paste." Journal of the American Ceramic Society 87(2): 187-191.

Liu, J. and S. A. Barnett (2002). "Thin yttrium-stabilized zirconia electrolyte solid oxide fuel cells by centrifugal casting." Journal of the American Ceramic Society 85(12): 3096-3098.

Lu, G. Q., R. C. Sutterlin, et al. (1993). "Effect of mismatched sintering kinetics on camber in a low-temperature cofired ceramic package." Journal of the American Ceramic Society 76(8): 1907-14.

Majumdar, S., T. Claar, et al. (1986). "Stress and Fracture Behavior of Monolithic Fuel Cell Tapes." Journal of the American Ceramic Society 69(8): 628-633.

Maximenko, A. L. and O. Van Der Biest (2001). "Modelling of damage development during sintering." Journal of the European Ceramic Society 21(8): 1061-1071.

Melngailis, J. (1987). "Focused ion beam technology and applications." Journal of Vacuum Science & Technology, B: Microelectronics and Nanometer Structures 5(2): 469-95.

Miller, K. T., F. F. Lange, et al. (1990). "Instability of polycrystalline thin films. Experiment and theory." Journal of Materials Research 5(1): 151-160.

Nagaishi, M., K. Takeuchi, et al. (1999). "Preparation of yttria-stabilized zirconia thin films by sedimentation from liquid suspension." Key Engineering Materials 159-160: 163-168.

Nernst, W. (1899). "Verfahren zur Erzeugung von elektrischem Gluhlicht." DRP 104 872, filed 6.7.1897.

Nernst, W. (1901). "Material for electric-lamp glowers." US-P 685 730, filed 24.8.1899.

Ondik, H. M., H. F. McMurdie, et al. (1998). Phase diagrams for zirconium and zirconia systems Westerville, Ohio :, American Ceramic Society.

Orth, A., J. P. Reithmaier, et al. (1995). "Gain-modulated second order distributed feedback gratings fabricated by maskless focused ion beam implantation in GaInAsP heterostructures." Microelectronic Engineering 27(1-4): 343-346.

Owen, D. M. and A. H. Chokshi (1998). "Final stage free sintering and sinter forging behavior of a yttria-stabilized tetragonal zirconia." Acta Materialia 46(2): 719-29.

Panda, P. C., J. Wang, et al. (1988). "Sinter-forging characteristics of fine-grained zirconia." Journal of the American Ceramic Society 71(12): 507-509.

Rahaman, M. M. and L. C. De Jonghe (1984). "Sintering of cadmium oxide under low applied stress." Journal of the American Ceramic Society 67(10): C205-C207.

Rahaman, M. N., L. C. De Jonghe, et al. (1986). "EFFECT OF SHEAR STRESS ON SINTERING." Journal of the American Ceramic Society 69(1): 53-58.

Rahaman, M. N., L. C. De Jonghe, et al. (1986). "Creep during sintering of porous compacts." Journal of the American Ceramic Society 69(1): 58-60.

Raj, R. (1987). "Analysis of the sintering pressure." Journal of the American Ceramic Society 70(9): C/210-C/211.

Raj, R. and R. Bordia (1984). "Sintering Behavior of Bi-Modal Powder Compacts." Acta Metallurgica 32(7): 1003-1019.

Reyntjens, S. and R. Puers (2001). "A review of focused ion beam applications in microsystem technology." Journal of Micromechanics and Microengineering 11(4): 287-300.

Rice, R. W. (1998). Porosity of ceramics / Roy W. Rice. New York :, M. Dekker.

Rubanov, S. and P. R. Munroe (2005). "Damage in III-V compounds during focused ion beam milling." Microscopy and Microanalysis 11(5): 446-455.

Salamone, S. (2003). Densification of and constitutive laws for ceramic matrix composites and multilayered systems University of Washington. Ph.D.: 214.

Salamone, S. M., L. C. Stearns, et al. (2003). "Effect of rigid inclusions on the densification and constitutive parameters of liquid-phase-sintered

YBa2Cu3O6+x powder compacts." Journal of the American Ceramic Society 86(6): 883-892.

Scherer, G. W. and T. Garino (1985). "VISCOUS SINTERING ON A RIGID SUBSTRATE." Journal of the American Ceramic Society 68(4): 216-220.

Skandan, G., H. Hahn, et al. (1994). "Effect of applied stress on densification of nanostructured zirconia during sinter-forging." Materials Letters 20(5-6): 305-309.

Speight, M. V. and J. E. Harris (1967). "Kinetics of stress-induced growth of grain-boundary voids." Metal Science Journal 1: 83-85.

Stech, M., P. Reynders, et al. (2000). "Constrained film sintering of nanocrystalline TiO2." Journal of the American Ceramic Society 83(8): 1889-1896.

Suzuki, Y. (1996). "Activation energy for electrical conduction of Y2O3-stabilized ZrO2 containing 8 mol% Y2O3." Solid State Ionics 91(3-4): 239-241.

Tsuji, S., K. Tsujimoto, et al. (1998). "Application of cross-sectional transmission electron microscopy to thin-film-transistor failure analysis." IBM Journal of Research and Development 42(3-4): 509-516.

Venkatachari, K. R. and R. Raj (1986). "Shear deformation and densification of powder compacts." Journal of the American Ceramic Society 69(6): 499-506.

Venkatachari, K. R. and R. Raj (1987). "ENHANCEMENT OF STRENGTH THROUGH SINTER FORGING." Journal of the American Ceramic Society 70(7): 514-520.

Wagner, C. (1943). "The mechanism of electric conduction in the Nernst glower." Naturwissenschaften 31: 265-8.

Yashima, M., M. Kakihana, et al. (1996). "Metastable-stable phase diagrams in the zirconia-containing systems utilized in solid-oxide fuel cell application." Solid State Ionics 86-88(Part 2): 1131-1149.

Zhang, Y., J. Gao, et al. (2004). "Dip-coating thin yttria-stabilized zirconia films for solid oxide fuel cell applications." Ceramics International 30(6): 1049-1053.

Zhao, Y. and L. R. Dharani (1994). "Theoretical model for the analysis of a ceramic thin film sintering on a non-sintering substrate." Thin Solid Films 245(1-2): 109-114.

Zimmermann, A., M. Hoffman, et al. (1998). "Fracture of alumina with controlled pores." Journal of the American Ceramic Society 81(9): 2449-2457.

Zuo, R., E. Aulbach, et al. (2003). "Critical evaluation of hot forging experiments: Case study in alumina." Journal of the American Ceramic Society 86(7): 1099-1105.

Zuo, R., E. Aulbach, et al. (2003). "Experimental determination of sintering stresses and sintering viscosities." Acta Materialia 51(15): 4563-4574.

Zuo, R., E. Aulbach, et al. (2004). "Shrinkage-free sintering of low-temperature cofired ceramics by loading dilatometry." Journal of the American Ceramic Society 87(3): 526-8.

Zuo, R., E. Aulbach, et al. (2003). "Viscous Poisson's coefficient determined by discontinuous hot forging." Journal of Materials Research 18(9): 2170-2176.

VITA

Dustin Frame was born in Orlando and grew up on the gulf coast of Florida. After graduating high school the author moved with his family to Port Townsend, Washington in 1997. In 1999 he earned his Associates of Arts in Pre-Engineering from Peninsula College in Port Angeles, WA. He continued his undergraduate studies at the University of Washington in Seattle, WA where in 2001 he received his Bachelors of Science in Mechanical Engineering. Dustin pursued graduate studies at the University of Washington in Seattle, WA where he completed his Doctor of Philosophy in Materials Science & Engineering and Nanotechnology in 2006